Title	STUDIES ON SYNTHESIS AND PROPERTIES OF EUROPIUM (II) BORATES AND SILICATES
Author(s)	Machida, Ken-ichi
Citation	大阪大学, 1982, 博士論文
Version Type	VoR
URL	https://hdl.handle.net/11094/2160
rights	
Note	

STUDIES ON SYNTHESIS AND PROPERTIES OF EUROPIUM (II) BORATES AND SILICATES

1982

KEN-ICHI MACHIDA

STUDIES ON SYNTHESIS AND PROPERTIES
OF EUROPIUM (II)
BORATES AND SILICATES

(ユウロピウム（II）ホウ酸塩ならびにケイ酸塩
の合成と物性に関する研究)

1982

KEN-ICHI MACHIDA

Preface

The work in this thesis was carried out under the guidance by Professor Dr. Jiro Shiokawa at the Department of Applied Chemistry, Faculty of Engineering, Osaka University.

The purpose of the present thesis is to synthesize new europium(II) compounds and Eu^{2+}-activated calcium or strontium compounds, and to appreciate their possibilities for magnetic materials and phosphors. The author hopes that the findings obtained in this work would give the valuable suggestions for new inorganic compounds with useful technological properties.

Kenichi Machida

Ken-ichi Machida

Suita, Osaka
January, 1982

Contents

GENERAL INTRODUCTION

In recent years, compounds containing rare earth elements have been actively investigated directed toward the development of functional materials because they have various interesting and very useful physical properties such as their magnetic, optical, or electrical properties, etc. Since the systematic separation and purification procedures for a series of rare earth elements from one another were established and accordingly their metals or oxides with high purity were easily available as raw materials, these elements have played a particularly important part in the field of materials science.

The ions of rare earth elements generally are in the trivalent state. Under limited conditions, europium (Eu) gives the divalent ion stabilized by the attainment of half filled 4f shell as well as trivalent ion. The outer electrons of Eu^{2+} ion occupy a $4f^7$ configuration, and hence the Eu^{2+} ion has an effective magnetic moment of 7.94 μ_B in a similar manner as the gadolinium ion (Gd^{3+}). Since Matthias et al.1) found that a monoxide EuO is ferromagnetic below a low temperature (T_C=69 K), many europium(II) compounds have been synthesized because of their attractive magnetic properties, e.g., chalcogenides,2) silicates,3) aluminates,3) and titanates.4) Recently, EuO as a magnetic insulator has been taken notice of as laser beam addressable memory units in thin film5) for the unusually large magneto-optical effect.6) A silicate Eu_2SiO_4 also is a ferromagnet and can be prepared in a virtually transparent single crystal form for magneto-optic applications.7) In these oxides, the direct magnetic and indirect superexchange interactions between the neighboring Eu^{2+} ions take place owing to overlap of the 4f and 5d orbitals,8) the magnitudes of which strongly depend on the distances and angles via O^{2-} ions between the magnetic ions.2a,b) The magnetisms of highly symmetrical compounds have been theoretically interpreted on the basis of the crystal structures.4)

In addition, Eu^{2+}-activated compounds give line or band emissions assigned to $4f^7$-$4f^7$ or $4f^7$-$4f^6 5d$ transitions of Eu^{2+} ions.9) The materials as emitted by the latter transitions have been received attention as violet-blue to green emitting phosphors, whose colors are influenced by the arrangement of anions around the Eu^{2+} ion and the electronegativities of anions.[10)] A number of efficient photoluminescent materials have been obtained, viz., halides,[11)] borates,[12)] aluminates,[13)] silicates,[14)] and phosphates.[15)] Some of these compounds have been put to practical use as the phosphors for high-color-rendering fluorescent lamps or X-ray intensifying screens.[16)]

When the preparation of Eu^{2+}-containing mixed oxides is performed according to standard ceramic techniques, it comes into question that EuO is able to coexist only with a part of the metal oxides because of the strong reducing power. This fact is interpreted by considering the Gibbs' energy change (ΔG) in the reducing process of metal oxides (see Table I).[17)] Since the ΔG value of the reduction

$$2\ Eu_2O_3 \xrightarrow{-O_2} 4\ EuO$$

at 1500 K is 137 kcal/mol, the metal oxides which have smaller values than ΔG=137 kcal/mol are reduced to lower oxides or even to metals. From Table I, B_2O_3 and SiO_2 having ΔG=142 and 153 kcal/mol are seen to coexist with EuO. The temperature dependences for the oxygen fugacity (vapor phase) in the system Eu-O reported by McCarthy and White[18)] indicate that EuO is unstable at high temperatures in air or an oxidizing atmosphere.

Table I. Free energy changes for reductions of binary oxides per mole of O_2 at 1500 K (kcal/mol)

Oxide	ΔG[a]
CaO	231
$(R.E.)_2O_3$ (R.E.=La-Lu)	218-230
SrO	212
MgO	202
Al_2O_3	190
Li_2O	180
Ti_2O_3	178
SiO_2	153
B_2O_3	142
V_2O_3	137
MnO	130
Cr_2O_3	118
Ga_2O_3	95
FeO	82

[a] The dotted line indicates the position of the reaction $4\ EuO + O_2 \longrightarrow 2\ Eu_2O_3$.

Therefore, the preparation of Eu^{2+}-containing compounds by solid state reactions is required to be performed in vacuum, an inert gas, or a reducing atmosphere.

The present work has been carried out for the purpose of synthesizing new Eu^{2+}-containing compounds (borates and silicates) and investigating the crystal structures and physical (mainly magnetic and luminescent) properties. Especially, these physical properties are discussed by taking into consideration the results of X-ray structural analyses since those, in which the broadly spacing 5d orbitals take part, are closely related to the crystal structures as stated above.

This work is composed of four chapters and general conclusion. The first chapter deals with the crystal structures, the magnetic and luminescent properties, and the thermal stabilities (at high temperatures in air) for a series of europium(II) borates. The magnetic and luminescent properties have been interpreted from the crystal structures. In the second chapter, similarly, the crystal structures and physical properties of europium(II) haloborates are described, and the third chapter is mostly devoted to a description of the high-pressure polymorphism and luminescent properties of EuB_2O_4 as obtained in the first chapter. In these chapters, the relationship between the luminescent properties and the crystal structures or magnetisms has became more apparent. In the fourth chapter, the study has been made on the high-pressure polymorphism, crystal structures, and luminescent properties of $EuSiO_3$. The luminescent properties of $CaSiO_3:Eu^{2+}$ and $SrSiO_3:Eu^{2+}$ polymorphs have been discussed in terms of the X-ray structural and IR spectral analyses of host lattices, and the temperature dependences of luminescences.

The contents of this thesis are composed of the following papers:

1. Synthesis and Characterization of Divalent-Europium (Eu^{2+}) Compounds, EuB_4O_7, EuB_2O_4, and $Eu_2B_2O_5$,
   K. Machida, H. Hata, K. Okuno, G. Adachi, and J. Shiokawa,
   J. Inorg. Nucl. Chem., 41, 1425 (1979).
2. Luminescence Properties of Eu(II)-Borates and Eu^{2+}-Activated Sr-

Borates,
K. Machida, G. Adachi, and J. Shiokawa,
J. Lumin., 21, 101 (1979).

3. Structure of Divalent-Europium Metaborate,
K. Machida, G. Adachi, and J. Shiokawa,
Acta Crystallogr., Sect. B, 35, 149 (1979).

4. Structure of Europium(II) Tetraborate,
K. Machida, G. Adachi, and J. Shiokawa,
Acta Crystallogr., Sect. B, 36, 2008 (1980).

5. The Crystal Structure and Magnetic Property of Europium(II) Orthoborate,
K. Machida, G. Adachi, H. Hata, and J. Shiokawa,
Bull. Chem. Soc. Jpn., 54, 1052 (1981).

6. Synthesis and Characterization of Europium(II)-Haloborates,
K. Machida, T. Ishino, G. Adachi, and J. Shiokawa,
Mater. Res. Bull., 14, 1529 (1979).

7. Crystal Structure of Europium(II) Bromoborate,
K. Machida, G. Adachi, N. Yasuoka, N. Kasai, and J. Shiokawa,
Inorg. Chem., 19, 3807 (1980).

8. The Crystal Structure and Luminescence Properties of Europium(II) Haloborates,
K. Machida, G. Adachi, Y. Moriwaki, and J. Shiokawa,
Bull. Chem. Soc. Jpn., 54, 1048 (1981).

9. Synthesis and Magnetic Property of Europium(II) Haloborates, Eu_2BO_3X (X=Cl and Br),
K. Machida, G. Adachi, and J. Shiokawa,
Chem. Lett., in press.

10. High-Pressure Synthesis and Properties of Eu(II)-Metaborate,
K. Machida, G. Adachi, J. Shiokawa, M. Shimada, and M. Koizumi,
Chem. Lett., 1980, 81.

11. High-Pressure Synthesis, Characterization, and Properties of Europium(II) Metaborate and Europium(II)-Activated Strontium and Calcium Metaborates,
K. Machida, G. Adachi, J. Shiokawa, M. Shimada, and M. Koizumi,

Inorg. Chem., 19, 983 (1980).

12. Luminescence of High-Pressure Phases of Eu^{2+}-Activated SrB_2O_4, K. Machida, G. Adachi, J. Shiokawa, M. Shimada, and M. Koizumi, J. Lumin., 21, 233 (1980).
13. Structure of Strontium Tetraaluminate β-$SrAl_4O_7$, K. Machida, G. Adachi, J. Shiokawa, M. Shimada, and M. Koizumi, Acta Crystallogr., Sect. B, in press.
14. Structure and High-Pressure Polymorphism of Strontium Metasilicate, K. Machida, G. Adachi, J. Shiokawa, M. Shimada, and M. Koizumi, Acta Crystallogr., Sect. B, in press.
15. High-Pressure Synthesis and Characterization of Europium(II) Metasilicate, $EuSiO_3$, K. Machida, G. Adachi, J. Shiokawa, M. Shimada, M. Koizumi, K. Suito, and A. Onodera, Chem. Lett., 1980, 1111.
16. High-Pressure Synthesis, Crystal Structures, and Luminescence Properties of Europium(II) Metasilicate and Europium(II)-Activated Calcium and Strontium Metasilicates, K. Machida, G. Adachi, J. Shiokawa, M. Shimada, M. Koizumi, K. Suito, and A. Onodera, Inorg. Chem., in press.
17. Spectroscopic Properties for High-Pressure Polymorphs of Calcium and Strontium Metasilicates, K. Machida, G. Adachi, and J. Shiokawa, Bull. Chem. Soc. Jpn., in contribution.
18. Luminescence Properties for the High-Pressure Polymorphs of $CaSiO_3:Pb^{2+}$ and $SrSiO_3:Pb^{2+}$, K. Machida, G. Adachi, N. Ito, J. Shiokawa, M. Shimada, and M. Koizumi, Mater. Res. Bull., in contribution.

1. SYNTHESIS AND PROPERTIES OF BORATES IN THE BINARY SYSTEM $EuO-B_2O_3$

1-1. Introduction

Many Eu^{2+}-containing compounds have been synthesized because of their magnetic and luminescent properties. Several europium(II) mixed oxides with network-former oxides, e.g., Eu_2SiO_4, Eu_3SiO_5, $Eu_3Al_2O_6$, and $Eu_3P_2O_8$, have been found to be ferromagnetic at low temperatures.3) These mixed oxides can be prepared in virtually transparent single crystal forms, and hence they are interested in magneto-optic applications.7) The luminescent properties of Eu^{2+}-activated alkaline earth compounds also have been studied with a view to obtaining violet-blue to green emitting phosphors. A borate $BaB_8O_{13}:Eu^{2+}$ has been reported to be an efficient photoluminescent material and shows a deep-blue band emission.12)

A network-former oxide B_2O_3 gives a series of borates with various compositions reacting with network-modifier oxides. Since these borates generally consist of the linear or three-dimensional borate anions condensed with BO_3 triangular or BO_4 tetrahedral units, their crystal structures are complicated. The systematic IR spectral analyses on a number of borates have been made by Weir and Schroeder19) in order to investigate the structures of glassy and crystalline borates.

In this study, the borates in the binary system $EuO-B_2O_3$ have been prepared, viz., EuB_4O_7, EuB_2O_4, and $Eu_2B_2O_5$, and the single crystals of these europium(II) borates and $Eu_3B_2O_6$20) have been grown using Bridgeman, slowly cooling, and flux methods. This chapter describes their characterizations by X-ray analyses and IR spectrum, magnetic susceptibility, and luminescent spectrum measurements.

1-2. Experimental

A. Sample preparations. The europium(II) borates were prepared in the following way: the appropriate amounts of Eu_2O_3 (99.9 %), H_3BO_3 (99.5 %), and B (99.0 %) were fully mixed, pelletized, and heated at

950-1000°C for 3 h in vacuum (about 10^{-4} mmHg) after preheating at 200 -300°C. The preparation method of $Eu_3B_2O_6$ has been described in ref. 20.

The conditions and methods for the crystal growth of samples are summarized in Table I. The congruent melting points of resulting materials were 985±10°C for EuB_4O_7 and 1000±30°C for EuB_2O_4 and $Eu_2B_2O_5$ respectively. That of $Eu_3B_2O_6$ was not observed. The single crystals obtained had the following colors and shapes: pale-gray prism, EuB_4O_7; light-yellow needle, EuB_2O_4; yellow plate, $Eu_2B_2O_5$; black hexagonal prism, $Eu_3B_2O_6$.

Table I. Summary of crystal growth for a series of europium(II) borates

Borate	M.P. (°C)	Method of crystal growth	Crystal		
			Color	Habit	Dimension (mm)
EuB_4O_7	985	Bridgeman (1050→900°C,5°C/h)	Pale-gray	Prism	∿0.4
EuB_2O_4	≃1000	Slowly cooling (1050→950°C,20°C/h)	Light-yellow	Needle	∿3.0
$Eu_2B_2O_5$	≃1000	NaCl-KCl flux (950→750°C,3°C/h)	Yellow	Plate	∿0.2
$Eu_3B_2O_6$	—	KCl flux (1050→750°C,3°C/h)	Black	Hexagonal prism	∿0.1

The preparation of Eu^{2+}-activated strontium borates (viz., SrB_4O_7, SrB_2O_4, $Sr_2B_2O_5$, and $Sr_3B_2O_6$) was carried out by heating the intimate mixtures of H_3BO_3 and $SrCO_3:Eu^{3+}$, coprecipitated from a dilute HCl solution of a reagent grade $Sr(NO_3)_2$ and Eu_2O_3 (99.99 %) by the slow addition of a $(NH_4)_2CO_3$ solution, at 900-1000°C for 2 or 3 h in a reducing stream of H_2 or N_2 containing 5 mol% H_2. A borate, SrB_6O_{10}, cannot be obtained by the standard ceramic technique. Chenot[21)] has obtained it by heating a compound $SrO \cdot 3B_2O_3 \cdot 5H_2O$. Accordingly, $SrB_6O_{10}:Eu^{3+}$ was precipitated form the hot solution (about 95°C) by the slow addition of a dilute NH_4OH solution. When the precipitate was heating at 650°C for 3 h and 800°C for 2 h in H_2, $SrB_6O_{10}:Eu^{2+}$ formed, but its degree of crystallinity was low.

The resulting samples were checked by the powder X-ray analysis.

B. X-ray measurements. Preliminary Weissenberg photographs showed that the obtained crystals of EuB_4O_7, EuB_2O_4, and $Eu_3B_2O_6$ belong to the orthorhombic symmetry of space group Pnmm or $Pnm2_1$ (systematic absence: k+l=2n+1 for 0kl reflections), the orthorhombic symmetry of space group Pnca (systematic absences: k+l=2n+1 for 0kl reflections, l=2n+1 for h0l reflections, and h=2n+1 for hk0 reflections), and the trigonal system of space group R3c or $R\bar{3}c$ (systematic absences: h+k+l=3n+1 and 3n+2 for hkl reflections and l=2n+1 for h0l reflections), respectively. For $Eu_2B_2O_5$, no information on the crystal data was obtainable since the crystals used for X-ray measurements were twin crystals. From the similarity between the X-ray patterns of $Eu_2B_2O_5$ and $Sr_2B_2O_5$, however, they were found to be isostructural with each other. The cell parameters (Table II) were determined by a least-squares treatments of the X-ray

Table II. Crystal data and X-ray measurements for a series of europium(II) borates

	EuB_4O_7	EuB_2O_4	$Eu_2B_2O_5$	$Eu_3B_2O_6$
F.W.	307.20	237.58	405.54	573.50
Symmetry	Orthorhombic	Orthorhombic	Monoclinic	Trigonal
S.G.	$Pnm2_1$	Pnca	$P2_1/a$	$R\bar{3}c$
a (Å)	4.435(1)	6.593(1)	11.91(1)	9.069(1)
b (Å)	10.731(1)	12.063(2)	5.36(1)	
c (Å)	4.240(1)	4.343(1)	7.74(1)	12.542(2)
β (°)			92.7(1)	
V ($Å^3$)	201.8(2)	345.4(1)	494(2)	893.3(3)
Dm (g/cm^3)	5.01	4.61	5.45	6.31
Dx (g/cm^3)	5.08	4.57	5.37	6.40
Z	2	4	4	6
λ (Å)		0.71069		
μ(Mo Kα) (mm^{-1})	15.54	18.15	24.75	31.26
F(000)	273	420	704	1482

powder patterns (Cu $K\bar{\alpha}$ radiation: λ=1.5418 Å) calibrated with high purity silicon as an internal standard.

The intensity data were measured on a Rigaku automated four-circle diffractometer with Mo Kα radiation monochromated by a graphite plate using crystals of dimensions: 0.30×0.20×0.20 mm, EuB_4O_7; 0.15×0.15×0.30 mm, EuB_2O_4; 0.08 (side to side of hexagonal cross section) × 0.04 (thickness) mm. The ω-2θ scan method was employed at a scanning rate of 4°/min. The stationary-crystal and stationary-counter background counts were measured at beginning and end of the ω-2θ scan for one-fourth of the scan time taken on each reflection. All possible reflections were collected up to 2θ=60 or 70°. Three standard reflections were monitored every 60 or 100 reflections, and no apparent decay in intensity was detected. The numbers of observed reflections were 510 ($F_o>3\sigma_{F_o}$) for EuB_4O_7, 334 (nonzero) for EuB_2O_4, and 259 (nonzero) for $Eu_3B_2O_6$, respectively. The usual Lorentz and polarization corrections were applied, but the absorption and anomalous dispersion effects for heavy atoms were not considered.

C. Structure determinations and refinements. The structures of EuB_4O_7 was solved by the conventional heavy-atom method and refined with HBLS-V program[22)] by the block-diagonal least-squares method, the function minimized being $\Sigma w(|F_o|-|F_c|)^2$. From a three-dimensional Patterson synthesis, the noncentrosymmetric space group $Pnm2_1$ was adopted and the Eu atom was determined to be on a set of special positions, 2(a): x, 0, 0 with x=0.12. The remaining atoms (O and B) were located on successive Fourier maps: O(1) at the 2(a) site and the other atoms at general positions [4(b) sites]. Isotropic refinements for all atomic parameters gave R=0.023 and R_w=0.030 for 510 observed reflections, where $R=\Sigma||F_o|-|F_c||/\Sigma|F_o|$ and $R_w=[\Sigma w(|F_o|-|F_c|)^2/\Sigma w(F_o)^2]^{1/2}$. The weighting scheme $w=(F_m/F_o)^2$ for $F_o>F_m$ (=20.0) and w=1.0 for $F_o\leq F_m$ (= 20.0) was employed to determine the coordinates of the light atoms more accurately. The final positional and thermal parameters are listed in Table III.

The location of the Eu atom in EuB_2O_4 was determined by a three-dimensional Patterson map. Successive Fourier syntheses revealed the

Table III. Final positional and thermal parameters for EuB_4O_7, with their standard deviations in parentheses

	x	y	z	B ($Å^2$)
Eu	0.2116(3)	0	0	0.18(1)
O(1)	0.768(6)	0	0.581(7)	0.31(8)
O(2)	0.358(4)	0.141(4)	0.546(4)	0.25(5)
O(3)	0.727(4)	0.135(5)	0.134(5)	0.31(5)
O(4)	0.132(5)	0.278(4)	0.139(5)	0.27(5)
B(1)	0.672(5)	0.122(5)	0.463(7)	0.28(8)
B(2)	0.178(5)	0.251(5)	0.484(14)	0.47(8)

positions of the O and B atoms. All the atomic parameters were refined by the block-diagonal least-squares method to give R=0.029 and R_w=0.039. The weighting scheme used was $w=[\sigma(F_o)^2+a|F_o|+b|F_o|^2]^{-1}$, and the values of a and b used in the refinement were 0.1002 and 0.0004, respectively. The final positional and thermal parameters are listed in Table IV.

Table IV. Final positional and thermal parameters for EuB_2O_4, with their standard deviations in parentheses

Atom	x	y	z	U_{11}[a]	U_{22}	U_{33}	U_{12}	U_{13}	U_{23}
Eu	1/4	0	0.2610(1)	88(2)	67(2)	65(2)	0(2)	0	0
O(1)	0.0935(9)	0.0914(4)	0.7350(9)	77(20)	82(21)	86(22)	-22(20)	7(15)	4(16)
O(2)	0.1440(9)	0.2111(4)	0.1470(12)	233(28)	83(19)	74(23)	10(20)	1(21)	8(98)
B	0.1247(13)	0.1944(6)	0.8281(18)	112(32)	102(30)	91(32)	15(26)	6(28)	0(28)

[a] The form of the anisotropic thermal parameter (×10^4) is $\exp[-2\pi^2(U_{11}h^2a^{*2} + U_{22}k^2b^{*2} + U_{33}l^2c^{*2} + 2U_{12}hka^*b^* + 2U_{13}hla^*c^* + 2U_{23}klb^*c^*)]$.

The structure of $Eu_3B_2O_6$ was solved by the heavy-atom method and refined by the full-matrix least-squares method (FMLS program[23)]) based on the observed reflections, the function minimized being $\Sigma w(|F_o|-|F_c|)^2$ where w=1 for all $|F_o|$. From a three-dimensional Patterson synthesis, the centrosymmetric space group R$\bar{3}$c was chosen and the coordinate of Eu atom determined to be at a special position [18(e) site]. The remaining atoms (O and B) were located on the successive Fourier maps: O at the general position [36(d) site] and B at the 12(c) site on three-fold axis. Isotropic refinement for all atomic parameters was carried out to give R=0.082 for 259 observed reflections. The final positional and thermal parameters are given in Table V. The atomic scattering factors for Eu, O, and B atoms were those given in International Tables for X-Ray Crystallography.24)

Table V. Final positional and thermal parameters for $Eu_3B_2O_6$, with their standard deviations in parentheses

Atom	x	y	z	B (Å^2)
Eu	0.3075(18)	0	1/4	0.45(4)
O	0.164(23)	0.033(23)	0.396(18)	0.88(27)
B	0	0	0.39(6)	1.3(8)

D. Magnetic susceptibility and optical measurements. Magnetic susceptibilities of powdered samples were measured with a Shimadzu MB-11 magnetic balance over a temperature range of 2-300 K. Ultraviolet luminescent spectrum measurements were made at room temperature with a Shimadzu recording absolute spectrofluorophotometer,25) which can record the corrected excitation and emission spectra by the automatic compensation and precalibration systems for the instrumental factors, and its slit widths were routinely set at 10 nm for excitation spectra and 5 nm for emission spectra. The relative emission intensities of samples were measured by integrating the corresponding area below curves as " corrected emission spectra " under the excitation by a xenon lamp and with reference to a suitable standard phosphor, $CaWO_4:Pb^{2+}$ (NBS 1026). The relative emission intensity under 254 nm excitation at 300 K of the $CaWO_4:Pb^{2+}$ was defined as 76 %. Diffuse reflection spectra were measured with a Shimadzu multipurpose recording spectrophotometer equipped with an attachment for an integrating sphere. Magnesium oxide was used as the standard material, of which the reflection was defined as 100 %.

The IR spectral analysis was performed on a Hitachi Perkin-Elmer 225 grating spectrophotometer covering a range of 2000-200 cm^{-1}. Dry air was circulated through the spectrometer to eliminate interference from atmospheric moisture in the 400 cm^{-1} region. The samples were examined as a dispersion in potassium bromide, using the pressed disk technique, and 1 % mixtures were generally employed.

E. TGA and DTA measurements. The thermogravimetric analysis (TGA) and differential thermal analysis (DTA) were made on a series of europium(II) borates at 25-1000°C in air with a Rigaku DTA " Thermoflex." The heating rate employed was 10°C/min.

1-3. Results and discussion

A. Crystal structures. The interatomic distances and angles are summarized in Table VI and the projections of the EuB_4O_7 structure viewed along the c and a axes are shown in Figs. 1 and 2. The atoms,

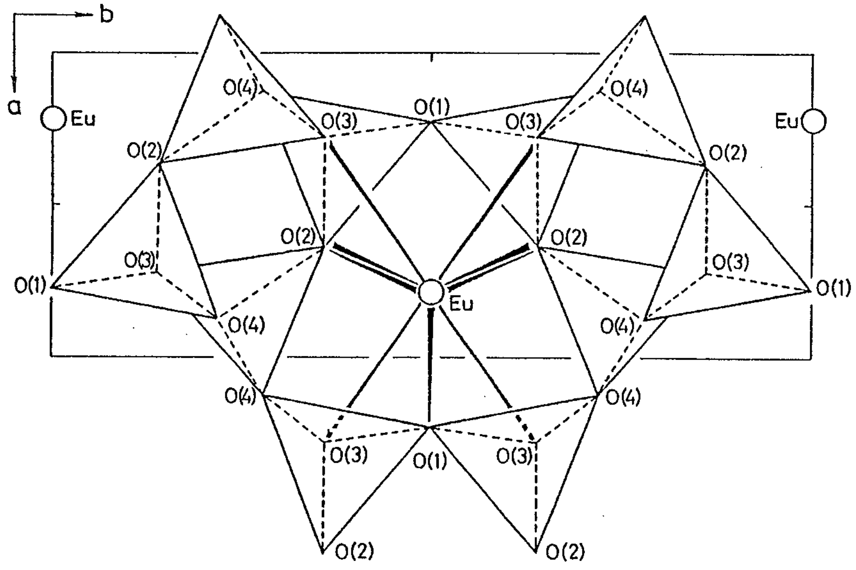

Figure 1. A projection of the EuB_4O_7 structure viewed along the c axis.

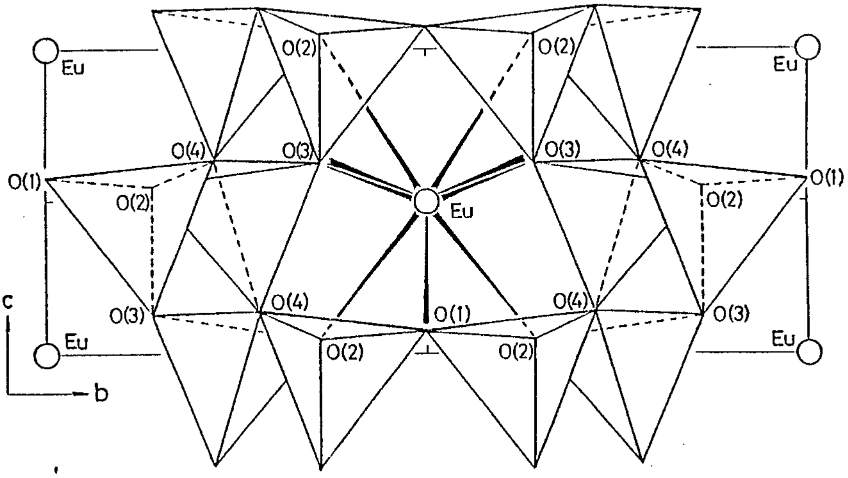

Figure 2. A projection of the EuB_4O_7 structure viewed along the a axis.

Eu and O(1), are located on mirror planes, y=0 and 1/2. There are two kinds of borate units, $B(1)O_4$ and $B(2)O_4$, with mean B-O distances 1.479 and 1.486 Å respectively and mean O-B-O angle 109.4°. The structure consists of a three-dimensional $(B_4O_7)_\infty$ network in which the $B(1)O_4$ and $B(2)O_4$ tetrahedra are alternately linked by sharing cornered O atoms. The Eu atoms are located in a so-called " cage " formed by the BO_4 units of the $(B_4O_7)_\infty$ network and have four nearest and twelve next-

Table VI. Interatomic distances (Å) and angles (°) in EuB_4O_7

Standard deviations are given in parentheses.

(*a*) The $(B_4O_7)_\infty$ network

B(1)-tetrahedron		B(2)-tetrahedron	
B(1)–O(1)	1·465 (10)	B(2)–O(2)	1·449 (14)
–O(2)	1·451 (8)	–O(3^{i})	1·436 (15)
–O(3)	1·427 (8)	–O(4)	1·503 (14)
–O(4^{i})	1·573 (8)	–O(4^{ii})	1·556 (14)
Average	1·479	Average	1·486
O(1)–B(1)–O(2)	108·8 (6)	O(2)–B(2)–O(3^{i})	116·9 (10)
O(1)–B(1)–O(3)	111·9 (6)	O(2)–B(2)–O(4)	114·0 (10)
O(1)–B(1)–O(4^{i})	106·8 (6)	O(2)–B(2)–O(4^{ii})	104·3 (9)
O(2)–B(1)–O(3)	113·0 (6)	O(3^{i})–B(2)–O(4)	108·1 (9)
O(2)–B(1)–O(4^{i})	108·7 (5)	O(3^{i})–B(2)–O(4^{ii})	103·8 (9)
O(3)–B(1)–O(4^{i})	107·4 (5)	O(4)–B(2)–O(4^{ii})	109·1 (9)
Average	109·4	Average	109·4

(*b*) Eu–Eu distances

Nearest neighbors		Next-nearest neighbors	
Eu–Eu^{i}	4·240 (1) (×2)	Eu–Eu^{iii}	6·136 (1) (×4)
–Eu^{ii}	4·435 (1) (×2)	–Eu^{iv}	6·311 (1) (×4)
Average	4·338	–Eu^{v}	6·067 (1) (×4)
		Average	6·171

(*c*) Eu–O distances

Eu–O(1^{i})	2·651 (7)	Eu–O(3)	2·768 (5) (×2)
–O(2)	2·841 (4) (×2)	–O(3^{ii})	2·653 (5) (×2)
–O(2^{i})	2·531 (4) (×2)	Average	2·693

Symmetry code: Eu^{i} $(x, 0, \pm 1)$, Eu^{ii} $(\pm 1 + x, 0, 0)$, Eu^{iii} $(\pm 1 + x, 0, \pm 1)$, Eu^{iv} $(x, \pm\frac{1}{2}, \pm\frac{1}{2})$, Eu^{v} $(1 - x, \pm\frac{1}{2}, \pm\frac{1}{2})$, O(1^{i}) $(-1 + x, 0, -1 + z)$, O(2^{i}) $(x, \pm y, -1 + z)$, O(3^{i}) $(-x, \frac{1}{2} - y, \frac{1}{2} + z)$, O(3^{ii}) $(-1 + x, \pm y, z)$, O(4^{i}) $(1 - x, \frac{1}{2} - y, \frac{1}{2} + z)$, O(4^{ii}) $(-x, \frac{1}{2} - y, \frac{1}{2} + z)$.

nearest neighboring Eu atoms with mean interatomic distances 4.338 and 6.171 Å. Each Eu atom is surrounded by nine O atoms at individual distances varying from 2.531 to 2.841 Å to form EuO_9 polyhedron (Fig. 3).

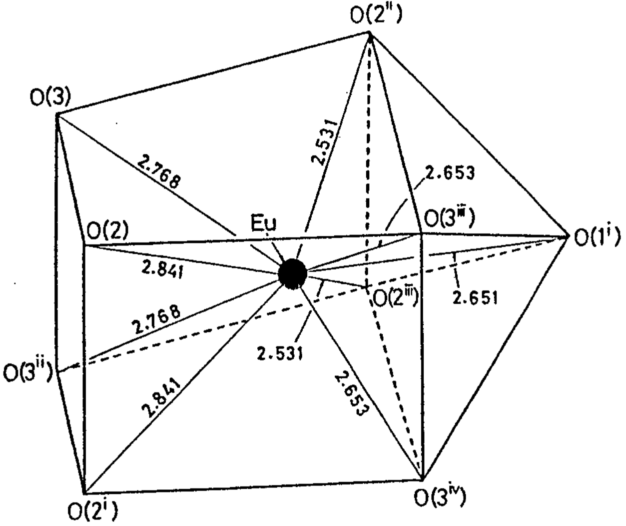

Figure 3. A schematic illustration of the EuO_9 polyhedron in EuB_4O_7. The numerical values represent Eu-O nearest-neighbor distances (Å).

The projections of the EuB_2O_4 structure viewed along the a and c axes are shown in Figs. 4 and 5, respectively. The interatomic distances and angles are presented in Table VII. The final parameters (see Table IV) were found to agree with those of CaB_2O_4.[26)] Therefore, EuB_2O_4 is isostructural with CaB_2O_4.

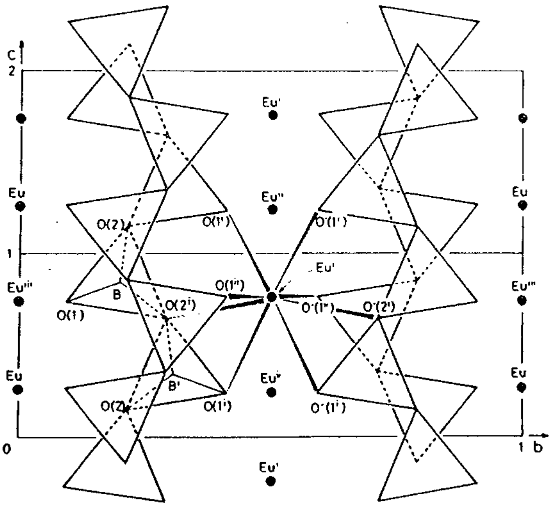

Figure 4. A projection of the EuB_2O_4 structure viewed along the a axis.

The B-O distances are 1.32, 1.41, and 1.39 Å. The short bond B-O(1) involving the unshared O(1) atom in the $(BO_2)_\infty$ chain may be ascribed to the next-nearest neighbor interaction between Eu and B atoms since O(1) is shared between the BO_3 triangle and the EuO_8 dodecahedron. The B-O(2)-B^i

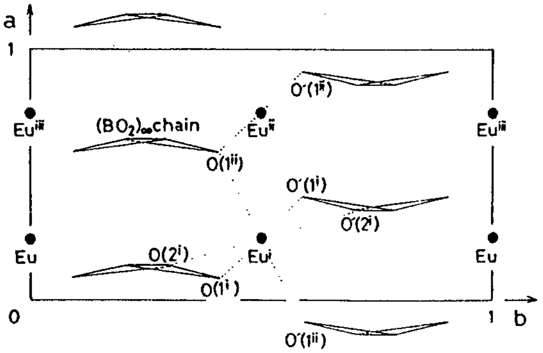

Figure 5. A projection of the EuB_2O_4 structure viewed along the c axis.

angle (131.8°) closely agrees with the corresponding angle (131.5°) in a pyroborate group, B_2O_5, of $Mg_2B_2O_5$ reported by Takeuchi.$^{27)}$

Each Eu atom is surrounded by eight O atoms to form a distorted EuO_8 dodecahedron with individual Eu–O distances varying from 2.519 to 2.738 Å (see Table VII).

The crystal structure of $Eu_3B_2O_6$ is shown in Fig. 6, and the bond lengths and angles are given in Table VIII. This borate contains isolated and planar triangles of BO_3 groups with a B-O distance of 1.36 Å like other orthoborates,$^{28)}$ the crystal lattice consisting of Eu atoms and BO_3 groups hexagonally packed along the c axis. The triangle planes of BO_3 groups are perpendicular to

Table VII. Interatomic distances (Å) and angles (°) in EuB_2O_4

Standard deviations are given in parentheses.

(*a*) The $(BO_2)_\infty$ chain			
Distances			
B–O(1)	1·32 (1)	O(1)–O(2)	2·323 (8)
–O(2)	1·41 (1)	–O(2^{i})	2·435 (8)
–O(2^{i})	1·39 (1)	O(2)–O(2^{i})	2·365 (8)
B–B^{i}	2·55 (1)		
Angles			
O(1)–B–O(2)	116·7 (7)	O(1)–B–O(2^{i})	127·7 (7)
O(2)–B–O(2^{i})	115·6 (7)	B–O(2)–B^{i}	131·8 (7)
(*b*) Eu–Eu distances			
Nearest neighbors		Next-nearest neighbors	
Eu^{i}–Eu$^{i'}$	4·342 (1) (×2)	Eu^{i}–Eu$^{i''}$	6·593 (1) (×2)
–Eu^{ii}	4·001 (1) (×2)	–Eu	6·410 (1) (×4)
–Eu$^{ii'}$	3·896 (1) (×2)	–Eu^{iii}	6·874 (1) (×4)
Average	4·080	Average	6·632
(*c*) Eu–O distances			
Eu^{i}–O(1^{i})	2·738 (6) (×2)	Eu^{i}–O(1^{ii})	2·519 (6) (×2)
–O(2^{i})	2·687 (6) (×2)	Eu^{ii}–O(1^{ii})	2·553 (6) (×2)
	Average	2·624	
(*d*) Eu–O–Eu angles			
Eu^{i}–O(1^{i})–Eu$^{i'}$	110·3 (2)	Eu^{i}–O(1^{i})–Eu$^{ii'}$	100·4 (2)
Eu^{i}–O(1^{i})–Eu^{ii}	99·0 (2)	Eu^{i}–O(1^{ii})–Eu$^{ii'}$	100·4 (2)
Eu^{i}–O(1^{ii})–Eu^{ii}	99·0 (2)		

Symmetry transformations: Eu^{i} $(\frac{1}{4}, \frac{1}{2}, \frac{1}{2}+z)$, Eu$^{i'}$ $(\frac{1}{4}, \frac{1}{2}, -\frac{1}{2}+z; \frac{1}{4}, \frac{1}{2}, \frac{3}{2}+z)$, Eu$^{i''}$ $(-\frac{3}{4}, \frac{1}{2}, \frac{1}{2}+z; \frac{5}{4}, \frac{1}{2}, \frac{1}{2}+z)$, Eu^{ii} $(\frac{3}{4}, \frac{1}{2}, \frac{1}{2}-z)$, Eu$^{ii'}$ $(-\frac{1}{4}, \frac{1}{2}, \frac{3}{2}-z; \frac{3}{4}, \frac{1}{2}, \frac{3}{2}-z)$, Eu^{iii} $(\frac{3}{4},0,\bar{z})$, B^{i} $(x, \frac{1}{2}-y, \frac{1}{2}+z)$, O(1^{i}) $(x, \frac{1}{2}-y, \frac{1}{2}+z; \frac{1}{2}-x, \frac{1}{2}+y, \frac{1}{2}+z)$, O(1^{ii}) $(\frac{1}{2}+x, \frac{1}{2}-y, \frac{1}{2}-z; x, \frac{1}{2}+y, \frac{1}{2}-z)$, O(2$'$) $(x, \frac{1}{2}-y, \frac{1}{2}+z; \frac{1}{2}-x, \frac{1}{2}+y, \frac{1}{2}+z)$.

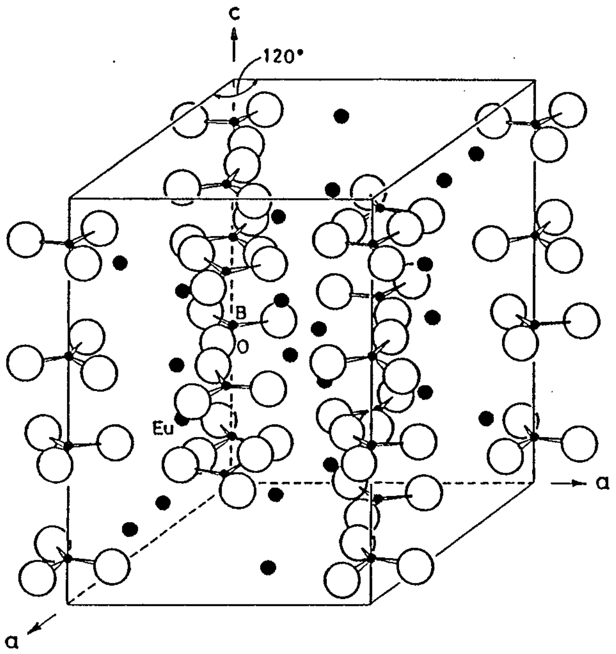

Figure 6. Crystal structure of $Eu_3B_2O_6$.

the c axis. Each Eu atom is surrounded by 8 oxygens to form an EuO_8 polyhedron with Eu-O distances varying from 2.36 to 2.95 Å (Fig. 7). An Eu atom has 8 nearest and 6 second-nearest neighboring Eu atoms with the mean interatomic distances 3.816 and 5.244 Å, respectively.

The IR spectral data of europium(II) borates are given in Table IX. The spectra of EuB_2O_4, $Eu_2B_2O_5$, and $Eu_3B_2O_6$ were able to be ascribed to the vibrations of isolated, planar, and trigonal BO_3 group. For

Table VIII. Interatomic distances (Å) and angles (°) in $Eu_3B_2O_6$

Standard deviations are given in parentheses.

(a) The BO_3 triangle			
B–O	1.36(6)	O–B–O	120(0)
(b) Eu–Eu distances			
Nearest neighbors		Second-nearest neighbors	
Eu–Eu^{I}	3.509(3)	Eu–Eu^{IV}	5.450(3)
–Eu^{II}	3.778(3)	–Eu^{V}	4.831(3)
–Eu^{III}	4.200(3)		
(c) Eu–O distances			
Eu–O^{I}	2.92(3)	Eu–O^{III}	2.95(3)
–O^{II}	2.58(3)	–O^{IV}	2.36(3)
(d) Eu–O–Eu angles			
Nearest neighbors		Second-nearest neighbors	
Eu–O–Eu^{I}	82.7(7)	Eu–O–Eu^{IV}	166.0(4)
–O–Eu^{II}	80.1(6)		
	85.9(7)		
	99.8(8)		
–O–Eu^{III}	103.9(8)		

Symmetry code: Eu^{I} (1/3−x, −1/3, 1/6+z; 2/3−x, 1/3, 1/3−z), Eu^{II} (1/3, 2/3−x, 1/6+z; 1/3+x, −1/3+x, 1/6+z: 2/3, 1/3−x, 1/3−z; −1/3+x, −2/3+x, 1/3−z), Eu^{III}(−1/3+x, 1/3, 1/3+z; 1/3−x, 2/3−x, −1/3+z), Eu^{IV}(1−x, 1−x, z; 1, x, z; 1−x, −x, z; 0, −1+x, z), Eu^{V}(0, x, z; −x, −x, z), O^{I} (x, y, z; x−y, −y, 1/2−z), O^{II} (2/3−x+y, 1/3+y, −1/6+z; 1/3−x, −1/3−y, 2/3−z), O^{III} (2/3−y, 1/3−x, −1/6+z; 1/3+x−y, −1/3+x, 2/3−z), O^{IV} (2/3−x, 1/3−x+y, 5/6−z; 1/3−y, −1/3+x−y, 1/3+z).

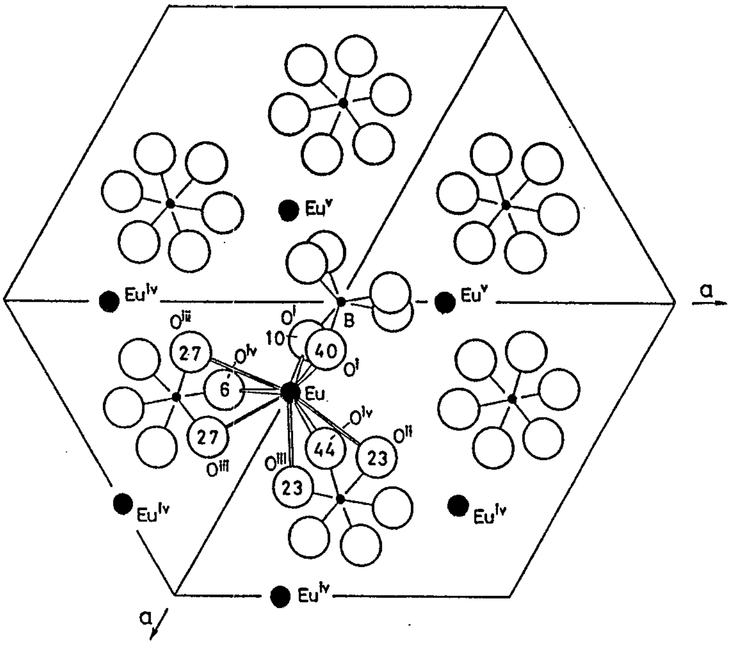

Figure 7. A projection between Z=0 and 0.5 of the $Eu_3B_2O_6$ structure viewed along the c axis. Numerical values give the fractional Z coordinates of O atoms.

the BO_3 group of D_{3h} symmetry, there are four fundamental modes of vibration: ν_1, symmetrical strech (950 cm^{-1}); ν_2, out-of-plane (750 cm^{-1}); ν_3, antisymmetrical strech (1250 cm^{-1}); ν_4, in-plane bend (600 cm^{-1}).

In the IR spectra of EuB_2O_4, the bands between 1450 and 1050 cm^{-1} are derived from the ν_3. The 980 cm^{-1} absorption corresponds to the ν_1, and the bands below 750 cm^{-1} are derived from the distortion modes ν_2 and ν_4.

In those of $Eu_2B_2O_5$, the group of bands between 1400 and 1100 cm^{-1} corresponds to the modes originated from the ν_3. The symmetric streching mode (ν_1) can be identified with the frequency at 999 cm^{-1}, and the

Table IX. IR spectra for a series of europium(II) borates (cm^{-1})[a]

Mode	EuB_2O_4		$Eu_2B_2O_5$		$Eu_3B_2O_6$		EuB_4O_7	
			1510	w			1450	mvb
	1420	s	1398	sb			1310	mb
			1380	sb			1222	sb
			1341	sb			1192	sb
ν_3			1319	sb	1300 -		1160	sb
			1262	sb			1100	sb
			1220	sb	1000		1020	svb
	1167	s	1165	sb			970	sb
	1060	mb	1120	sb			905	mb
							886	s
ν_1	980	mb	999	m	1000	m	812	sb
							777	sb
	768	w	745	s	881	w	725	m
	732	m	732	s	783	w	705	mb
ν_2	700	m	723	s	773	vw	658	s
					747	w	644	s
					715	vs	626	s
							554	s
ν_4	685	s	658	m	612	m	532	w
	636	s	620	s	600	s	515	w
							470	w
							445	mb
							418	m
	$(BO_2)_\infty$ chain		$B_2O_5^{4-}$ ion		BO_3^{3-} ion		BO_4 tetrahedron	

[a] The characters of absorption bands: s, strong; m, medium; w, weak; v, very; b, broad.

bands below 750 cm^{-1} are due to the distortion modes ν_2 and ν_4. This IR pattern is closely similar to that of $Sr_2B_2O_5$ which contains $B_2O_5^{4-}$ ions.[29)] Consequently, the absorption bands of $Eu_2B_2O_5$ are attributed to the anions.

For $Eu_3B_2O_6$, the assignment of the spectrum pattern can be directly made on the basis of the modes derived from the above-mentioned BO_3 group. It should be concluded that this borates contains BO_3^{3-} ions in a similar manner as a series of alkaline earth orthoborates without $Be_3B_2O_6$.

The IR spectra of EuB_4O_7 is similar to those of SrB_4O_7 and PbB_4O_7, which have been found to be consist of a three-dimensional network of BO_4 tetrahedra.[30)] Therefore, the structural framework of EuB_4O_7 seems to be the same network as them.

B. Magnetic properties. The magnetic data for a series of europium(II) borates are summarized in Table X. The effective magnetic moment per Eu^{2+} ion of EuB_4O_7, EuB_2O_4, and $Eu_2B_2O_5$ were 8.02, 8.00, and 7.72 μ_B, which are in good agreement with the theoretical value of 7.94 μ_B. Therefore, the ions of Eu seem to be in divalent state. The borate, $Eu_3B_2O_6$, in which the EuO content is the most among these borates, has been found to be a ferromagnet with T_C=7.5 K and its paramagnetic Curie

Table X. Magnetic properties for a series of europium(II) borates

Borate	Magnetism	μ_{eff} $(\mu_B)^a$	T_C (K)	T_N (K)	θ_C $(K)^b$
EuB_4O_7	Para.	8.02	—	—	0
EuB_2O_4	Antiferro.	8.00	—	≃3	-5
$Eu_2B_2O_5$	Para.	7.72	—	—	-1
$Eu_3B_2O_6{}^c$	Ferro.	7.74	7.5	—	8

[a] Magnetic moment per Eu^{2+} ion. The theoretical value is 7.94 μ_B.

[b] Paramagnetic Curies temperature. [c] See ref. 20.

temperature θ_C is 8 K.[20)] The magnetic susceptibilities of EuB_4O_7 and $Eu_2B_2O_5$ obeyed the Curie Weiss law in the corresponding ranges of measured temperatures. On the other hand, EuB_2O_4 was an antiferromagnet with a Neel point $T_N \simeq 3$ K and the value of θ_C was -5 K, although it was expected for this borate to be paramagnetic because the EuO content in EuB_2O_4 was less than that in $Eu_2B_2O_5$. These magnetisms were understood by considering the relationship between their crystal structures and magnetic interactions in the following.

Kasuya[8b)] has suggested that the magnetism of europium(II) compounds is attributable to the magnetic exchange and superexchange interactions taking place via the overlap of 4f and 5d orbitals between neighboring Eu^{2+} ions. The magnetism of highly symmetrical compounds, EuO (T_C=69 K),[2a,b)] $EuTiO_3$ (T_N=5.3 K),[4a)] and Eu_2TiO_4 (T_C=9 K),[4b)] has been interpreted in terms of the magnitude of the magnetic interactions between the nearest and second-nearest neighboring Eu^{2+} ions. The direct Eu^{2+}-Eu^{2+} interactions between the nearest Eu neighbors are responsible for the ferromagnetic interaction, the 90°Eu^{2+}-O^{2-}-Eu^{2+} superexchange pairs undergoing the antiferromagnetic interaction via the O^{2-} ions at an angle of 90°. The 180°Eu^{2+}-O^{2-}-Eu^{2+} superexchange interactions between the second-nearest Eu neighbors contribute to the overall magnetism, ferromagnetically or antiferromagnetically, as the case may be. The difference among the magnetic properties of europium(II) compounds results from the difference in magnitude for the abovementioned interactions.

From the Heisenberg model and molecular field approximation, McGuire et al.[2a,b),4a)] have expressed the θ_C and T_N values as follows:

$$\theta c = \frac{2}{3k} S(S+1)(Z_1 J_1 + Z_2 J_2) \qquad (1\text{-}1)$$

$$T_N = -\frac{2}{3k} \epsilon S(S+1)(Z_1 J_1 + Z_2 J_2) \qquad (1\text{-}2)$$

where J_1 and J_2 denote the effective exchange integrals between the nearest and second-nearest neighboring Eu^{2+} ions, Z_1 and Z_2 the numbers of the nearest and second-nearest Eu neighbors, and ε a numerical factor equal to unity in the molecular field theory. For the oxides, EuO, EuTiO$_3$, and Eu$_2$TiO$_4$, the direct Eu^{2+}-Eu^{2+} exchange and indirect 90° Eu^{2+}-O^{2-}-Eu^{2+} superexchange interactions are responsible for J_1, positively and negatively, respectively. The 180°Eu^{2+}-O^{2-}-Eu^{2+} superexchange interactions contribute to the value of J_2. The magnitude of direct exchange interactions is strongly influenced by the Eu-Eu distance, but that of superexchange interactions is not.

Each Eu^{2+} ion in Eu$_3$B$_2$O$_6$ has 8 nearest and 6 second-nearest neighboring Eu^{2+} ions. The nearest Eu neighbors with the interatomic distances of 3.509 and 3.778 Å contribute as the exchange and superexchange pairs, but not the nearest Eu neighbors with 4.200 Å, the distance of 4.200 Å appearing to be too great to interact with the neighboring Eu^{2+} ions as judged by the cases of other europium(II) compounds. For example, the mean distance between the nearest Eu neighbors in EuB$_4$O$_7$ (paramagnet) is 4.338 Å and insufficient for the magnetic interactions. Among the nearest Eu neighbors, therefore, we can point out two kinds of effective exchange pairs (Fig. 8). Type 1: the Eu-Eu^{i} pair with two 82.7°Eu^{2+}-O^{2-}-Eu^{2+}; Type 2: the Eu-Eu^{ii} pair

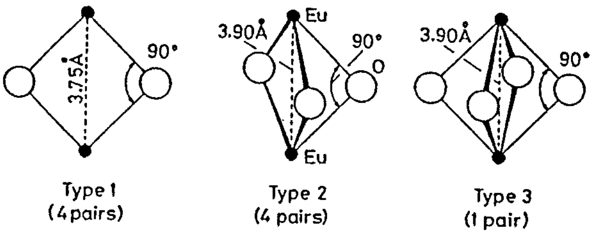

(a) Eu$_2$TiO$_4$

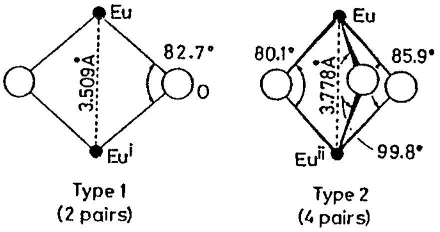

(b) Eu$_3$B$_2$O$_6$

Figure 8. Anions environments around exchange pairs between nearest neighboring Eu^{2+} ions in Eu$_2$TiO$_4$ and Eu$_3$B$_2$O$_6$.

with three 80.1-99.8°Eu^{2+}-O^{2-}-Eu^{2+}.

For the second-nearest Eu neighbors, four Eu-Eu^{iv} pairs via an O^{2-} ion at 166.0° correspond to the 180°Eu^{2+}-O^{2-}-Eu^{2+} superexchange pairs in EuO, $EuTiO_3$, and Eu_2TiO_4, although the Eu-O-Eu angle somewhat deviates from the value of 180°. The remaining two Eu-Eu^{V} pairs cannot be regarded as the superexchange pairs because no oxygen occupies the position between them.

Greedan and McCarthy[4b)] estimated the values of exchange integrals J_1/k and J_2/k of Eu_2TiO_4 to confirm agreement with the experimental value (θ_C=10 K) using Eg. (1-1): J_1/k=0.07 and J_2/k=0.04 K (Table XI).

Table XI. Magnetic exchange and superexchange interactions in Eu_2TiO_4 and $Eu_3B_2O_6$

	Eu_2TiO_4[a]	$Eu_3B_2O_6$
T_C (K)	9	7.5
θ_C (K)	10	8
Nearest neighbors	5 Eu^{2+} at 3.90 Å 4 Eu^{2+} at 3.75	2 Eu^{2+} at 3.509 Å 4 Eu^{2+} at 3.778
Second-nearest neighbors	8 Eu^{2+} at 5.51	4 Eu^{2+} at 5.450
Interactions contributing to J_1	Eu^{2+}-Eu^{2+}(+) 90°Eu^{2+}-O^{2-}-Eu^{2+}(-)	Eu^{2+}-Eu^{2+}(+) 80.1$\sim$99.8°Eu^{2+}-O^{2-}-Eu^{2+}(-)
Resultant J_1/k (K)	0.07	0.10
Interactions contributing to J_2	180°Eu^{2+}-O^{2-}-Eu^{2+}	166.0°Eu^{2+}-O^{2-}-Eu^{2+}
Resultant J_2/k (K)	0.04	0.04

[a] Ref. 4b.

An Eu^{2+} ion in Eu_2TiO_4 is surrounded by 9 nearest and 8 second-nearest neighboring Eu^{2+} ions with the interatomic distances of 3.75 to 3.90 Å and 5.51 Å, respectively. The Eu-Eu distances and Eu-O-Eu angles in Eu_2TiO_4 are closely similar to those of $Eu_3B_2O_6$.

In Eu_2TiO_4, there are three kinds of exchange pairs between the nearest Eu neighbors, Types 1 and 2 correspond to those of $Eu_3B_2O_6$, the Eu–Eu distances in the borate being smaller than those in the titanate (Fig. 8). The exchange pair (Type 3), which is the pair with four 90° Eu^{2+}-O^{2-}-Eu^{2+} and contributes antiferromagnetically to the overall magnetism in a similar manner to that of the exchange pairs in $EuTiO_3$, does not exist in $Eu_3B_2O_6$. Thus, $Eu_3B_2O_6$ is expected to give the greater values of J_1/k than Eu_2TiO_4. The superexchange pairs between the second-nearest Eu neighbors in Eu_2TiO_4 and $Eu_3B_2O_6$ should gives similar values of J_2/k from the similarity of the Eu–Eu distances and Eu–O–Eu angles. From the observed θ_C value of 8 K, we can estimate the values of J_1/k and J_2/k to be 0.10 and 0.04 K, substituting $S=7/2$, $Z_1=6$, and $Z_2=4$ into Eq. (1-1). It is concluded that the 166.0°Eu^{2+}-O^{2-}-Eu^{2+} superexchange pairs contribute ferromagnetically and the ferromagnetism of $Eu_3B_2O_6$ is attributable to the direct Eu^{2+}-Eu^{2+} and the 166.0°Eu^{2+}-O^{2-}-Eu^{2+} ferromagnetic interactions.

An Eu^{2+} ion in EuB_2O_4 is surrounded by 8 oxygens to form an EuO_8 dodecahedron. Since the endless chains of BO_3 triangular units extend in parallel with the c axis, all Eu^{2+} ions are located in the (010) and (020) planes. Each Eu^{2+} ion has 6 nearest Eu neighbors, 2 at 3.896, 4 at 4.001, and 2 at 4.342 Å, and 10 second-nearest Eu neighbors, 4 at 6.874, 4 at 6.410, and 2 at 6.593 Å (see Table VII). Particularly, all nearest Eu neighbors exist only in the (010) or (020) plane.

The value of J_1 in $EuTiO_3$, which is responsible for the exchange and superexchange pairs between the nearest Eu neighbors (Type 3), is antiferromagnetic and small since the increased Eu–Eu distance (3.90 Å) dictates a weak ferromagnetic interaction and the presence of the additional anion pair doubles the number of possible 90°Eu^{2+}-O^{2-}-Eu^{2+} superexchange interactions over that in Eu_2TiO_4 (Type 1).

For EuB_2O_4, there are two types among the 6 exchange pairs. One type (Type 3) contains 4 exchange pairs and is closely similar to that found in $EuTiO_3$. The distances between nearest Eu neighbors in EuB_2O_4 (3.896 and 4.001 Å) are roughly equal to that in $EuTiO_3$, and each exchange pair has the same anion coordination as in $EuTiO_3$ although the

Eu-O-Eu angles (99.0 and 100.4°) somewhat deviate from the value of 90°. The contribution of this type to J_1 seems to be approximately equivalent to that of the type in $EuTiO_3$. For another type (Type 1), the Eu-Eu distance (4.342 Å) is longer than that in $EuTiO_3$ and the Eu-O-Eu angle (110.3°) largely deviates from the value of 90°. Therefore, the J_1 for this type must be dominated by neither the positive Eu^{2+}-Eu^{2+} interaction nor the negative 90°Eu^{2+}-O^{2-}-Eu^{2+} interaction and its magnitude seems to be very small. Consequently, it is concluded that the overall J_1 in EuB_2O_4 is antiferromagnetic ($Z_1J_1/k<0$ K).

The distances between the second-nearest Eu neighbors (6.874, 6.410, and 6.593 Å) are much longer than that in $EuTiO_3$ and Eu_2TiO_4 (5.51 Å) and the Eu-O-Eu angles (154, 140, and 125°) largely deviate from the value of 180°. Consequently, it seems that the superexchange interactions between second-nearest Eu neighbors are very weak and the value of J_2 is negligible ($J_2/k \simeq 0$ K).

When $Z_1J_1/k<0$ K and $Z_2J_2/k \simeq 0$ K are substituted in Eqs. (1-1) and (1-2), we obtain the result which the θ_C is negative and the T_N is positive. Therefore, it is reasonable that EuB_2O_4 is an antiferromagnet with $T_N \simeq 3$ K and $\theta_C = -5$ K.

The magnetic property of $Eu_2B_2O_5$ was understood based on the structure of $Sr_2B_2O_5$, since $Eu_2B_2O_5$ is isostructural with $Sr_2B_2O_5$. The detailed structure analysis of $Sr_2B_2O_5$ has been performed by Bartl et al.[29] Each Sr^{2+} ion is surrounded by 6 or 7 oxygens, and has 8 nearest Sr neighbors at the mean distance 4.04 Å, which form a dodecahedron, and 2 second-nearest Sr neighbors at 5.35 Å. Each nearest Sr neighbor pair coordinates one, two, or three oxygens with Sr-O-Sr angles of 70 to 100°.

For $Eu_2B_2O_5$, since the mean distance between nearest neighboring Eu^{2+} ions (4.04 Å for $Sr_2B_2O_5$) is roughly equivalent to that in EuB_2O_4 or $EuTiO_3$, the positive Eu^{2+}-Eu^{2+} interaction is weak, too. However, the negative 90°Eu^{2+}-O^{2-}-Eu^{2+} interaction does not seem to dominate the J_1 as in EuB_2O_4 or $EuTiO_3$, since the coordination numbers of the nearest neighboring oxygens about the exchange pairs of nearest Eu neighbors are less than that in EuB_2O_4 or $EuTiO_3$. Consequently, the value of J_1 seems to be very small and negligible ($J_1/k \simeq 0$ K). The value of J_2 also is negligible ($J_2/k \simeq 0$ K), since no oxygen is coordinated between second-nearest Eu neighbors such as the 180°Eu^{2+}-O^{2-}-Eu^{2+} although the Eu-Eu distance (5.35 Å) is as short as that in $EuTiO_3$ or Eu_2TiO_4.

Therefore, it seems to be reasonable that $Eu_2B_2O_5$ is paramagnetic in spite of the fact that the EuO content in $Eu_2B_2O_5$ is more than that in EuB_2O_4. It is concluded that the difference between the magnetic properties of EuB_2O_4 and $Eu_2B_2O_5$ is due to that between the corresponding anion coordinations around the exchange pairs.

It is to note that the single crystals of EuB_2O_4 are expected to be magnetic anisotropy, since the nearest Eu neighbors are located in the (010) or (020) plane.

C. Luminescent properties. Some of europium(II) borates and Eu^{2+}-activated strontium borates were found to give the $4f^7$-$4f^6 5d$ band emissions. The luminescences of $(Sr_{1-x}Eu_x)_3B_2O_6$ and $(Sr_{1-x}Eu_x)_2B_2O_5$ were very weak or not observed (Fig. 9).

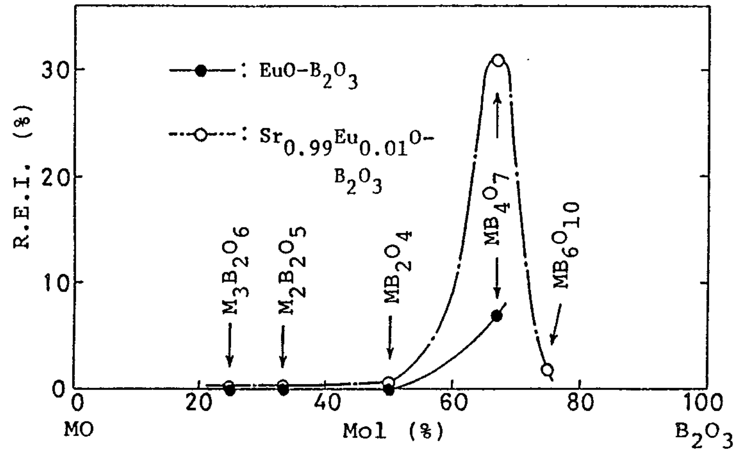

Figure 9. Relative emission intensity under 254 nm excitation at 300 K for a series of europium(II) borates and Eu^{2+} (1 at%)-activated strontium borates.

Compounds, $Sr_{1-x}Eu_xB_2O_4$ and $Sr_{1-x}Eu_xB_4O_7$, have the emission spectra peaking at about 370 nm, respectively. They are closely similar to each other (Figs. 10 and 11), but their excitation spectra vary with

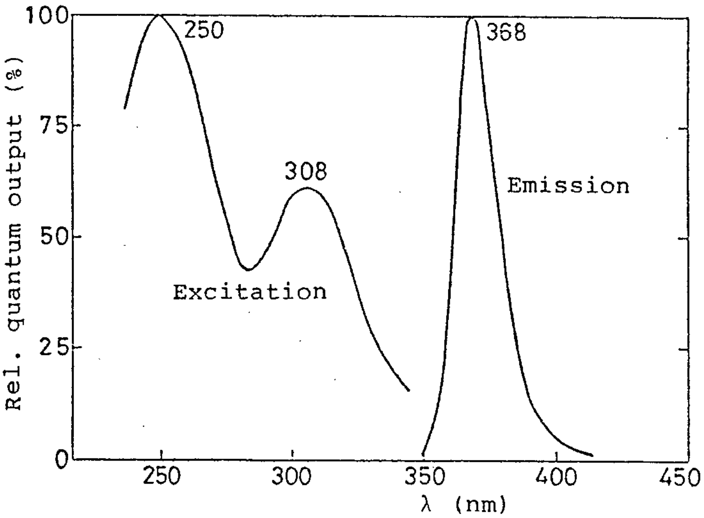

Figure 10. Relative emission and excitation spectra at 77 K of $Sr_{0.99}Eu_{0.01}B_2O_4$.

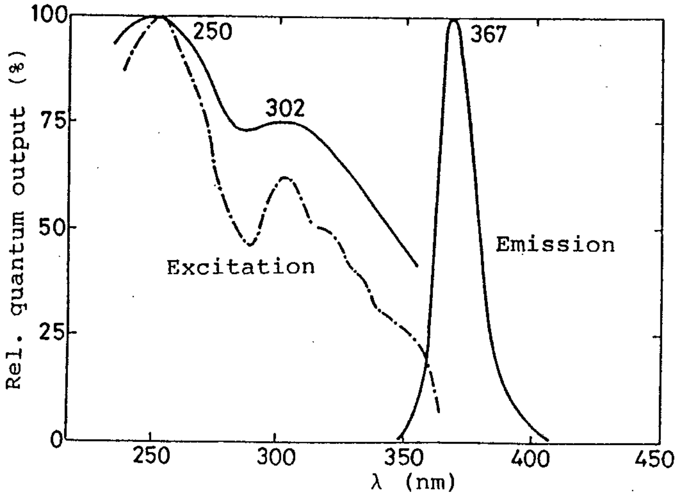

Figure 11. Relative emission and excitation spectra at 77 K of $Sr_{0.99}Eu_{0.01}B_4O_7$. The dashed-line represents the relative excitation spectra measured with the excitation and emission slits setting at 5 and 0.5 nm, respectively.

value of x (Fig. 12). On two borates, $Sr_{0.99}Eu_{0.01}B_2O_4$ and $Sr_{0.99}$-$Eu_{0.01}B_4O_7$, the similar excitation spectra are observed peaking at 250 and 308 nm and at 250 and 302 nm, respectively, whereas EuB_4O_7 as x=

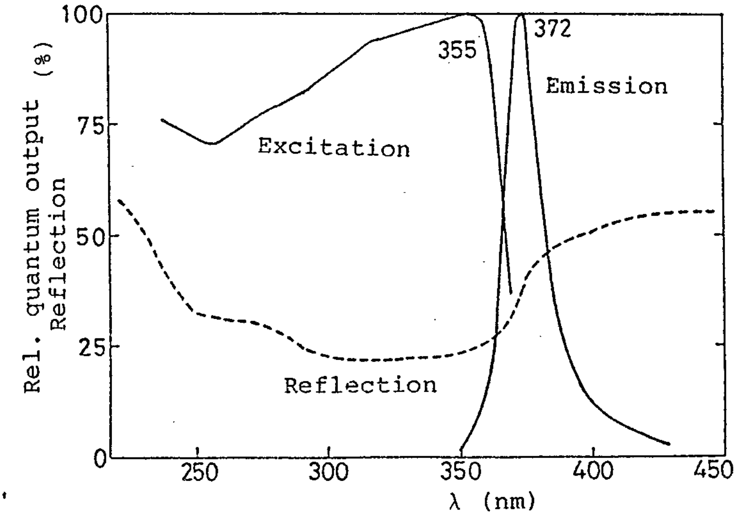

Figure 12. Relative emission and excitation spectra at 77 K and diffuse reflection spectrum at 300 K of EuB_4O_7.

1.00 gives a broad band peaking at 355 nm. The excitation spectrum of EuB_2O_4 was not observed, apparently since its emission spectrum was very weak.

The M (M=Sr and Eu) atoms in MB_2O_4 and MB_4O_7 are surrounded by 8 and 9 O atoms to form MO_8 and MO_9 polyhedra, respectively. The two polyhedra seem to give approximately the same symmetry of the crystal field as a regular octahedral field is caused, although they are considerably distorted (see Figs. 3 and 4). Therefore, it is concluded that the excitation spectra peaking at two positions of $Sr_{0.99}Eu_{0.01}$-B_2O_4 and $Sr_{0.99}Eu_{0.01}B_4O_7$ are due to energy splitting of the 5d level of Eu^{2+} ions into two levels, t_{2g} and e_g. The two bands of their spectra are relatively broad because of the low symmetry around Eu^{2+} ions. Particularly, the excitation bands of $Sr_{0.99}Eu_{0.01}B_4O_7$ are seen to be considerably broadened and split into several fine bands when its excitation spectrum is measured with the excitation and emission slits setting at 5 and 0.5 nm (see Fig. 11).

The emission spectrum of $Sr_{1-x}Eu_xB_6O_{10}$ peaks at about 388 and 432 nm, and its excitation spectra of 388 and 432 nm emission bands consist of three and two bands (Fig. 13). The emission band at 432 nm corresponds to that of vitreous SrB_6O_{10}:Eu^{2+}, and accordingly the band at

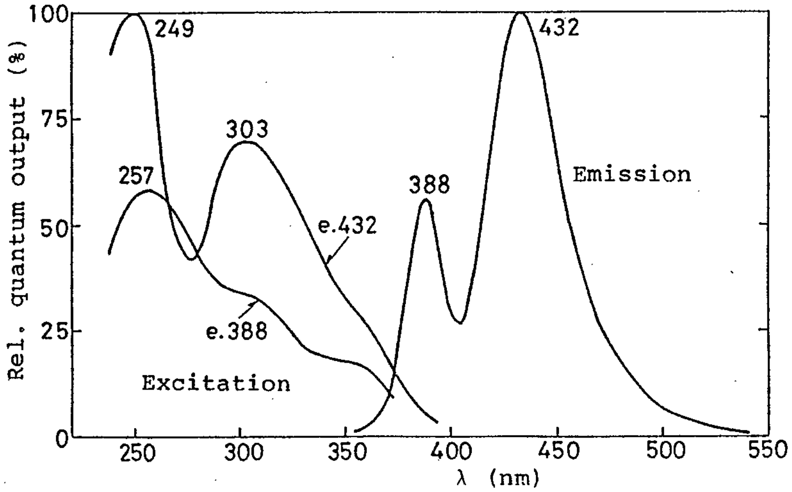

Figure 13. Relative emission and excitation spectra at 77 K of $Sr_{0.99}Eu_{0.01}B_6O_{10}$.

388 nm is probably attributed to the Eu^{2+} ion in the crystalline SrB_6O_{10} matrix. The fact that the excitation spectrum of 388 nm emission band consists of three bands suggests that the 5d level of Eu^{2+} ions splits into three and consequently $Sr_{0.99}Eu_{0.01}B_6O_{10}$ forms the crystal field considerably differing from that of $Sr_{0.99}Eu_{0.01}B_2O_4$ and $Sr_{0.99}Eu_{0.01}B_4O_7$.

From Fig. 9, it is to be noted that the relative emission intensity of $Sr_{1-x}Eu_xB_4O_7$ is much higher than that of the other compounds. In order to discuss the concentration quenching phenomenon of $Sr_{1-x}Eu_xB_4O_7$, the energy transfer from Eu^{2+} to Eu^{2+} ions have been considered on the basis of the Dexter theory. Since the 4f-5d transition of Eu^{2+} ions is an allowed one, the transfer will mainly take place via a dipole-dipole interaction.31) The probability (P) of energy transfer between neighboring Eu^{2+} ions by this interaction has been expressed as32)

$$P_{Eu^{2+}-Eu^{2+}} = 3 \times 10^{12} \frac{P_A}{R^6 \tau_{Eu}} \frac{1}{E^4} \int f_{Eu}(E)\, F_{Eu}(E)\, dE\,, \tag{1-3}$$

where P_A is the oscillator strength of the 4f-5d transition in Eu^{2+} ions, R the distances between the neighboring Eu^{2+} ions (in Å), τ_{Eu} the decay time of the luminescence (in s), E the energy involved in the transfer (in eV) and $\int f_{Eu}(E)F_{Eu}(E)dE$ the overlap between the normalized shape of the emission and the absorption (reflection) bands of Eu^{2+} ions (in eV^{-1}).

The critical distance (R_c) defined by Blasse[32)] is the distance between two luminescent centers, S (sensitizer) and A (activator), at which the probability of transfer from S to A is equal to the probability of radiative emission of S. In Eq. (1-3), this means that $P_{Eu-Eu}\tau_{Eu}=1$, and hence R_c is given as

$$R_c^6 = 3 \times 10^{12} \frac{P_A}{E^4} \int f_{Eu}(E)\, F_{Eu}(E)\, dE\,. \qquad (1\text{-}4)$$

If $P_A=0.01$ (the usual value for 4f-5d transitions) and E=3.5 eV are substituted in Eq. (1-4) and the energy overlap at about 0.3 eV^{-1} is estimated from Fig. 12, $R_c=20$ Å is found for EuB_4O_7.

The mean distances between the neighboring Eu^{2+} ions of EuB_4O_7 are 4.338 Å for 4 nearest Eu neighbors and 6.171 Å for 12 second-nearest Eu neighbors, and accordingly many Eu^{2+} ions are positioned around an Eu^{2+} ion at the distance within 20 Å. Therefore, it is concluded that the energy transfer in this effectively occurs between the neighboring the energy transfer in this borate effectively occurs between the neighboring Eu^{2+} ions based on the above-calculated value. In practice, hence the calculated result seems to be in conflict with the experimental one. This will be discussed later.

The Eu^{2+} concetration dependence of the relative emission intensity in $Sr_{1-x}Eu_xB_4O_7$ is summarized in Fig. 14. The optimum concentration is seen to be about 5 at%, at which its relative emission intensity is about 40 % under 254 nm excitation at 300 K.

The distance R_c can also be estimated from geometrical considerations[32)] with help of the formula

$$R_c \simeq 2(3V/4\pi x_c N)^{1/3}\,, \qquad (1\text{-}5)$$

where V is the volume of the unit cell (in $Å^3$), x_c the activator atom fraction (the optimum concentration) at which the quenching occurs, the so-called critical concentration and N the number of sites per unit

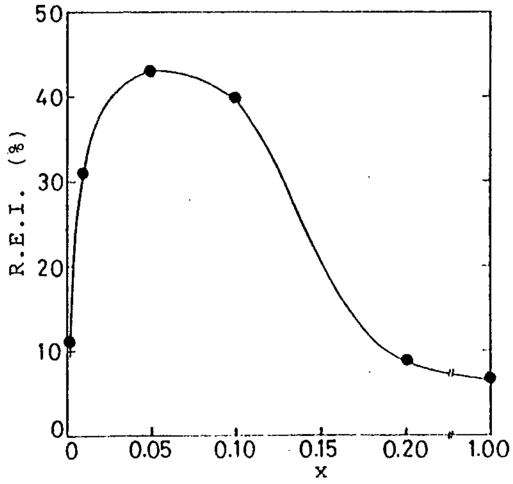

Figure 14. Relative emission intensity vs. Eu^{2+} content (x) for $Sr_{1-x}Eu_xB_4O_7$. Excitation at 254 nm and 300 K.

which M atoms can occupy. Accordingly x_c is given as

$$x_c \simeq 6V/\pi N R_c^3 . \qquad (1\text{-}6)$$

If we substitute in Eq. (1-6) V=4.4263x10.7074x4.2338 $\mathring{A}^3$ (cell constants of SrB_4O_7[30)]), N=2 [M atoms occupy the 4(a) site], and R_c=20 Å [the value obtained from Eq. (1-4) for EuB_4O_7], we find x_c=0.02. Although this calculated value seems to be in good agreement with the value obtained from experimental data (x=0.05), there is still difference. This will also be discussed later.

The structure of MB_4O_7 consists of the three-dimensional network of BO_4 tetrahedra and neighboring M^{2+} ions are completely isolated from one another by that network in comparison with the cases of the other borates. For $M_3B_2O_6$ and $M_2B_2O_5$ consisting of BO_3^{3-} and $B_2O_5^{4-}$ ions, such isolating effect of borate units to M^{2+} ions is an incomplete one, and although for MB_2O_4 all sites of M^{2+} ions are located in (010) and (020) planes by $(BO_2)_\infty$ chains extending parallel to the c axis, no borate unit is positioned between the neighboring M^{2+} ions in those planes. This suggests that the concentration quenching effect of $Sr_{1-x}Eu_xB_4O_7$ can be expected to be lowered by a so-called " shield effect " of the BO_4 network for the Eu^{2+}-Eu^{2+} interactions whereas for the other compounds above-described such effect is small owing to the incompleteness of isolating Eu^{2+} ions form neighboring Eu^{2+} ions by the borate units. Therefore, it is reasonable that $Sr_{1-x}Eu_xB_4O_7$ gives very strong emission in comparison with that of the other compounds and the optimum concentration of $Sr_{1-x}Eu_xB_4O_7$ (x=0.05) deviates from the calculated one (x_c=0.02).

The fact that $Sr_{1-x}Eu_xB_6O_{10}$ gives the relatively weak emission is probably due to following causes: (a) for $Sr_{1-x}Eu_xB_6O_{10}$ prepared from $SrO \cdot 3B_2O_3 \cdot 5H_2O:Eu^{3+}$, it contains more or less a glassy phase from which the luminescence is weak, and hence the emission of $Sr_{1-x}Eu_xB_6O_{10}$ is weak. (b) If the $(B_3O_5)_\infty$ network of MB_6O_{10} is unable to isolate Eu^{2+} ions from the neighboring Eu^{2+} ions completely, $Sr_{1-x}Eu_xB_6O_{10}$ should give the weak emission.

D. Thermal properties. The Eu^{2+} ions in solid phases of inorganic compounds are easily oxidized to Eu^{3+} ions by heating in an oxidizing atmosphere at 300-500°C. The thermal analytical data for a series of europium(II) borates are presented in Fig. 15 and Table XII. The oxidation temperature is about 400°C for $Eu_3B_2O_6$, 410°C for $Eu_2B_2O_5$, 480°C for EuB_2O_4, and 760°C for EuB_4O_7. The proportions of weight gains by oxidation are in good agreement with the corresponding theoretical values. It is noticeable that the oxidation temperature of EuB_4O_7 is considerably higher than those of other europium(II) borates. This can

Table XII. Thermal data for a series of europium(II) borates

Borate	M.P. (°C)	Oxidation temperature (°C)	Weight gain (%)	
			Found	Calcd.
$Eu_3B_2O_6$	—	400	4.14	4.18
$Eu_2B_2O_5$	≃1000	410	3.88	3.95
EuB_2O_4	≃1000	480	3.33	3.37
EuB_4O_7	985	760	2.51	2.60

be considered as being attributable to their structural framework. From the IR spectral and X-ray analyses, $Eu_3B_2O_6$ and $Eu_2B_2O_5$ contain BO_3^{3-} and $B_2O_5^{4-}$ ions, and EuB_2O_4 consists of $(BO_2)_\infty$ chains. Their Eu^{2+} ions are closely packed together with the borate ions or along the direction of borate chains. The Eu^{2+} ions in EuB_4O_7 are completely surrounded by BO_4 units of the $(B_4O_7)_\infty$ network, and are therefore hardly expected to be attacked by oxygen.

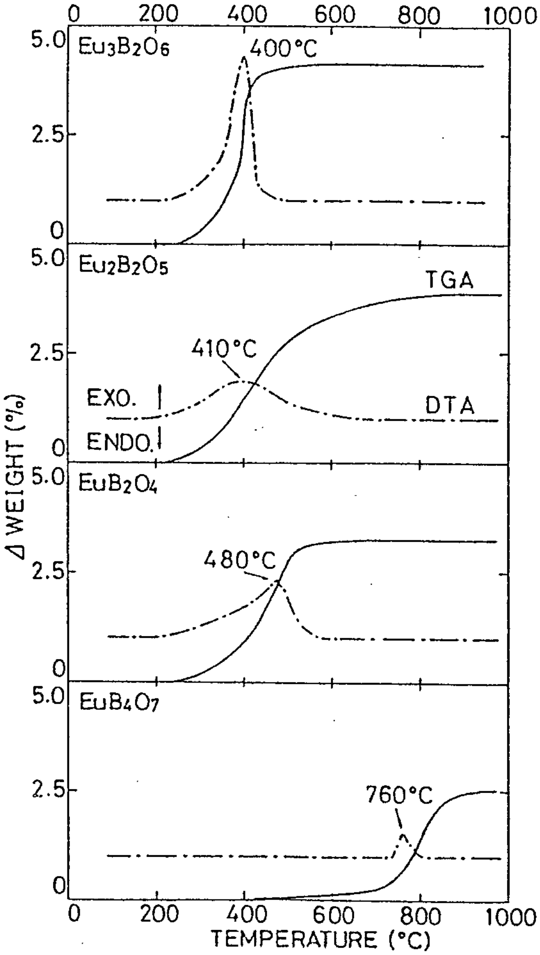

Figure 15. TGA and DTA curves for a series of europium(II) borates.

1-4. Summary

Several new europium(II) borates, EuB_4O_7, EuB_2O_4, and $Eu_2B_2O_5$ were synthesized in the binary system $EuO-B_2O_3$, and the single crystals of these borates and $Eu_3B_2O_6$ were grown by applying the Bridgeman and flux methods. These crystals belong to the following symmetries: orthorhombic ($Pnm2_1$), EuB_4O_7; orthorhombic (Pnca), EuB_2O_4; monoclinic ($P2_1/a$), $Eu_2B_2O_5$; trigonal ($R\bar{3}c$), $Eu_3B_2O_6$. From the X-ray analyses (R=0.023 for 510 observed reflections of EuB_4O_7, R=0.029 for 334 observed reflections of EuB_2O_4, and R=0.082 for 259 observed reflections of $Eu_3B_2O_6$) and IR spectral analyses, their crystal lattices are constructed of the following borate anions: a three-dimensional $(B_4O_7)_\infty$ network of BO_4 tetrahedra, EuB_4O_7; $(BO_2)_\infty$ chains of BO_3 triangles, EuB_2O_4; $B_2O_5^{4-}$ ions, $Eu_2B_2O_5$; BO_3^{3-} ions, $Eu_3B_2O_6$.

The magnetic susceptibilities of europium(II) borates were measured over the temperature range of 2-300 K. Two borates, EuB_4O_7 and $Eu_2B_2O_5$, are paramagnetic in the measured temperatures while EuB_2O_4 is an antiferromagnet with $T_N \simeq 3$ K. The magnetic properties were understood by considering the relationship between their structures and the magnetic interactions.

The luminescent properties were studied on the europium(II) borates and Eu^{2+}-activated strontium borates. It was found that EuB_4O_7 and $SrB_4O_7:Eu^{2+}$ consisting of $(B_4O_7)_\infty$ network give remarkable stronger emissions than the other borates of BO_3^{3-} ions, $B_2O_5^{4-}$ ions, and $(BO_2)_\infty$ chains. These emissions, which are colored with violet-blue for $SrB_2O_4:Eu^{2+}$ and blue for $SrB_6O_{10}:Eu^{2+}$. For $Sr_3B_2O_6:Eu^{2+}$ and $Sr_2B_2O_5:Eu^{2+}$, no luminescence was observed. These experimental results were interpreted from their crytal structures and with help of the Dexter theory.

It was found from the thermal analyses that the oxidation temperature of EuB_4O_7 is considerably higher than those of the other borates. This could be considered as being attributable to their structural frameworks in a same manner as the luminescent properties.

2. SYNTHESIS AND PROPERTIES OF HALOBORATES IN THE TERNARY SYSTEM $EuO-EuX_2$(X=Cl and Br)-B_2O_3

2-1. Introduction

Most of Eu^{2+}-containing halides give the blue emissions with high quantum efficiency and, at low temperature, the $4f^7$-$4f^7$ line spectra are observed on some of them.11) Barium halides with high X-ray absorptivities have been brought into use as phosphors for X-ray intensifying screens.16) However, the practical use should be considerably limited because these halides are strongly deliquescent.

In a ternary system $MO-MX_2-B_2O_3$ (M=Ca, Sr, and Ba), haloborates as being stable even in a moist atmosphere have been prepared: $M_2B_5O_9X$ type compounds have been obtained in the attempts to prepare the boracite ($Mg_3B_7O_{13}Cl$) analogues.33) No boracite type compound has been synthesized in this system. Hanic and co-workers34) have prepared a new chloroborate, Ca_2BO_3Cl, as an intermediate phase in a system $Ca_3B_2O_6$-$CaCl_2$.

The present chapter deals with syntheses of deliquescence-resistant haloborates in a ternary system $EuO-EuX_2$(X=Cl and Br)-B_2O_3. The crystal structures, magnetism, and luminescence of resulting materials are described. The emission intensities of samples have been interpreted in terms of the crystal structures and magnetism.

2-2. Experimental

A. Sample preparation. The europium(II) haloborates are obtained from some raw materials, $Eu_3B_2O_6$ or EuB_2O_4, EuX_2, and B_2O_3. The preparation methods of $Eu_3B_2O_6$ and EuB_2O_4 have been described in ref. 20 and the preceding chapter, and EuX_2 can be easily prepared by heating $EuX_3 \cdot nH_2O$ together with a large excess of NH_4X at 650-700°C for several hours in a reducing atmosphere. When the appropriate amounts of $Eu_3B_2O_6$ or EuB_2O_4, EuX_2, and B_2O_3 were fully mixed, pelletized, and heated at 900 or 1050°C for 2 h, Eu_2BO_3X or $Eu_2B_5O_9X$ was formed. The single crystals of Eu_2BO_3X and $Eu_2B_5O_9X$ were prepared as follows: the appropriate amounts of $Eu_3B_2O_6$ or EuB_2O_4 and B_2O_3 and a large excess of EuX_2 were mixed. The mixtures were heated on a molybdenum boat above the congruent melting point of Eu_2BO_3X or $Eu_2B_5O_9X$ (about 1050 or 1100 °C) for 1 or 2 h in an inert gas, e.g., He, and then the molten samples were allowed to cool at a rate of 3-5°C/h to 800 or 950°C. The unreactive $EuBr_2$ served as a flux and was removed from the resulting materials by washing with water or methanol. The black hexagonal prisms (∿2 mm long) were obtained for Eu_2BO_3X while $Eu_2B_5O_9Cl$ and $Eu_2B_5O_9Br$ gave the prismatic and needlelike single crystals colored with light yellow (∿4 mm long).

The Eu^{2+}-activated strontium haloborate, $Sr_2BO_3X{:}Eu^{2+}$ or $Sr_2B_5O_9X{:}Eu^{2+}$, was prepared by heating the stoichiometric mixture of SrX_2, H_3BO_3, $SrCO_3{:}Eu^{3+}$, coprecipitated from a dilute HCl solution of $Sr(NO_3)_2$ at 950°C for 2 h in a H_2 stream. The bromide, $SrBr_2{:}Eu^{2+}$, was formed when the precipitate $SrBr_2{:}Eu^{3+}$ from an aqueous solution was heated at 650°C for 2 h in a H_2 stream. The resulting materials were checked by the powder X-ray analysis.

B. Magnetic susceptibility and optical measurements. The magnetic susceptibilities or magnetizations and ultraviolet luminescent spectra of powder samples were measured with the same apparatuses and techniques as described in the preceding chapter.

C. X-ray measurements. Preliminary Weissenberg photographs showed that the crystals of Eu_2BO_3X and $Eu_2B_5O_9X$ belong to the hexagonal system of space group $P6_3mc$, $P\bar{6}2c$, or $P6_3/mmc$ (systematic absence: $l=2n+1$ for hhl reflections) and the orthorhombic (pseudotetragonal) system of space group Pnn2 or Pnnm (systematic absences: $k+l=2n+1$ for $0kl$ reflections and $h+l=2n+1$ for $h0l$ reflections). The accurate cell parameters (Table I) were determined by a least-squares treatments of the X-ray powder patterns (Cu $K\alpha_1$) calibrated with high purity silicon as an internal standard. The intensity data were measured on a Rigaku automated four-circle diffractometer according to the methods described elsewhere. All possible reflections were collected up to $2\theta=60$ or 70°. The numbers of observed reflections ($F_o>3\sigma F_o$) were 397 for Eu_2BO_3Cl,

Table I. Crystal data and X-ray measurements for europium(II) haloborates

	Eu_2BO_3Cl	Eu_2BO_3Br	$Eu_2B_5O_9Cl$	$Eu_2B_5O_9Br$
F.W.	398.18	442.64	537.43	581.88
Symmetry	Hexagonal		Orthorhombic	
S.G.	$P6_3mc$		Pnn2	
a (Å)	10.585(3)	10.598(1)	11.364(3)	11.503(3)
b (Å)			11.301(3)	11.382(3)
c (Å)	6.804(2)	6.845(1)	6.503(2)	6.484(2)
V ($Å^3$)	660.3(4)	665.8(2)	835.2(5)	848.9(4)
Dm (g/cm^3)	5.95	6.55	4.30	4.53
Dx (g/cm^3)	6.01	6.63	4.28	4.55
Z	6		4	
λ (Å)	0.71069			
μ(Mo Kα) (mm^{-1})	28.78	36.88	15.28	19.26
F(000)	1032	1140	960	1032
Cryst size (mm^3)	0.15 (ϕ) ×0.25	0.15 (ϕ) ×0.12	0.14×0.08 ×0.17	0.10×0.10 ×0.20

566 for Eu_2BO_3Br, 1967 for $Eu_2B_5O_9Cl$, and 1979 for $Eu_2B_5O_9Br$, respectively. The usual Lorentz and polarization corrections were applied, but the absorption and anomalous dispersion effects for heavy atoms were not considered.

D. Structure determinations and refinements. The structure of europium(II) haloborate, $Eu_2B_5O_9X$, was solved by the conventional heavy atom method and was refined by the method of block-diagonal least-squares (HBLS-V program$^{22)}$) in a similar manner as those of europium(II) borates (see the preceding chapter). From three-dimensional Patterson functions, the space group of $Eu_2B_5O_9X$ was found to be the noncentrosymmetric Pnn2 and the coordinates of Eu and X atoms were determined. All major peaks on the Patterson maps could be explained by locating the Eu atoms at the general positions [4(c) site] and X atoms at the special positions [2(a) and 2(b) sites]: Eu(1) at 0.25, 0.05, 0.00; Eu(2) at 0.03, 0.25, 0.66; X(1) at 0.00, 0.00, 0.88; X(2) at 0.00, 0.50, 0.66. The structure factors based on these coordinates, with the assumption of an isotropic thermal factor of 0.5 $\mathring{A}^2$ for each atom, gave R=0.40, which reduced to 0.13 after three cycles of refinements. The remaining atoms, O and B, were located on the successive Fourier maps. Three cycles of isotropic refinements gave a conventional R value of 0.060. Further refinements with anisotropic thermal factors for heavy atoms reduced the R and R_w values to 0.054 and 0.068 for $Eu_2B_5O_9Cl$ and 0.047 and 0.053 for $Eu_2B_5O_9Br$, respectively. The weighting schemes of $w=(F_{max}/F_o)^2$ for $F_o>F_{max}$ and w=1.0 for $F_o \leq F_{max}$ ($Eu_2B_5O_9Cl$, F_{max}=20.0; $Eu_2B_5O_9Br$, F_{max}=40.0) were employed. The atomic scattering factors were taken from the International Tables for X-ray Crystallography.[24)] The final positional and thermal parameters of $Eu_2B_5O_9Cl$ and $Eu_2B_5O_9Br$ are listed in Tables II and III.

For the haloborate, Eu_2BO_3X, the space group was found to be $P6_3mc$ from the three-dimensional Patterson maps calculated on the basis of the intensity data. The structure determinations are in progress.

2-3. Results and discussion

A. Crystal structure of $Eu_2B_5O_9X$. Since the final parameters of $Eu_2B_5O_9X$ are almost equal to each other, the two europium(II) haloborates are considered to be isostructural. The interatomic distances and angles along with their estimated standard deviations of $Eu_2B_5O_9Br$ are presented in Table IV. There are two types of B atoms: three of them [B(1), B(2), and B(3)] are tetrahedrally coordinated with mean B-O distances from 1.446 to 1.438 Å and two [B(4) and B(5)] are triangularly coordinated with mean B-O distances 1.367 and 1.361 Å. The mean O-B-O angles are about 109° for tetrahedra and 120° for triangles, respectively. Three tetrahedra and two triangles form a B_5O_{12} group (Fig. 1) by sharing O atoms are shared with other BO_4 tetrahedra and O(2), O(5), O(6), and O(8) atoms are shared with BO_4 tetrahedra and BO_3 triangles. These groups are linked together to form a three-

Table II. Final positional and thermal parameters for $Eu_2B_5O_9Cl$, with their estimated standard deviations in parentheses

Atom	x	y	z	U_{11} [a]	U_{22}	U_{33}	U_{12}	U_{13}	U_{23}
Eu(1)	0.2523(7)	0.0475(6)	0	79(2)	69(2)	60(2)	8(2)	-11(2)	-11(3)
Eu(2)	0.0255(6)	0.2403(6)	0.6624(12)	48(2)	96(2)	53(2)	-4(2)	-13(3)	3(3)

Atom	x	y	z	B (Å^2)	Atom	x	y	z	B (Å^2)
Cl(1)	0	0	0.862(6)	1.08(7)	O(7)	0.182(10)	0.269(10)	0.939(10)	0.21(11)
Cl(2)	0	1/2	0.613(6)	1.03(7)	O(8)	0.421(10)	0.207(10)	0.510(12)	0.53(12)
O(1)	0.244(10)	0.318(10)	0.594(10)	0.31(12)	O(9)	0.232(10)	0.114(10)	0.576(11)	0.46(12)
O(2)	0.211(10)	0.427(10)	0.191(11)	0.60(13)	B(1)	0.274(14)	0.325(13)	0.809(15)	0.25(16)
O(3)	0.279(10)	0.225(10)	0.255(10)	0.38(12)	B(2)	0.187(12)	0.299(12)	0.162(20)	0.29(14)
O(4)	0.077(11)	0.270(11)	0.263(11)	0.61(13)	B(3)	0.292(14)	0.217(13)	0.479(15)	0.31(16)
O(5)	0.286(11)	0.451(10)	0.853(12)	0.64(13)	B(4)	0.457(22)	0.231(21)	0.712(23)	1.40(27)
O(6)	0.384(12)	0.262(11)	0.856(12)	0.78(14)	B(5)	0.251(16)	0.497(15)	0.035(15)	0.57(19)

[a] The form of the anisotropic thermal parameter (×10^4) is $\exp[-2\pi^2(U_{11}h^2a^{*2} + U_{22}k^2b^{*2} + U_{33}l^2c^{*2} + 2U_{12}hka^*b^* + 2U_{13}hla^*c^* + 2U_{23}klb^*c^*)]$.

Table III. Final positional and thermal parameters for Eu$_2$B$_5$O$_9$Br, with their estimated standard deviations in parentheses

Atom	x	y	z	U_{11}[a]	U_{22}	U_{33}	U_{12}	U_{13}	U_{23}
Eu(1)	0.2547(6)	0.0501(6)	0	76(2)	77(2)	84(2)	12(2)	-12(2)	-10(2)
Eu(2)	0.0307(6)	0.2374(6)	0.6572(10)	62(2)	92(2)	77(2)	-4(2)	-16(2)	1(3)
Br(1)	0	0	0.8769(27)	95(7)	107(7)	244(10)	-19(6)	0	0
Br(2)	0	1/2	0.6370(32)	75(6)	111(7)	357(13)	2(5)	0	0

Atom	x	y	z	B $(\text{\AA}^2)$	Atom	x	y	z	B $(\text{\AA}^2)$
O(1)	0.246(9)	0.318(9)	0.581(9)	0.40(11)	O(8)	0.423(9)	0.212(9)	0.500(11)	0.66(11)
O(2)	0.209(9)	0.427(9)	0.182(10)	0.59(12)	O(9)	0.239(9)	0.115(9)	0.571(10)	0.62(12)
O(3)	0.279(9)	0.227(9)	0.248(10)	0.59(12)	B(1)	0.275(12)	0.326(12)	0.805(13)	0.17(13)
O(4)	0.078(9)	0.267(9)	0.254(10)	0.69(12)	B(2)	0.187(12)	0.299(12)	0.167(17)	0.54(14)
O(5)	0.283(10)	0.454(9)	0.844(11)	0.76(12)	B(3)	0.295(12)	0.218(12)	0.471(13)	0.39(15)
O(6)	0.388(10)	0.266(10)	0.847(10)	0.76(12)	B(4)	0.462(14)	0.236(15)	0.699(14)	0.72(18)
O(7)	0.185(9)	0.271(8)	0.928(9)	0.35(10)	B(5)	0.248(12)	0.497(12)	0.031(12)	0.29(14)

[a] The form of the anisotropic thermal parameter (×10^4) is $\exp[-2\pi^2(U_{11}h^2a^{*2} + U_{22}k^2b^{*2} + U_{33}l^2c^{*2} + 2U_{12}hka^*b^* + 2U_{13}hla^*c^* + 2U_{23}klb^*c^*)]$.

Table IV. Interatomic distances (Å) and angles (°) in $Eu_2B_5O_9Br$, with their estimated standard deviations in parentheses

(a) Distances and Angles of the $(B_5O_9)_\infty$ Network

B(1)–Tetrahedron

B(1)–O(1)	1.489 (16)	O(1)–B(1)–O(5)	103.9 (9)
B(1)–O(5)	1.483 (16)	O(1)–B(1)–O(6)	110.2 (10)
B(1)–O(6)	1.497 (16)	O(1)–B(1)–O(7)	110.5 (10)
B(1)–O(7)	1.446 (15)	O(5)–B(1)–O(6)	111.3 (10)
average	1.479	O(5)–B(1)–O(7)	112.1 (10)
		O(6)–B(1)–O(7)	108.8 (10)
		average	109.5

B(2)–Tetrahedron

B(2)–O(2)	1.485 (20)	O(2)–B(2)–O(3)	114.6 (12)
B(2)–O(3)	1.443 (19)	O(2)–B(2)–O(4)	111.6 (12)
B(2)–O(4)	1.422 (20)	O(2)–B(2)–O(7)	105.2 (13)
B(2)–O(7)	1.582 (19)	O(3)–B(2)–O(4)	111.1 (13)
average	1.483	O(3)–B(2)–O(7)	104.5 (13)
		O(4)–B(2)–O(7)	108.9 (13)
		average	109.3

B(3)–Tetrahedron

B(3)–O(1)	1.454 (16)	O(1)–B(3)–O(3)	112.8 (10)
B(3)–O(3)	1.457 (16)	O(1)–B(3)–O(8)	111.4 (10)
B(3)–O(8)	1.476 (17)	O(1)–B(3)–O(9)	103.3 (10)
B(3)–O(9)	1.493 (17)	O(3)–B(3)–O(8)	104.8 (10)
average	1.470	O(3)–B(3)–O(9)	115.2 (10)
		O(8)–B(3)–O(9)	109.6 (10)
		average	109.5

B(4)–Triangle

B(4)–O(4)	1.382 (18)	O(4)–B(4)–O(6)	116.1 (13)
B(4)–O(6)	1.326 (18)	O(4)–B(4)–O(8)	123.1 (13)
B(4)–O(8)	1.392 (18)	O(6)–B(4)–O(8)	120.9 (13)
average	1.367	average	120.0

B(5)–Triangle

B(5)–O(2)	1.338 (16)	O(2)–B(5)–O(5)	122.4 (10)
B(5)–O(5)	1.368 (16)	O(2)–B(5)–O(9)	118.8 (10)
B(5)–O(9)	1.376 (16)	O(5)–B(5)–O(9)	119.0 (10)
average	1.361	average	120.1

(b) Eu–Eu Distances[a]

Nearest Neighbors

Eu(1)–Eu(2)	4.014 (1)	Eu(1)–Eu(2‴)	4.122 (1)
Eu(1)–Eu(2′)	5.142 (1)	average	4.432
Eu(1)–Eu(2″)	4.448 (1)		

Next-Nearest Neighbors

Eu(1)–Eu(1′)	5.750 (1)	Eu(1)–Eu(2)	5.415 (1)
	5.976 (1)	Eu(1)–Eu(2′)	6.296 (1)
Eu(2)–Eu(2′)	5.442 (1)		
	6.029 (1)		

(c) Eu–Br and Eu–O Distances

Eu(1) Polyhedron

Eu(1)–Br(1)	3.093 (3)	Eu(1)–O(3)	2.590 (10)
Eu(1)–Br(2)	3.009 (3)	Eu(1)–O(5)	2.522 (11)
average	3.051	Eu(1)–O(6)	3.061 (11)
Eu(1)–O(1)	2.692 (9)	Eu(1)–O(7)	2.682 (9)
Eu(1)–O(2)	2.526 (10)	Eu(1)–O(9)	2.884 (10)
		average	2.708

Eu(2) Polyhedron

Eu(2)–Br(1)	3.075 (3)	Eu(2)–O(4)	2.691 (10)
Eu(2)–Br(2)	3.012 (3)	Eu(2)–O(6)	2.598 (11)
average	3.044	Eu(2)–O(7)	2.528 (9)
Eu(2)–O(1)	2.683 (9)	Eu(2)–O(8)	2.613 (11)
Eu(2)–O(3)	2.986 (10)	Eu(2)–O(9)	2.832 (10)
		average	2.704

[a] Symmetry transformations: Eu(1′), $(\bar{x}, \bar{y}, z)$; Eu(2′), $(\bar{x}, \bar{y}, z)$; Eu(2″), $(1/2 - x, 1/2 + y, 1/2 + z)$; Eu(2‴), $(1/2 + x, 1/2 - y, 1/2 + z)$.

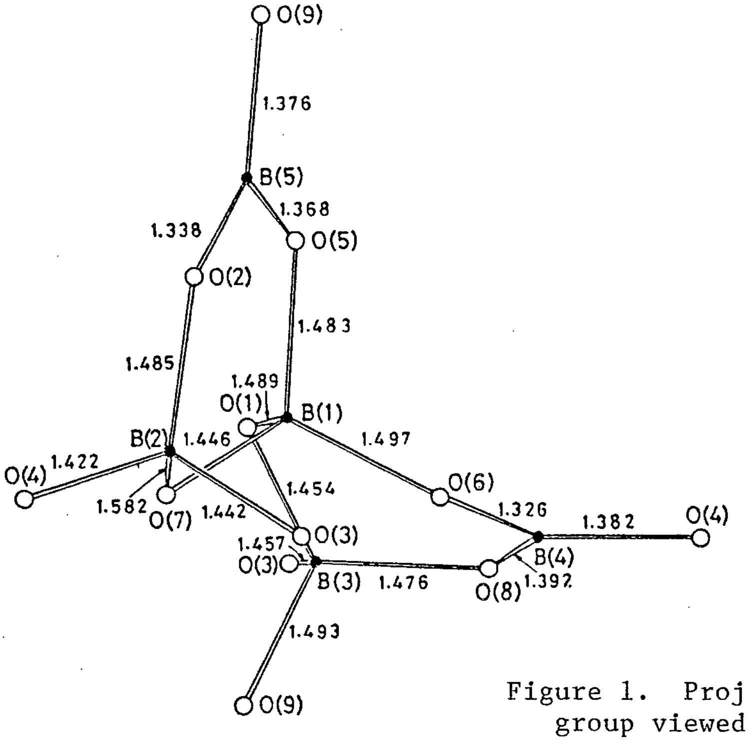

Figure 1. Projection of the B_5O_{12} group viewed along the c axis. The bond lengths in Å are given.

dimensional $(B_5O_9)_\infty$ network by sharing O(3), O(4), and O(9) atoms with one another. The projections of the $Eu_2B_5O_9Br$ structure viewed along the c and b axes are shown in Figs. 2 and 3, respectively. The structure consists of chains of corner-sharing BO_4 tetrahedra which extend along the c axis, and they are linked in the a- and b-axis directions by B(4) and B(5) atoms which occupy the centers of triangles formed by O atoms.

The Eu and Br atoms are located alternately with each other in tunnels of the $(B_5O_9)_\infty$ network, and each Eu atom is considerably isolated from neighboring Eu atoms by the borate units of the $(B_5O_9)_\infty$ network in the a- and b-axis directions and Br atoms in the c-axis direction. The anion environments around Eu(1) and Eu(2) atoms are shown in Fig. 4. The Eu atoms are surrounded by two Br atoms and seven O atoms to form a EuO_7Br_2 polyhedron with Eu-Br distances from 3.009 to 3.093 Å and Eu-O distances from 2.526 to 3.061 Å, respectively.

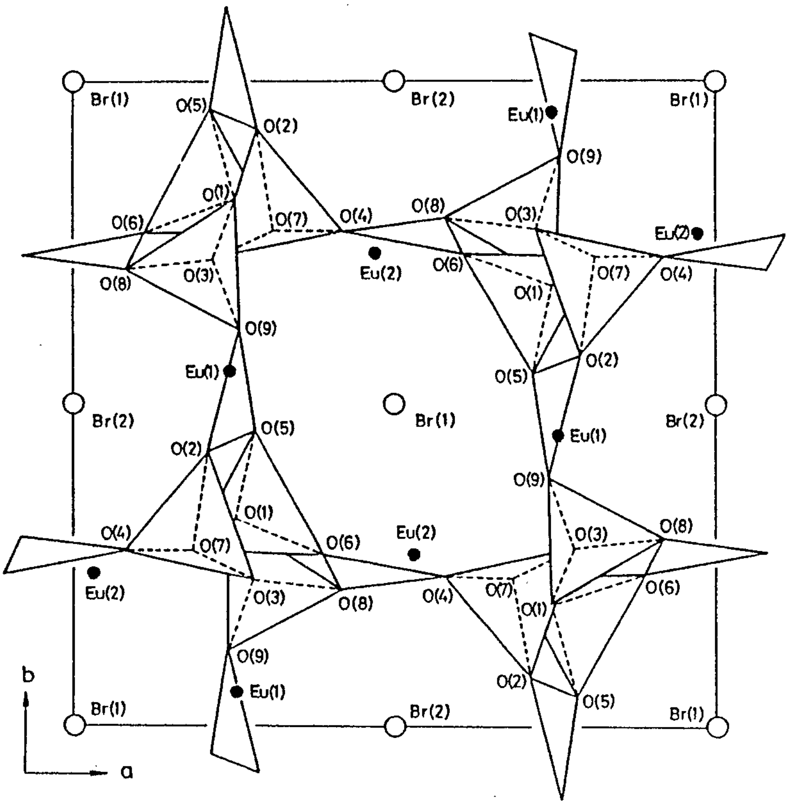

Figure 2. Projection of the $Eu_2B_5O_9Br$ structure viewed along the c axis.

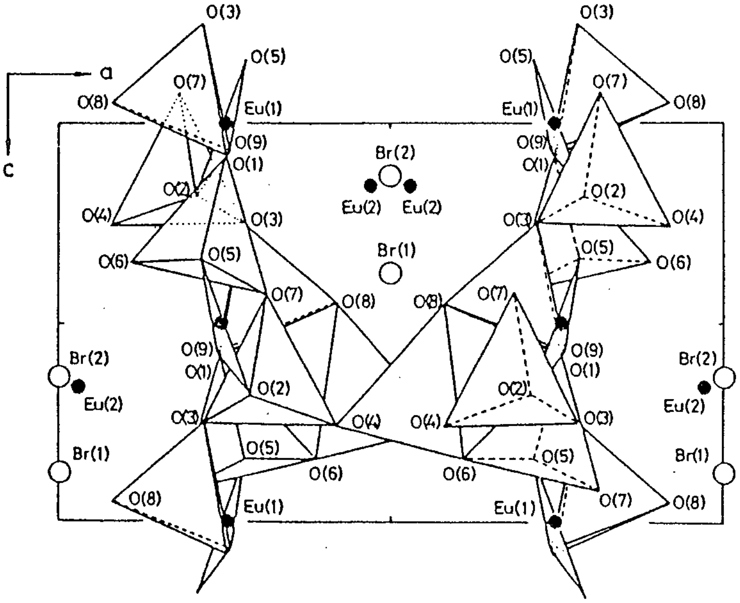

Figure 3. Projection of the $Eu_2B_5O_9Br$ structure viewed along the b axis.

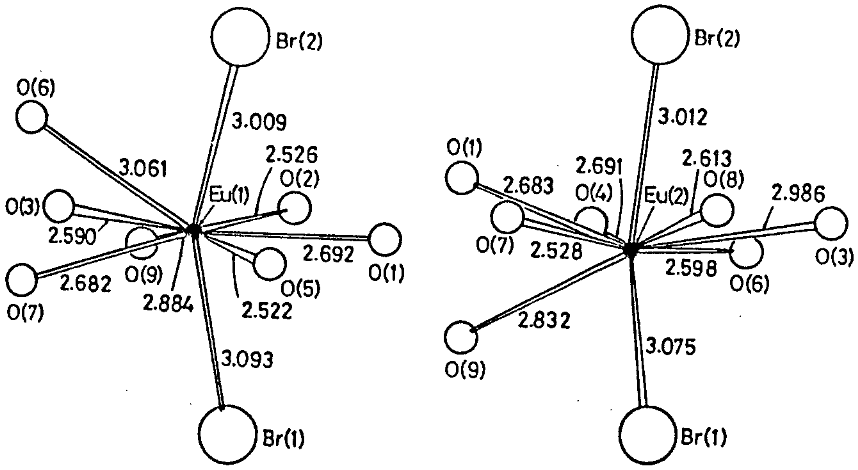

Figure 4. Anion environments around Eu(1) and Eu(2) atoms. Numerical values represent the nearest neighboring Eu-Br and Eu-O distances in Å.

B. Magnetic properties. The europium(II) haloborate, Eu_2BO_3X, was found to be a ferromagnet from the measurements of magnetizations at low temperatures, but another $Eu_2B_5O_9X$ was a paramagnet. The temperature and magnetic field dependences for the reciprocal susceptibility and magnetization of Eu_2BO_3Br are shown in Figs. 5 and 6. From Fig. 5, the reciprocal susceptibility can be seen to be proportional to the temperature above 10 K, but at the temperature below 10 K the reciprocal susceptibility deviates from the Curie Weiss law. The paramagnetic Curie temperature is about 5 K. For the magnetic field dependence of the magnetization at liq. He temperature (see Fig. 6), one can observed that the magnetization curve is asymptotic to the value at which the spins of the 4f electrons of Eu^{2+} ion are ferromagnetically arranged. It is, therefore, concluded that Eu_2BO_3Br is a ferromagnet with $4.2<T_C$ <5 K.

The magnetic and structural properties for some europium(II) compounds are summarized in Table V. The magnetisms of these compounds are interpreted by considering the exchange and superexchange interactions between the neighboring Eu^{2+} ions, which are sensitive to the Eu-Eu spacing. The Eu^{2+} ions in Eu_2BO_3X are located at two kinds of sites, Eu(1) and Eu(2). From the model of Eu_2BO_3Br structure with R=

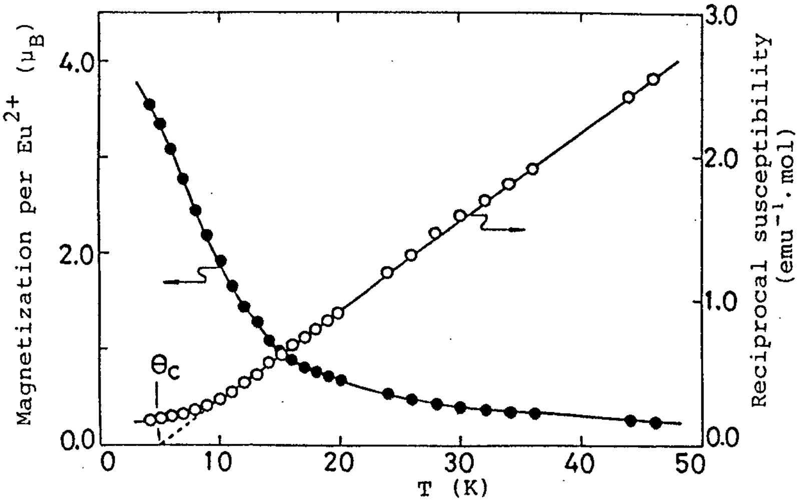

Figure 5. Temperature dependences for the magnetization and reciprocal susceptibility of Eu_2BO_3Br. The applied magnetic field is 3.5 KOe.

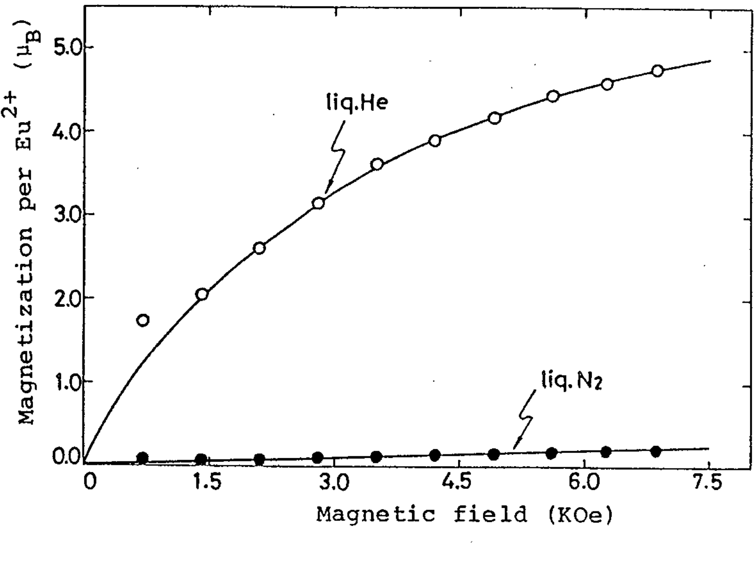

Figure 6. Magnetic field dependences for the magnetizations of Eu_2BO_3Br at liq. He (4.2 K) and liq. N_2 (77.4 K) temperatures.

0.10 for 566 non-equivalent reflections, mean distances between the neighboring Eu^{2+} ions are estimated to be 3.60 or 3.63 Å for the nearest neighbors and 5.27 or 5.14 Å for the second-nearest neighbors.

Table V. Magnetic and structural properties for some europium(II) compounds

Compt	Magnetism	$\mu_{eff}(\mu_B)$	T_C(K)	θ_C(K)	Atom	Mean Eu-Eu dist.(Å)[a] nn	nnn
$EuBr_2$[b]	Para.	7.87	—	0	Eu(1) Eu(2)	4.98(×9) 4.86(×8)	6.19(×5) 5.99(×4)
Eu_2BO_3Br	Ferro.	7.85	4.2∿5	5	Eu(1) Eu(2)	3.60(×6) 3.63(×4)	5.27(×6) 5.14(×4)
$Eu_2B_5O_9Br$	Para.	7.73	—	≃0	Eu(1) Eu(2)	4.432(4)	5.589(4) 5.796(4)

[a] nn and nnn represent the nearest and second-nearest Eu neighbors.

[b] See ref. 3.

These distances are comparable to that of $Eu_3B_2O_6$ with T_C=7.5 K (see the preceding chapter), and hence the magnetic interaction in Eu_2BO_3Br are effective for the ferromagnetic interactions at low temperatures. Since the superexchange interaction via X^- ion is less contributable than that interaction via O^{2-} ion, however, the T_C value of Eu_2BO_3X would be low compared with that of $Eu_3B_2O_6$.

C. Luminescent properties. The luminescent properties of some Eu^{2+}-containing compounds are summarized in Table VI. No luminescence was observed on Eu_2BO_3X. This must be attributable to the strong exchange and superexchange interactions between neighboring Eu^{2+} ions because Eu_2BO_3X is a ferromagnet with T_C≃5 K. The haloborate $Eu_2B_5O_9X$ (paramagnet) was found to be a blue emitting phosphor. The luminescent and diffuse reflection spectra are shown in Fig. 7. The haloborate, $Eu_2B_5O_9X$, emits the $4f^7$-$4f^6 5d$ band spectrum with half-width of 30 nm peaking at 430 or 435 nm, and these peak positions are near to that of EuX_2 as one of raw materials but considerably different from that of another raw material, EuB_2O_4. This suggests that the degrees for crystal field splitting and Stokes shifts of $4f^7$-$4f^6 5d$ levels in these compounds are different from one another. The Eu^{2+} ion in EuB_2O_4 is surrounded by eight oxygens to form a EuO_8 polyhedron with Eu-O distances 2.519-2.738 Å. The symmetry of the EuO_8 polyhedron differs

Table VI. Luminescent properties for some Eu^{2+}-containing compounds

Compound	λ_{max}(nm)[a]	$\lambda/2$(nm)[b]	R.E.I.(%)	
			254 nm excitation	optimum excitation
Eu_2BO_3Br	non-observable			
$Eu_2B_5O_9Br$	435	30	5	7 (350)
$(Sr_{0.93}Eu_{0.07})_2B_5O_9Br$	430	30	46	62 (350)
$EuBr_2$	422	27	12	21 (370)
$Sr_{0.99}Eu_{0.01}Br_2$	411	22	20	42 (370)
EuB_2O_4	370	20	negligible	
$Sr_{0.97}Eu_{0.03}B_2O_4$	367	20	2	2 (250)

[a] λ_{max}=position of the maximum of emission band. [b] $\lambda/2$=half-width of the emission band.

[c] R.E.I.=relative emission intensity at 300 K. The values in parentheses represent the wavelengths for optimum excitation.

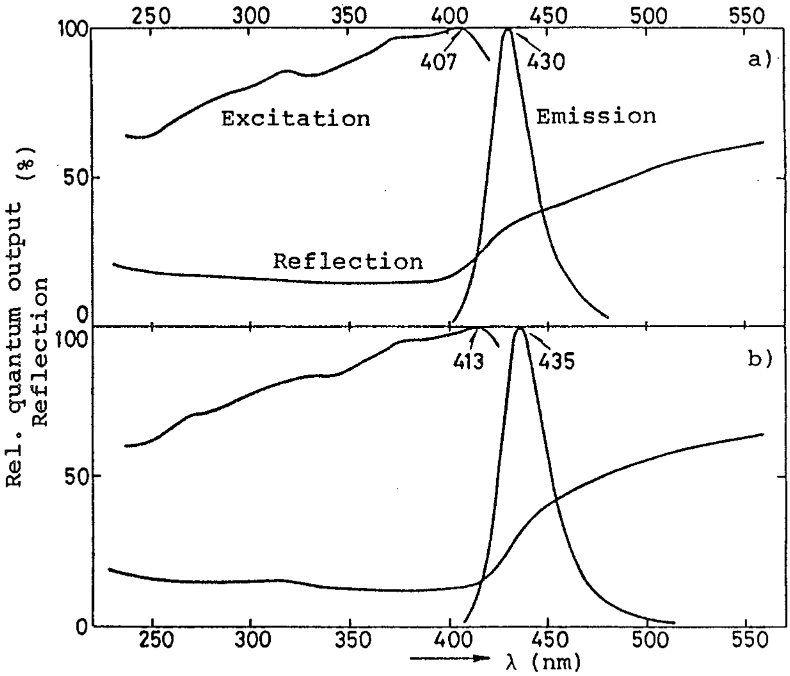

Figure 7. Relative emission and excitation spectra and diffuse reflection spectra at 300 K of a) $Eu_2B_5O_9Cl$ and b) $Eu_2B_5O_9Br$.

from that of the EuO_7X_2 polyhedron (see Fig. 4) in $Eu_2B_5O_9X$ because of the large X^- ions: the symmetry of the EuO_7X_2 polyhedron is low. This difference must reflect the degrees of crystal field splitting and Stokes shift.

It is seen from Table VI that $Sr_2B_5O_9Br:Eu^{2+}$ and $SrBr_2:Eu^{2+}$ give the blue emissions with high relative emission intensity (about 60 % under 350 nm excitation for the former compound and about 40 % under 370 nm excitation for the latter compound) and are efficient phosphors. Particularly, the relative emission intensities of $Eu_2B_5O_9Br$ and $EuBr_2$ are noticed to be considerably high compared with that of EuB_2O_4, although the concentration quenching effects in these materials are expected to be large.

In Fig. 8, the concentration quenching curve for $(Sr_{1-x}Eu_x)_2B_5O_9Br$ is shown together with those for $Sr_{1-x}Eu_xBr_2$ and $Sr_{1-x}Eu_xB_2O_4$. The curve of $(Sr_{1-x}Eu_x)_2B_5O_9Br$ or $Sr_{1-x}Eu_xB_2O_4$ has a maximum at about 7 or 3 at%. For $Sr_{1-x}Eu_xBr_2$, however, the relative emission intensity does not apparently depend on the value of x. The slope of this curve is much flatter than those of other curves.

One of the quenching effects on Eu^{2+}-activated phosphors is a non-

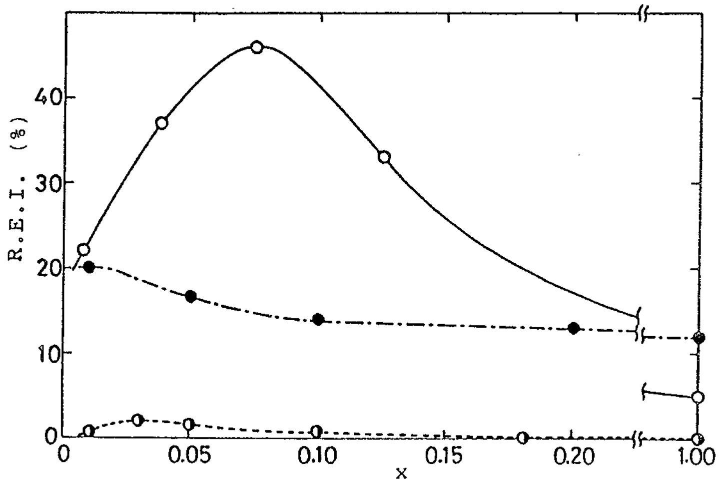

Figure 8. Relative emission intensity vs. Eu^{2+} content (x) for the emission bands under 254 nm excitation of $(Sr_{1-x}Eu_x)_2B_5O_9Br$ (○), $Sr_{1-x}Eu_xBr_2$ (●), and $Sr_{1-x}Eu_xB_2O_4$ (◐).

radiative process via Coulomb (dipole-dipole) interactions and exchange interactions between neighboring Eu^{2+} ions,[32] For the Eu^{2+}-activated phosphors, the Coulomb interactions are effective for one of the quenching effects, but the luminescent properties of high-concentration Eu^{2+}-containing samples, e.g., europium(II) compounds, should be understood with regard to both of the Coulomb and exchange interactions. The two compounds, $Eu_2B_5O_9Br$ and $EuBr_2$, are paramagnets while EuB_2O_4 is antiferromagnetic below about 3 K. The Eu atoms in $Eu_2B_5O_9Br$ have four nearest Eu neighbors with the mean Eu-Eu distance 4.432 Å and four second-nearest Eu neighbors with the mean Eu-Eu distance 5.589 Å for the Eu(1) atom or 5.796 Å for the Eu(2) atom. These Eu-Eu distances are very long compared with those of other europium(II) compounds with strong magnetic interactions,[3] and are insufficient for the magnetic interactions. The bromide $EuBr_2$ is isostructural with $SrBr_2$, and the Eu atoms have nine or eight nearest Eu neighbors with the mean Eu-Eu distance 4.98 or 4.86 Å and five or four second-nearest Eu neighbors with the mean Eu-Eu distance 6.19 or 5.99 Å for the Eu(1) or Eu(2) atom.[35] These distances also are entirely insufficient for the magnetic interactions. For EuB_2O_4, however, the 99.0 and 100.4°Eu^{2+}-O^{2-}-Eu^{2+} superexchange pairs are effective and antiferromagnetically contribute to the overall magnetism. The differences in the magnetisms of these compounds must reflect on their luminescent properties. For $Eu_2B_5O_9Br$ and $EuBr_2$, the quenching effect of exchange interactions is expected to be very small, but the quenching effect in EuB_2O_4 is not. This agrees with the fact that the former compounds give the emissions with very high intensity compared with that of the latter compound.

The observation that the concentration quenching curve of $Sr_{1-x}Eu_xBr_2$ has a flatter slope than those of $(Sr_{1-x}Eu_x)_2B_5O_9Br$ and $Sr_{1-x}Eu_xB_2O_4$ (see Fig. 8) suggests that the quenching effect of Coulomb interactions in bromides also is small and the Br^- ions may be excellent in the property of electrostatic shield. For $(Sr_{1-x}Eu_x)_2B_5O_9Br$ and $Sr_{1-x}Eu_xB_2O_4$, the concentration quenching curves have the maximum. This suggests that the quenching effect of Coulomb interactions is effective in these compounds. The Eu^{2+} ions in $Eu_2B_5O_9Br$ are located alternately with Br^- ions in tunnels of the $(B_5O_9)_\infty$ network, and each Eu^{2+} ion is isolated from the neighboring Eu^{2+} ions by the borate units of the $(B_5O_9)_\infty$ network in the a- and b-axis directions and Br^- ions in the c-axis direction. The energy transfers via Coulomb interactions are expected to take place mainly in the a- and b-axis directions, in which no Br^- ion is located. The fact that the emission of $Sr_{1-x}Eu_x$-B_2O_4 is very weak is due to the cluster formation of Eu^{2+} ions in the matrix as discussed later.

2-4. Summary

Two kinds of europium(II) haloborates, Eu_2BO_3X and $Eu_2B_5O_9X$, were obtained in the ternary system EuO-EuX_2(X=Cl and Br)-B_2O_3. Hexagonal prismatic and needlelike or prismatic single crystals were grown from the molten samples containing a large excess of EuX_2 as a flux.

The haloborate Eu_2BO_3X crystallizes in the hexagonal system whereas another $Eu_2B_5O_9X$ belongs to the orthorhombic (pseudotetragonal) system. The crystal structure of $Eu_2B_5O_9X$ was determined from three-dimensional X-ray diffraction data (R=0.054 for 1967 observed reflections of $Eu_2B_5O_9Cl$ and R=0.047 for 1979 observed reflections of $Eu_2B_5O_9Br$). The structure consists of a three-dimensional $(B_5O_9)_\infty$ network, in which the B_5O_{12} groups of three BO_4 tetrahedra and two BO_3 triangles are linked together by sharing cornered oxygens. The Eu^{2+} and Br^- ions are located in tunnels of the $(B_5O_9)_\infty$ network extending along the c axis. Each Eu^{2+} ion is surrounded by two X^- ions and seven O^{2-} ions and is isolated from the neighboring Eu^{2+} ions by the borate units and X^- ions. From the magnetic susceptibility and magnetization measurements at low temperatures, Eu_2BO_3X and $Eu_2B_5O_9X$ were found to be a ferromagnet with $T_C \simeq 5$ K and a paramagnet, respectively. The compounds as diluted the Eu^{2+} ions in $Eu_2B_5O_9X$ matrix with alkaline earth cations are efficient photoluminescent materials whereas no luminescence is observable. This finding can be accounted for by estimating the magnitudes of the Coulomb and exchange interactions between neighboring Eu^{2+} ions in $Eu_2B_5O_9X$, which are expected to be weak from the magnetism and the arrangement of anions around the Eu^{2+} ions.

3. HIGH-PRESSURE SYNTHESIS AND PROPERTIES OF EUROPIUM(II) METABORATE

3-1. Introduction

Some of alkaline earth borates, aluminates, and gallates are transformed into high-pressure phases, anion units changing from triangles to tetrahedra or from tetrahedra to octahedra.36) For metaborates, M^IBO_2 and $M^{II}B_2O_4$, there are two types of chain constructions, namely, one which consists of $(BO_2)_\infty$ chains sharing an oxygen of the BO_3 group (e.g., $LiBO_2$, CaB_2O_4, and SrB_2O_4)19,26,37) and another which contains condensed-ring anions of three BO_3 units, $(B_3O_6)^{3-}$ (e.g., $NaBO_2$ and BaB_2O_4).19,38) The borates of former type are easily transformed into several high-pressure phases, the triangularly coordinated borons in their units being partially or all changed into tetrahedrally coordinated borons by high-pressure treatments.39,40)

The calcium metaborate CaB_2O_4 crystallizes with four different structures, three orthorhombic and one cubic modifications. Phase α-CaB_2O_4, which is stable at atmospheric pressure, contains only triangularly coordinated borons, and each Ca atom is surrounded by eight oxygens. In β-CaB_2O_4, 50 % of the B atoms transform into the tetrahedral coordination, although the Ca atoms have the same coordination number of 8 as in α-CaB_2O_4. Phase γ-CaB_2O_4 consists of a three-dimensional network of two triangular and four tetrahedral borons, a $(B_6O_{12})_\infty$ network, and 33 % of the Ca atoms increase their coordination number from 8 to 10. Finally in δ-CaB_2O_4 all B atoms are tetrahedrally coordinated, and this phase consists of a $(B_3O_6)_\infty$ network, and the coordination number of all B atoms increases to 12. On the other hand, SrB_2O_4 can crystallize only with three forms different from the case of CaB_2O_4.41) Phase β-SrB_2O_4 has not been obtained. Since the modifications of CaB_2O_4 and SrB_2O_4 are isostructural with each other, the boron and the strontium coordination numbers in each phase of SrB_2O_4 are the same values as those for the corresponding calcium analogues.

The europium(II) metaborate, EuB_2O_4, which has been obtained in the previous chapter and also consists of $(BO_2)_\infty$ chains, is isostructural with the α form of CaB_2O_4 and SrB_2O_4. It is , therefore, expected that the similar polymorphism to that of CaB_2O_4 or SrB_2O_4 will be observed on this borate.

The present study has been carried out with a view to synthesizing the high-pressure phases of EuB_2O_4, $SrB_2O_4:Eu^{2+}$, and $CaB_2O_4:Eu^{2+}$ and characterizing them by X-ray analyses and measurements of magnetic susceptibility and ultraviole luminescence. In addition, the high-pressure synthesis of $SrAl_4O_7$ has been made, and the crystal structure of the resulting phase, β-$SrAl_4O_7$, has been determined.

3-2. Experimental

A. Sample preparation. The atmospheric pressure phases, α-EuB_2O_4 and α-$MB_2O_4:Eu^{2+}$ (M=Ca and Sr) were obtained according to the methods described previously. The high-pressure treatments of the samples were carried out with a Dia 15 cubic anvil type apparatus in the following way: the powdered samples were packed into boron nitride cups, illustrated elsewhere.42) After the samples were quenched to room temperature, and then the pressure released.

The high-pressure phase, β-$SrAl_4O_7$, was obtained as a by-product for runs in which single crystals of $SrAl_2O_4$ were grown using water as a solvent at 35-50 kbar (1 bar=10^5 Pa) and 1000-1300°C. The polycystalline sample of β-$SrAl_4O_7$ was prepared from a mixture of α-$SrAl_4O_7$ and water by the treatment of 50 kbar and 1200°C for 60 min. The samples of α-$SrAl_4O_7$ were obtained by heating the stoichiometric mixture of $SrCO_3$ and γ-Al_2O_3 (99.985 %) at 1300°C for 5×2 h (two times) in air. For trials, in which water was not applied for the preparation, β-$SrAl_4O_7$ could not be prepared up to 50 kbar and unknown phases were formed. The single crystals were grown from a mixture of $SrAl_2O_4$ and water by cooling to 800°C at a rate of about 2°C/min after maintaining at 40 kbar and 1300°C for 60 min. The resulting phases were characterized by the techniques of X-ray analysis as described previously.

B. Magnetic susceptibility and optical measurements. The descriptions of the apparatuses and methods used for measurements are made in the foregoing chapter.

3-3. Results

A. EuB_2O_4. The resulting phases of EuB_2O_4 from high-pressure treatments were identified by X-ray powder analysis on the basis of the lattice parameters for modifications of SrB_2O_4 and termed in a similar manner as the corresponding calcium and strontium analogues. The phase diagram of EuB_2O_4 is shown in Fig. 1. This diagram consists of four regions: the first (atmospheric pressure) phase α-EuB_2O_4, the third phase γ-EuB_2O_4, the fourth phase δ-EuB_2O_4, and the decomposed phase EuB_4O_7+ $Eu_2B_2O_5$. The second phase β-EuB_2O_4 was not obtained as well as β-SrB_2O_4. Under the conditions above 40 kbar and 900°C, EuB_2O_4 appeared to decompose into EuB_4O_7 and $Eu_2B_2O_5$ as follows:

$$3\ EuB_2O_4 \longrightarrow EuB_4O_7 + Eu_2B_2O_5. \qquad (3\text{-}1)$$

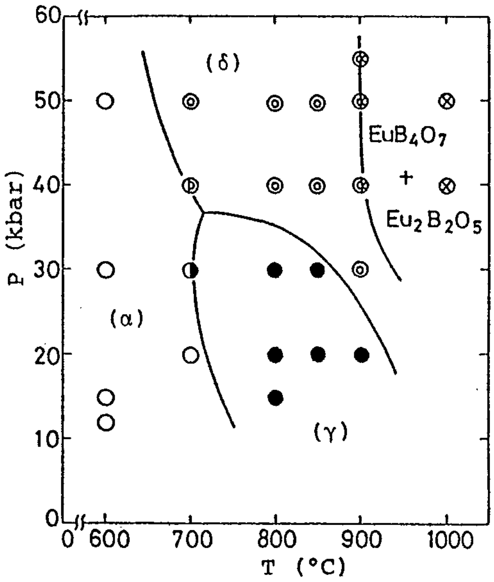

Figure 1. Phase diagram of EuB_2O_4.

According to the above scheme, the overall mole number reduces from 3 to 2 and the volume of the sample also reduces to 87.5 %. This agrees with the fact that one product of decomposition of SrB_2O_4 has been found to be SrB_4O_7 by Krogh-Moe.43) The crystallinities of the resulting phases of EuB_2O_4 were generally low.

The accurate lattice parameters refined from the X-ray powder data, the density, and the color for the resulting phases of EuB_2O_4 are summarized in Table I. The phases, γ- and δ-EuB_2O_4, crystallize in the orthorhombic system ($Pna2_1$) with 12 molecules per unit cell and in the

Table I. High-pressure polymorphism of EuB_2O_4

Phase		Lattice parameters (Å)				S.G.	Z	Density (g/cm^3)		Color
		CaB_2O_4[a]		SrB_2O_4[a]	EuB_2O_4			Dm	Dx	
α		a= 6.214 b=11.604 c= 4.284		a= 6.589 b=12.018 c= 4.337	a= 6.593(1) b=12.063(2) c= 4.343(1)	Pnca	4	4.61	4.57	Light-yellow
	12 kbar									
β		a= 8.369 b=13.816 c= 5.007	8 kbar			Pccn	8			
	15 kbar									
γ		a=11.380 b= 6.382 c=11.304		a=12.426 b= 6.418 c=11.412	a=12.44(1) b= 6.43(1) c=11.42(1)	$Pna2_1$	12	5.22^b	5.18	Yellow
	25 kbar		15 kbar							
δ		a= 9.008		a= 9.222	a= 9.240(1)	Pa3	12	5.57^b	6.00	Yellow
EuB_4O_7 + $Eu_2B_2O_5$				—	—	—	—	5.40^b	5.22	Dark-yellow

[a] Ref. 41. The treatment temperatures are 600°C for SrB_2O_4 and 900°C for CaB_2O_4, respectively.

[b] These data were obtained on the sintered samples with the dimension: ca. 4 mmϕ×3 mm.

cubic system (Pa3) with 12 molecules per unit cell, respectively. The observed density Dm of each phase is in good agreement with the calculated value Dx except for δ-EuB_2O_4. The values of Dm have been obtained on the sintered samples taken out from the boron nitride cell, and hence the pellet of δ-EuB_2O_4 seems to contain some pores. The crystallographic properties of polymorphism of EuB_2O_4 are completely equal to those of SrB_2O_4, but the transition pressures and temperatures of both borates differ from each other: α-EuB_2O_4 transforms into other phases at a higher temperature than that of α-SrB_2O_4. This suggests that the bond strength of Eu-O must be stronger than that of Sr-O.

The magnetic and luminescent data of EuB_2O_4 given in Table II are obtained for phase α (untreated, phase γ (20 kbar, 800°C) phase δ (50 kbar, 850°C), and the decomposed phase (50 kbar, 1000°C). The effective magnetic moment per Eu^{2+} ion (μ_{eff}) of the resulting phases are slightly smaller than the theoretical value of 7.94 μ_B. This implies that a very small amount of Eu^{2+} ion has been oxidized into Eu^{3+} ions in the high-pressure treatments because a μ_{eff} value of the Eu^{3+} ion is about 3.6 μ_B.[44)] The paramagnetic Curie temperature θ_C was about -5 K for phase γ, about 0 K for phase δ, and about -10 K for the decomposed phase, respectively. It can be presumed that phase γ and the decomposed phase are antiferromagnetic, and phase δ is paramagnetic at low temperatures.

Table II. Magnetic and luminescent data for the various phases of EuB_2O_4

Sample	Phase	Treatment P (kbar)	 T (°C)	$\mu_{eff}(\mu_B)$	θ_C(K)	λ_{max}(nm)	I^a
a	α			7.88	-5	370	Very weak
b	γ	20	800	7.42	-5	370	Very weak
c	δ	50	850	7.62	0	410	Weak
d	EuB_4O_7 + $Eu_2B_2O_5$	50	1000	7.54	-10	368, 395	Weak

^{a}I = emission intensity.

The high-pressure phases of EuB_2O_4 were found to give the band emissions based on the $4f^7$-$4f^6 5d$ transition of the Eu^{2+} ion. The peak positions of their emissions shift to long wavelength and their light outputs slightly increased with transformation into phase δ and the decomposed phase. The emission spectral distribution and the excitation spectra of phase δ and the decomposed phase are shown in Fig. 2.

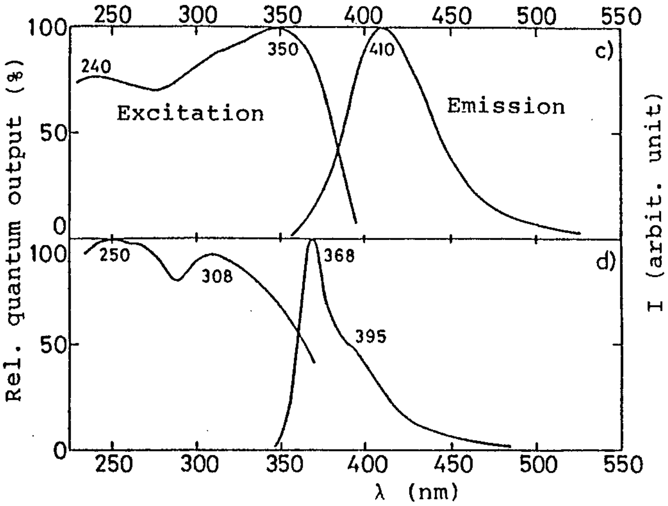

Figure 2. Spectral energy distribution and relative excitation spectra of the emissions of δ-EuB_2O_4 and the decomposed phase.

The emission intensity for any modification of EuB_2O_4 was weak. Their emission patterns were illustrated on the basis of the energy output of the photomultiplier. The emissions of phase δ and the decomposed phase consist of a band at about 410 nm and two bands at about 368 and 395 nm, respectively, although phases α and γ give very weak emissions at about 370 nm. The emission at about 370 nm of the decomposed phase must be attributable to the one product of decomposition, EuB_4O_7, since it gives a relatively strong emission at about 370 nm as described previously.

B. SrB_2O_4:Eu^{2+} and CaB_2O_4:Eu^{2+}. For the luminescent properties of Eu^{2+} ion in high-pressure phases of metaborate, the high-pressure treatments and luminescent measurements were made on Eu^{2+}-activated alkaline earth metaborates, SrB_2O_4:Eu^{2+} and CaB_2O_4:Eu^{2+}. The resulting phases of $Sr_{0.99}Eu_{0.01}B_2O_4$ from the treatments at 15-30 kbar and 700°C and their luminescent data are shown in Table III and Fig. 3. It is seen that the emission peak positions of samples containing the δ phase shift to long wavelength and bandwidths at half maximum increase from 20 to 43 nm compared with those of other phases. Whereas the peak positions of phases α and γ are 367 nm and their emission shapes are closely similar to each other, phase δ gives a strong emission peaking at 395 nm. Sample c of phase δ mixed with a small amount of phase γ gives an emission at 410 nm, which is positioned at a slightly longer wavelength than that of the pure phase of δ-$Sr_{0.99}Eu_{0.01}B_2O_4$. All phases of $SrB_2O_4:Eu^{2+}$ give the excitation spectra consisting of two bands peaking at 250±6 and 310±4 nm. The fivefold degenerated 5d level of the excited ($4f^6 5d$) configuration is split into several levels by the crystal field formed by anions around the Eu^{2+} ions. In solids, the absorption of Eu^{2+} ions in the near-ultraviolet region is generally agreed to be attributable to the 4f→5d transition,[45)] and the matrix of SrB_2O_4 has no absorption band in this region. Therefore, the excitation patterns as mentioned above should be due to the splitting of the 5d level.

Table III. Resulting phases and luminescent data for $Sr_{0.99}Eu_{0.01}B_2O_4$ from high-pressure treatments

Sample	Phase	P (kbar)[a]	λ_{max} (nm)	R.E.I. (%)[b]
a	α		367	1
b	γ	15	367	1
c	δ + γ(minor)	20	404	30
d	δ	30	395	39

[a] Treatment temperature = 700°C. [b] The values were measured under 254 nm excitation at 300 K.

It was found that the relative emission intensity of samples remarkably increased with transformation into phase δ. The treatment pressure dependence of the relative emission intensity of $Sr_{0.99}Eu_{0.01}$-

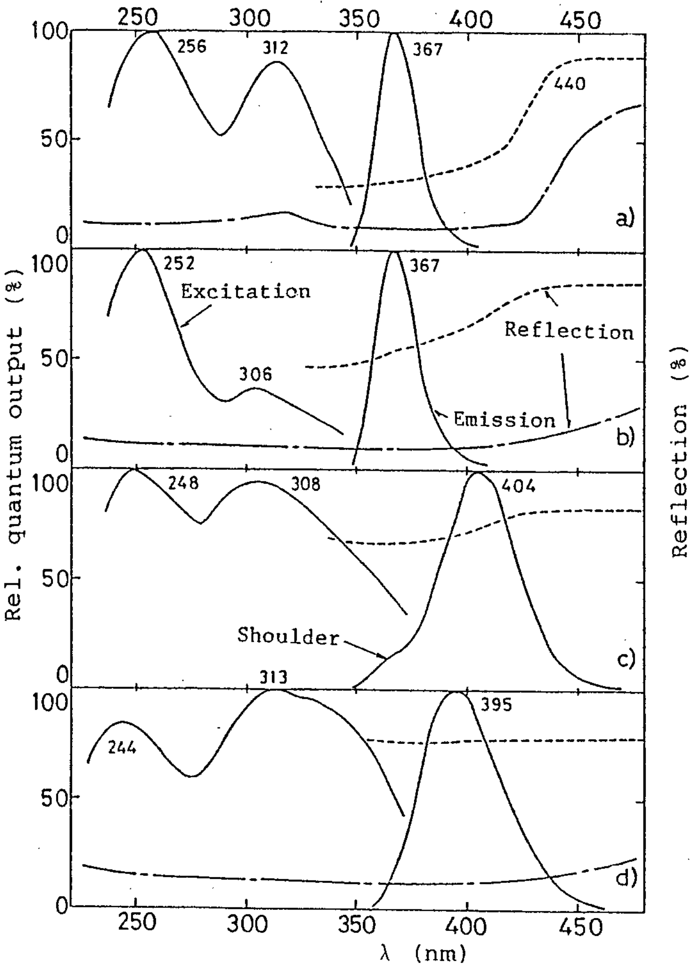

Figure 3. Relative emission and excitation spectra (solid line) for the various phases of $Sr_{0.99}Eu_{0.01}B_2O_4$ and diffuse reflection spectra (dashed line for $Sr_{0.99}Eu_{0.01}B_2O_4$ and dashed-dotted line for EuB_2O_4).

B_2O_4 is shown in Fig. 4. It is noticeable that the relative emission intensity drastically increases to about 50 times under 254 nm excitation and about 100 times under an optimum (313 nm) excitation for phase δ with transformation from phase γ to δ. The Eu^{2+} concentration quenching effect to the relative emission intensity of δ-$Sr_{1-x}Eu_xB_2O_4$ is summarized in Fig. 5. An optimum concentration is seen to be about 1 at%, at which its relative emission intensity is about 40 % under 254 nm excitation and about 60 % under 313 nm excitation. Since this value is as high as that of $BaB_8O_{13}:Eu^{2+}$ which is an efficient phosphor, δ-

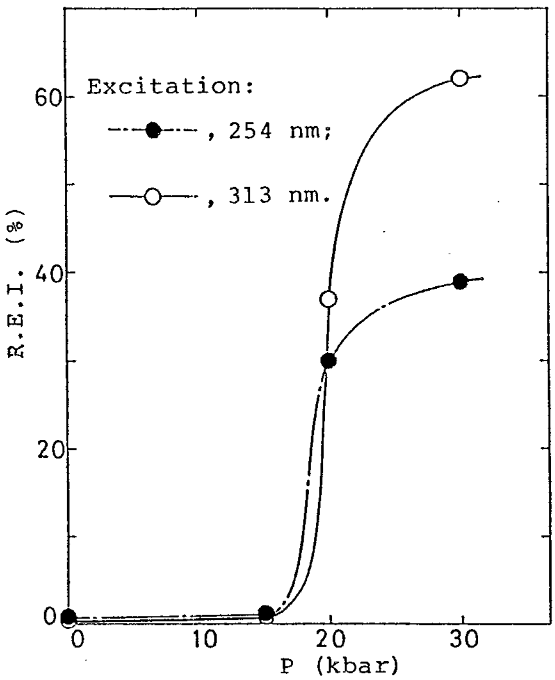

Figure 4. Relative emission intensity vs. treatment pressure for $Sr_{0.99}Eu_{0.01}B_2O_4$.

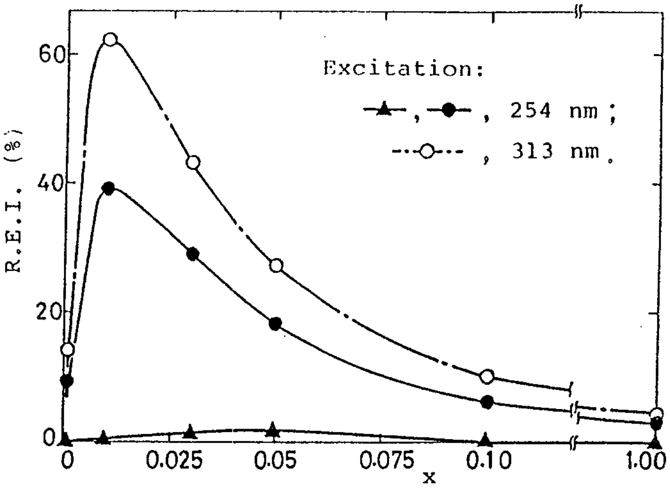

Figure 5. Relative emission intensity vs. Eu^{2+} content (x) for the high-pressure phases of $Sr_{1-x}Eu_xB_2O_4$: ▲, α; ● and ○, δ.

$SrB_2O_4:Eu^{2+}$ also is an efficient one.

The resulting phases of $CaB_2O_4:Eu^{2+}$ from the treatments at the various conditions and their luminescent data are summarized in Table IV and Fig. 6. The borate CaB_2O_4 crystallizes with four different structures. However, no pure phase of β-$CaB_2O_4:Eu^{2+}$ was obtainable.

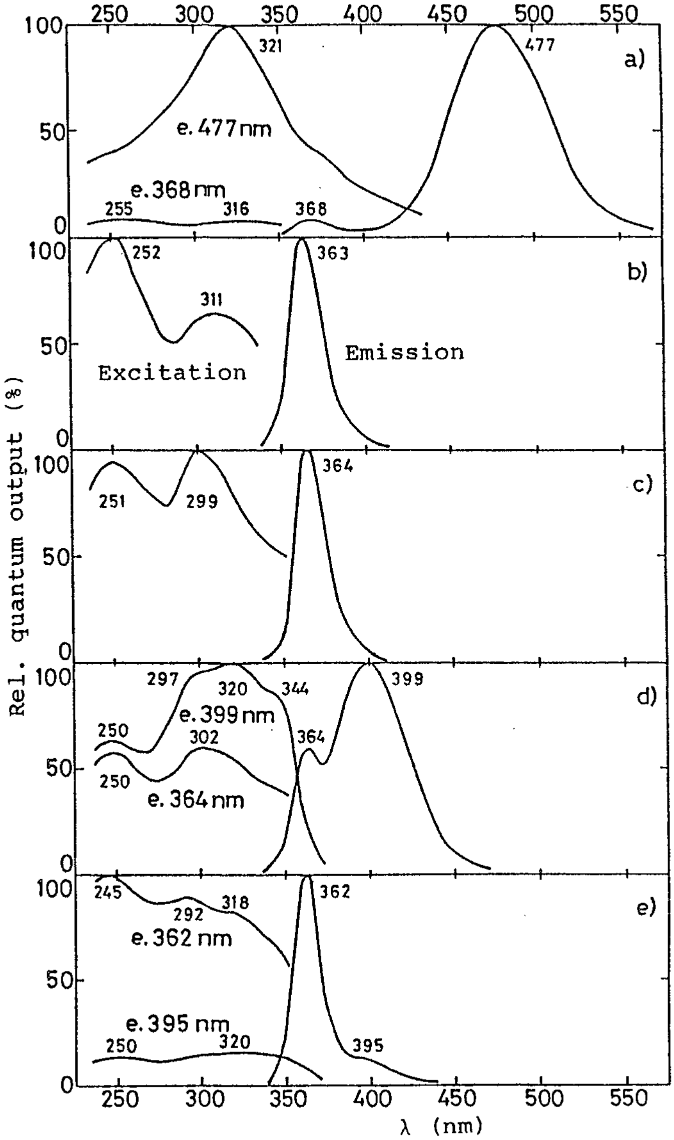

Figure 6. Relative emission and excitation spectra for the various phases of $Ca_{0.94}Eu_{0.06}B_2O_4$ ($Ca_{0.99}Eu_{0.01}B_2O_4$ for b).

Table IV. Resulting phases and luminescent data[a] for $Ca_{1-x}Eu_xB_2O_4$ from high-pressure treatments

Treatment[b]		Phase and luminescent data				
P (kbar)	T (°C)	CaB_2O_4	$Ca_{0.99}Eu_{0.01}B_2O_4$	$Ca_{0.97}Eu_{0.03}B_2O_4$	$Ca_{0.94}Eu_{0.06}B_2O_4$	$Ca_{0.90}Eu_{0.10}B_2O_4$
		α	α; about 450 nm; very weak	α; about 450 nm; weak	α; 368, 477 nm; <1 %	α; 367, 479 nm; <<1 %
13	900	α and β	b): α and β; 363 nm; weak		α; 367, 458 nm; 2 %	
15	800			β and γ; 363 nm; <1 %		
15	900				α; 363 nm; 2%	
18	900			γ; 363 nm; <1 %	c): γ; 364 nm; 3 %	
20	800			γ; 360, 395 nm; <1 %		
20	900	γ	γ; 362 nm; weak	γ and δ; 361, 396 nm; 2 %	d): γ; 364, 399 nm; 5 %	
22	900				δ and γ; 362, 395 nm; 9 %	
30	900	δ	δ; 359 nm; 26 %		e): δ; 362, 394 nm; 32 %	
31	900			δ; 361, 395 nm; 18 %	δ; 361, 394 nm; 13 %	

[a] The values of λ_{max} and R.E.I. under 254 nm excitation at 300 K are listed in this table. [b] Treatment period = 30–60 min.

The fact that phase β hardly forms with increasing the value of x in $Ca_{1-x}Eu_xB_2O_4$ is due to a crystallographic mismatching between the radii of Ca^{2+} and Eu^{2+} ions. The luminescent properties of the modifications of $CaB_2O_4:Eu^{2+}$ considerably differ from those of $SrB_2O_4:Eu^{2+}$. Phase α of $Ca_{0.94}Eu_{0.06}B_2O_4$ gives two emission bands peaking at 368 and 477 nm; its excitation spectra consist of a broad band at 321 nm for the 477 nm emission band and two bands at 255 and 316 nm for the 368 nm emission band. For the mixed phase of α- and β-$Ca_{0.99}Eu_{0.01}B_2O_4$, the emission spectrum consists of a band at about 363 nm, and its excitation pattern has two paeks at about 250 and 300 nm as well as that of the 368 nm emission band of phase α. The phase γ-$Ca_{0.94}Eu_{0.06}B_2O_4$ was found to give two types of emission patterns depending on the treatment conditions. One type was observed on sample c treated at 18 kbar and 900°C. Its emission and excitation spectra consist of a band and two bands similar to the patterns observed on the mixed-phase sample b, respectively. Another type, viz., sample d obtained at the treatment condition of 20 kbar and 900°C, gives two emission bands peaking at 364 and 399 nm, and its excitation spectra consist of four bands at about 250, 297, 320, and 344 nm for the 399 nm emission band and two bands at about 250 and 302 nm for the 364 nm emission band. These excitation patterns differ from each other; particularly, the excitation spectrum of the 399 nm emission band is specific among a series of high-pressure phases of $CaB_2O_4:Eu^{2+}$. The emission pattern of δ-$Ca_{0.94}Eu_{0.06}B_2O_4$ is peaking at 362 and 396 nm, and its excitation spectra have three peaks at 245, 292, and 318 nm for the 362 nm emission band. The relative emission intensities of $CaB_2O_4:Eu^{2+}$ also are observed to increase with transformation into the higher pressure phase. It is noticeable that the emission bands around 365 nm of samples a, b, c, and d are similar to those of phases α and γ of EuB_2O_4 and $SrB_2O_4:Eu^{2+}$, the band at 399 nm of sample d to that of δ-EuB_2O_4 and δ-$SrB_2O_4:Eu^{2+}$, and the pattern of sample e to that of the decomposed phase of EuB_2O_4, respectively.

In order to interpret these phenomena, the lattice parameters of the resulting phases of $Ca_{0.94}Eu_{0.06}B_2O_4$ were measured over a range of $0.11<(\sin\theta/\lambda)<0.32$ Å^{-1}. In Table V, their lattice parameters are summarized together with those of CaB_2O_4 measured at the same condition. The lattice parameters of CaB_2O_4 are smaller than those of EuB_2O_4 because of the difference between the radii of Ca^{2+} and Eu^{2+} ions. For phase α, the lattice parameters of $Ca_{0.94}Eu_{0.06}B_2O_4$ should be larger than those of CaB_2O_4, but those of the other phases of CaB_2O_4 and $Ca_{0.94}Eu_{0.06}B_2O_4$ are very close to each other. This suggests that the EuB_2O_4 phase is pressed out from the $CaB_2O_4:Eu^{2+}$ phase by the high-pressure treatments, and hence the emission pattern of $CaB_2O_4:Eu^{2+}$ are assigned as follows: for phase α, the emission at about 477 nm corresponds to the band from the Eu^{2+} ions in the matrix α-CaB_2O_4 because the emission at 368 nm must be derived from α-EuB_2O_4 in the grain boundaries. The fact that the emission peak position of α-$CaB_2O_4:Eu^{2+}$ (477 nm) considerably shifts to long wavelength compared with those of α-$SrB_2O_4:Eu^{2+}$ and α-EuB_2O_4 may be due to a strain of the matrix induced by substituting the larger Eu^{2+} ions for the smaller Ca^{2+} ions. On the basis of the phase diagram of EuB_2O_4 (see Fig. 3), the emissions at about 364 nm of samples b, c, and d are identified with the γ-EuB_2O_4 phase and the band at 399 nm of sample d corresponds to the emission pattern of δ-EuB_2O_4, although the peak positions of the corresponding emissions from EuB_2O_4 and $CaB_2O_4:Eu^{2+}$ somewhat deviate from each other. The emission pattern of sample e results from the decomposed phase of EuB_2O_4 in the grain boundaries of δ-CaB_2O_4. It is, consequently, concluded that the luminescent properties of the high-pressure phases of $CaB_2O_4:Eu^{2+}$ are due to those of the EuB_2O_4 phase pressed out from the

Table V. Lattice parameters[a] for CaB_2O_4 and $Ca_{0.94}Eu_{0.06}B_2O_4$ (Å)

Compound	α	β	γ	δ
CaB_2O_4	a= 6.215(3) b=11.611(4) c= 4.280(2)	a= 8.38(7) b=12.72(6) c= 4.94(7)	a=11.378(2) b= 6.3825(7) c=11.310(1)	a= 9.021(6)
$Ca_{0.94}Eu_{0.06}B_2O_4$	a= 6.259(5) b=11.623(6) c= 4.282(3)		a=11.403(2) b= 6.390(7) c=11.307(4)	a= 9.0169(6)

[a] Refinement range = $0.11<(\sin\theta/\lambda)<0.32$ $Å^{-1}$.

matrix of CaB_2O_4. The fact that the relative emission intensities of the high-pressure phases of CaB_2O_4:Eu^{2+} are relatively greater than those of EuB_2O_4 may be attributable to the decrease of the concentration quenching effect by dispersing the EuB_2O_4 phase into the grain boundaries of CaB_2O_4.

C. β-$SrAl_4O_7$. A new high-pressure phase was obtained as a by-product for runs in which single crystals of $SrAl_2O_4$ were grown using water as a solvent at 35-50 kbar and 1000-1300°C. Its chemical composition was found to be $SrAl_4O_7$ from X-ray analyses, and thus it was termed β-$SrAl_4O_7$.

The single crystals used for X-ray measurements were grown from a mixture of $SrAl_2O_4$ and water by cooling to 800°C at a rate of about 2°C/min. Their Weissenberg photographs have shown the following systematic absences: $h+k=2n+1$ for hkl reflections; $h=2n+1$ and $k=2n+1$ for hk0 reflections, which correspond to a space group Cmma. The crystal data of β-$SrAl_4O_7$ are presented together with those of the α form in Table VI. The cell parameters were refined by the least-squares treatment of the X-ray powder diffraction pattern calibrated with high-purity silicon as an internal standard.

The coordinate of the Sr atom firstly was determined by a three-dimensional Patterson function, and the remaining Al and O atoms were located on successive Fourier maps. The O(3) atom is located at the general position [16(o) site] while the other atoms occupy the special positions: Sr, 4(e) site; Al(1), 4(c) site; Al(2), 4(b) site; Al(3) and O(2), 8(m) site; O(1), 4(g) site. Isotropic refinements were made on all atomic parameters by the block-diagonal least-squares method with HBLS-V22) to give $R=0.047$ and $R_w=0.061$. The atomic scattering factors for Sr, Al, and O atoms were those listed in International Tables for X-ray Crystallography.24) The weighting scheme $w=(F_m/F_o)^2$ for $F_o>F_m$ (=10.0) and $w=1.0$ for $F_o \leq F_m$ (=10.0) was employed. The final positional and thermal parameters are listed in Table VII.

The interatomic distances and angles in β-$SrAl_4O_7$ are summarized in Table VIII. The coordination number for a quarter of Al atoms increases from 4 to 6 by the high-pressure treatment, and hence there

Table VI. Crystal data for α- and β-$SrAl_4O_7$

(a) α form[a]

F.W.= 307.54
Monoclinic
Space group C2/c
a=13.039(9) Å
b= 9.011(5)

c= 5.536(3) Å
β=106.12°
V=624.9 $Å^3$
Z=4
Dx=3.268 g/cm^3

(b) β form

F.W.= 307.54
Orthorhombic
Space group Cmma
a= 8.085(5) Å
b=11.845(8)
c= 4.407(3)
V=422.0(5) $Å^3$

λ=0.71069 Å
μ(Mo Kα)=13.20 mm^{-1}
Dm=4.80 g/cm^3
Dx=4.84
Z=4
F(000)=584
Cryst size
0.16×0.13×0.08 mm

[a] See ref. 46.

Table VII. Final positional and thermal parameters for β-$SrAl_4O_7$, with their standard deviations in parentheses

Atom	x	y	z	B ($Å^2$)
Sr	1/4	1/4	0	0.34(1)
Al(1)	0	0	0	0.26(5)
Al(2)	1/4	0	1/2	1.12(7)
Al(3)	0	0.136(4)	0.454(4)	1.30(5)
O(1)	0	1/4	0.335(10)	0.45(14)
O(2)	0	0.128(7)	0.782(7)	0.39(9)
O(3)	0.144(5)	0.073(5)	0.302(5)	0.33(6)

are two types of aluminate units, $Al(1)O_6$ octahedra, and $Al(2)O_4$ and $Al(3)O_4$ tetrahedra. These units are appreciably distorted from the

Table VIII. Interatomic distances (Å) and angles (°) in β-$SrAl_4O_7$, with their estimated standard deviations in parentheses

(a) The $(Al_4O_7)_\infty$ network

	Al(1)-octahedron		
Al(1) -O(2)	1.795(7)(×2)	O(2)-Al(1)-O(3)	89.5(3)(×4)
-O(3)	1.968(5)(×4)		90.5(3)(×4)
		O(3)-Al(1)-O(3)	72.5(2)(×2)
			107.5(2)(×2)
	Al(2)-tetrahedron		
Al(2) -O(3)	1.498(5)(×4)	O(3)-Al(2)-O(3)	108.7(3)(×2)
			109.5(3)(×2)
			110.2(3)(×2)
	Al(3)-tetrahedron		
Al(3) -O(1)	1.449(11)	O(1)-Al(3)-O(2)	115.0(5)
-O(2)	1.449(8)	O(1)-Al(3)-O(3)	107.2(5)(×2)
-O(3)	1.537(6)(×2)	O(2)-Al(3)-O(3)	113.8(4)(×2)
		O(3)-Al(3)-O(3)	98.5(3)

(b) Sr-O distances

Sr -O(1)	2.503(10)(×2)	Sr -O(3)	2.627(5)(×4)
-O(2)	2.664(7)(×4)		

regular octahedron and tetrahedron, the Al-O bond lengths and O-Al-O bond angles being 1.795-1.968 Å and 72.5-107.5° for the $Al(1)O_6$ unit and 1.449-1.537 and 98.5-115.0° for the $Al(2)O_4$ and $Al(3)O_4$ units. It is noticeable that the Al-O distances for the tetrahedral units are considerably shorter than those in some aluminates (atmospheric-pressure phases), e.g., 1.718-1.808 Å for α-$SrAl_4O_7$ 46) and 1.728-1.779 Å for $CaAl_2O_4$. 47)

A projection of the β-$SrAl_4O_7$ structure viewed along the c axis is shown in Fig. 7. The $Al(1)O_6$ and $Al(3)O_4$ units can be seen to have the mirror symmetry on the (100) or (200) plane and the $Al(2)O_4$ tetrahedron shows the symmetry of twofold rotation around an axis parallel to the c axis. The structure consists of a three-dimensional $(Al_4O_7)_\infty$ network of octahedral and tetrahedral units with shared corner O atoms, which is appreciably denser than the structural framework of α-$SrAl_4O_7$. This reflects the observation that the density of $SrAl_4O_7$ drastically increases with the phase transformation from α to δ (see Table VI).

The structure viewed along the a axis is illustrated in Fig. 8.

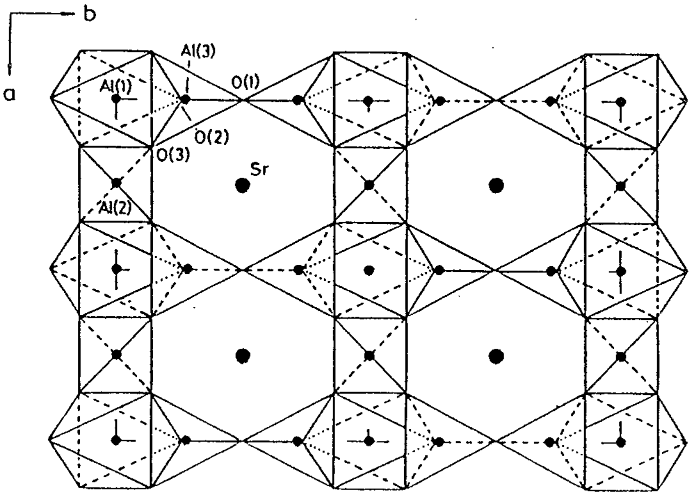

Figure 7. A projection of the β-$SrAl_4O_7$ structure viewed along the c axis.

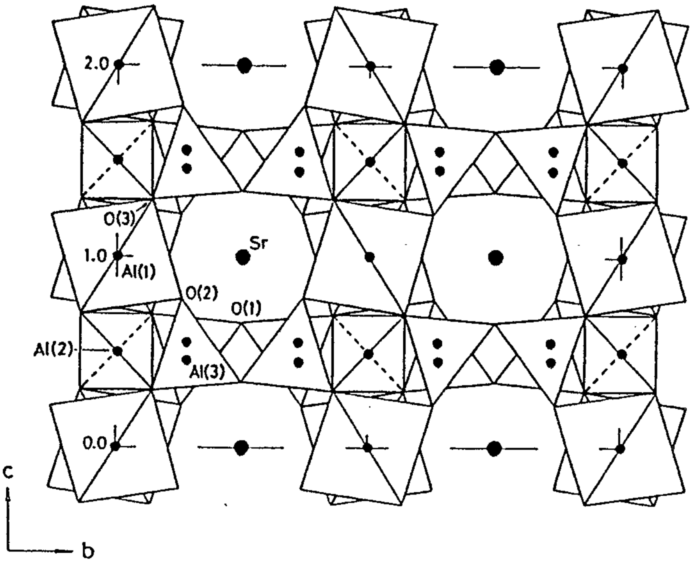

Figure 8. A projection of the β-$SrAl_4O_7$ structure viewed along the a axis.

The units of Al(1)O_6 and Al(3)O_4 are linked together to form a kind of layer on the (100) or (200) plane, which is three-dimensionally connected with the other layers by Al(2)O_4 tetrahedra. The Sr atoms are located in tunnels of $(Al_4O_7)_\infty$ network running parallel to the a axis.

The anion environments around Sr atoms in α- and β-$SrAl_4O_7$ are illustrated in Fig. 9. The Sr atoms are surrounded by seven and ten O atoms for the α and β phases to form SrO_7 and SrO_{10} polyhedra. The Sr-O distances are closely similar to each other (mean values: 2.618 Å, α form; 2.617 Å, β form). The symmetry of SrO_7 polyhedra, because the SrO_{10} polyhedra have the symmetries of mirror and twofold rotation but the SrO_7 polyhedra show only that of twofold rotation around the Sr-O(1) axis.

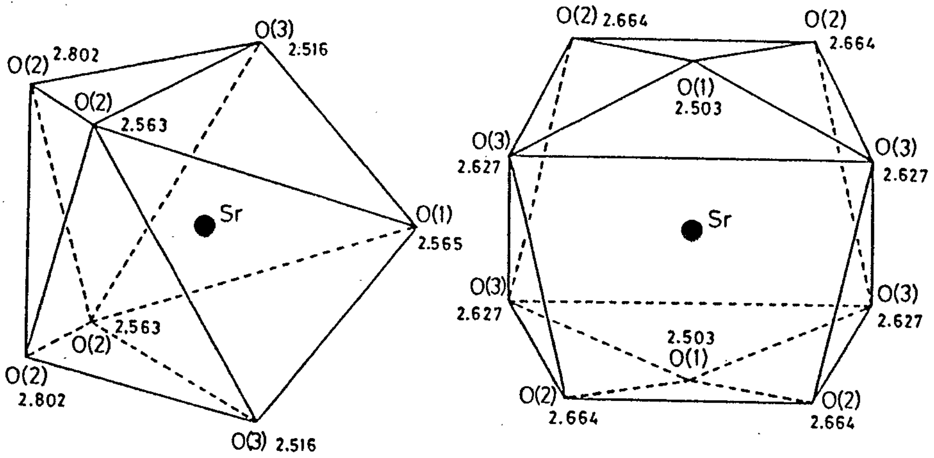

a) α form

b) β form

Figure 9. Schematic illustration of the SrO_n polyhedra in the $SrAl_4O_7$ polymorphs. The numerical values represent the Sr-O distances between nearest neighbors (Å).

3-4. Discussion

Among the modifications of CaB_2O_4 and SrB_2O_4, the detailed structural analysis has been performed only on α-, γ-, and δ-CaB_2O_4,[26,40] and α-EuB_2O_4 has been found to be entirely isostructural with α-CaB_2O_4. The structures of γ- and δ-CaB_2O_4 are illustrated in Fig. 10. As described previously, each Eu atom in α-EuB_2O_4 occupies a 4(c) site of space group Pnca and is surrounded by 8 oxygens. On the assumption that all atoms in the high-pressure phases of EuB_2O_4 are coordinated

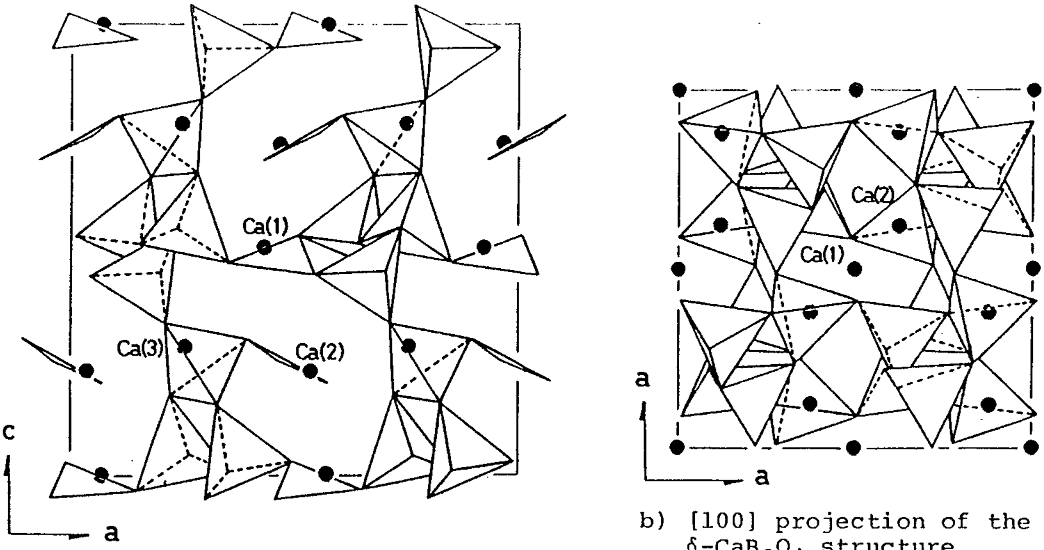

a) [010] projection of the γ-CaB_2O_4 structure

b) [100] projection of the δ-CaB_2O_4 structure

Figure 10. Crystal structures for the high-pressure phases of CaB_2O_4.

in a similar manner as those of CaB_2O_4, γ-EuB_2O_4 has three kinds of sites, Eu(1), Eu(2), and Eu(3), which belong to a 4(a) site of space group $Pna2_1$, and the coordination numbers of oxygen around the Eu atoms on those sites are 8 for Eu(1) and Eu(2) and 10 for Eu(3), respectively. While the Eu atoms in δ-EuB_2O_4 are placed on two sites, Eu(1) and Eu(2), which belong to 4(a) and 8(c) sites of space group Pa3 and those sites are surrounded by 12 oxygens. Phases α, γ, and δ consist of $(BO_2)_\infty$ chains, a network of B_6O_{12} units with two triangular and four tetrahedral borons, and a network of B_3O_6 units with three tetrahedral borons, respectively. It is noticeable that each Eu^{2+} ion in δ-EuB_2O_4 is considerably isolated from the neighboring Eu^{2+} ions by the surrounding BO_4 units compared with the cases of α- and γ-EuB_2O_4.

The magnetic properties of europium(II) compounds are approximately understood by considering the magnitude of the magnetic exchange and superexchange via O^{2-} ion interactions between the neighboring Eu^{2+} ions. In the case of europium(II) chalcogenides[2)] and titanates,[4)] their magnetism is mainly attributable to ferromagnetic

Eu^{2+}-Eu^{2+} exchange and antiferromagnetic 90°Eu^{2+}-O^{2-}-Eu^{2+} superexchange interactions between the nearest neighboring Eu^{2+} ions and a 180°Eu^{2+}-O^{2-}-Eu^{2+} superexchange interaction between the second-nearest neighboring Eu^{2+} ions (ferromagnetic or, as the case may be, antiferromagnetic). These interactions are sensitive to the interatomic Eu^{2+} spacings since the interactions between Eu^{2+} ions have been regarded as taking place with overlap of 4f and 5d orbitals. The interatomic distances between the neighboring Eu and O atoms in α- and δ-EuB_2O_4 are given in Table IX.

The mean distance between the nearest neighboring Eu^{2+} ions is 4.080 Å for α-EuB_2O_4 and 3.83 Å for the Eu(1) site and 3.89 Å for Eu(2) site in δ-EuB_2O_4. The fact that α-EuB_2O_4 is an antiferromagnet with T_N=3 K is due to the fact that the magnetic interaction between the nearest neighboring Eu^{2+} ions located in the (010) and (020) planes is expected to the ordering of spins only in those planes. The mean distance between the second-nearest neighboring Eu^{2+} ions around the Eu(1) site in δ-EuB_2O_4 is 5.15 Å and effective for the 180°Eu^{2+}-O^{2-}-Eu^{2+} interaction, but other distances longer than that are enough to interact with neighboring Eu^{2+} ions on the basis of other europium(II) compounds. Consequently the magnetism of δ-EuB_2O_4 is here considered on the basis of the magnetic interactions between the nearest neighboring Eu^{2+} ions and between the second-nearest neighboring Eu^{2+} ions around the Eu(2) site. The crystal structure of γ-EuB_2O_4 was too complex to discuss its magnetism. The anion environments around the nearest neighboring Eu^{2+} pairs in α- and δ-EuB_2O_4 are shown in Fig. 11.

Table IX. Interatomic distances in α- and δ-EuB_2O_4 (Å)

Phase		Eu-O	Eu-Eu nn	Eu-Eu nnn
α		2.624 (×8)	4.080 (×6)	6.632 (×10)
δ[a]	Eu(1)	2.80 (×12)	3.83 (×6)	6.00 (×4)
	Eu(2)	2.97 (×12)	3.89 (×4)	5.15 (×5)

[a] The values were estimated on the basis of the atomic parameters of δ-CaB_2O_4.

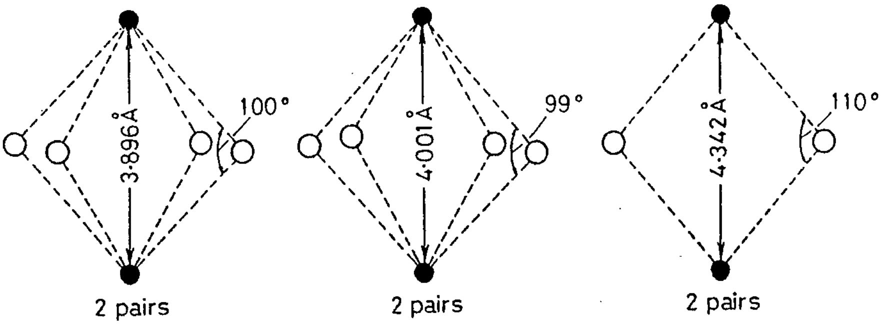

a) α-EuB_2O_4

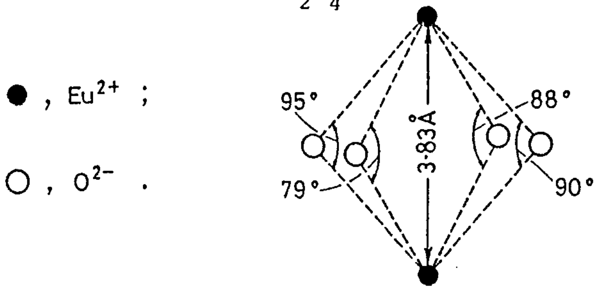

b) δ-EuB_2O_4

Figure 11. Anion environment around nearest neighboring Eu^{2+} ions in α- and δ-EuB_2O_4.

For α-EuB_2O_4, there are two types of interaction among the six nearest neighboring Eu^{2+} pairs: the first type is closely similar to that found in $EuTiO_3$[4a)] which is an antiferromagnet with T_N=5.3 K. In α-EuB_2O_4, four 90°Eu^{2+}-O^{2-}-Eu^{2+} superexchange interactions are dominant although the Eu^{2+}-O^{2-}-Eu^{2+} angles (99.0 and 100.4°) somewhat deviate from the value of 90°, since the Eu^{2+}-Eu^{2+} interaction is weak because the distance between the nearest neighboring Eu^{2+} pairs (3.896 and 4.001 Å) is not enough for its interaction. Therefore, the contribution of this type to the magnetism is antiferromagnetic. However, both of the exchange and superexchange interactions for the second type are weak because of the long distance between the nearest neighboring Eu^{2+} pair (4.342 Å) and the large deviation of the Eu^{2+}-O^{2-}-Eu^{2+} angle (110.3°) from the value of 90°. Therefore, α-EuB_2O_4 ia antiferromagnetic at low temperature owing to the contribution of the superexchange interaction of the first type.

On the other hand, the anion environments around the nearest Eu^{2+} neighboring Eu^{2+} ions in δ-EuB_2O_4 are mainly the same type as the first one of α-EuB_2O_4 and a nearest neighboring Eu^{2+} pair has four 90°Eu^{2+}-O^{2-}-Eu^{2+} superexchange pairs. The Eu^{2+}-Eu^{2+} distance is shorter than that of the first type of α-EuB_2O_4, and hence the Eu^{2+}-Eu^{2+} interaction in δ-EuB_2O_4 is not weaker than that in α-EuB_2O_4. If the contribution of the ferromagnetic Eu^{2+}-Eu^{2+} interaction to the magnetism is equal to that of the antiferromagnetic 90°Eu^{2+}-O^{2-}-Eu^{2+} interaction, the overall contribution of the magnetic interactions between the nearest neighboring Eu^{2+} ions should be paramagnetic. The 180°Eu^{2+}-O^{2-}-Eu^{2+} interaction between the second-nearest neighboring Eu^{2+} ions seems to be effective on the basis of the Eu^{2+}-Eu^{2+} distance and the Eu^{2+}-O^{2-}-Eu^{2+} angle: the Eu^{2+}-Eu^{2+} distance is 5.15 Å and enough to interact with the neighboring Eu^{2+} ions although the Eu^{2+}-O^{2-}-Eu^{2+} angle (162°) deviates from the value of 180°. However, all of the second-nearest neighboring Eu^{2+} ions which take part in this interaction are only those occupying the Eu(2) site and cannot interact with the neighboring Eu^{2+} ions on the Eu(1) site (see Fig. 10), and hence the contribution of the overall magnetism of δ-EuB_2O_4 must be small. Therefore, the magnetic behavior of δ-EuB_2O_4 is expected to be paramagnetic. However, the fact that the decomposed phase $EuB_4O_7 + Eu_2B_2O_5$ had the tendency to be antiferromagnetic although EuB_4O_7 and $Eu_2B_2O_5$ were paramagnetic as described previously could not be elucidated.

The emission assigned to the $4f^7$-$4f^6 5d$ transition strongly depends on anions and their arrangement around Eu^{2+} ions because of the broadly spaced d orbital, whereas the $4f^7$-$4f^7$ line emission is scarcely affected with the crystal field.10) The EuO_n polyhedra formed by oxygens around Eu^{2+} ions in the high-pressure phases are schematically illustrated in Fig. 12. The symmetries of their polyhedra are very low except for the $Eu(1)O_{12}$ polyhedron in phase δ which is cubically close packed. For phases α and γ, the symmetries of EuO_8 and EuO_{10} polyhedra are seen to be relatively similar to each other, but phase δ has the EuO_{12} polyhedra with a different symmetry from that of other phases. The assignment of their excitation spectra was unsuccessful because it was difficult to estimate the split energy levels of the 5d orbital of Eu^{2+} ions by the crystal field.

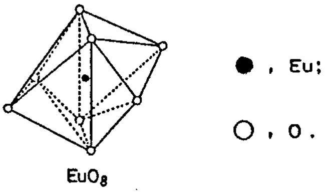

a) $\alpha\text{-}SrB_2O_4:Eu^{2+}$

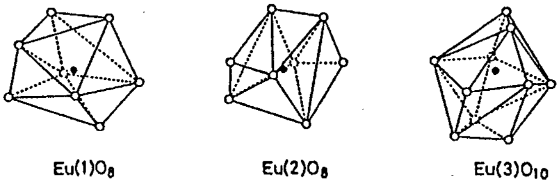

b) $\gamma\text{-}SrB_2O_4:Eu^{2+}$

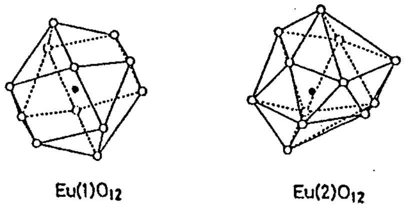

c) $\delta\text{-}SrB_2O_4:Eu^{2+}$

Figure 12. Oxygen coordination around Eu atoms in the high-pressure phases EuB_2O_4.

The emission peak positions of the high-pressure phases can be qualitatively interpreted by considering their emission processes on the basis of a configurational-coordinated diagram.[9)] The absorption corresponds to the transition of $4f \rightarrow 5d$, and then the electron in the excited ($4f^6 5d$) state move to the equilibrium distance (r_e) and undergo transition to the ground (${}^8S_{7/2}$) state. In this process, the value of r_e is not necessarily equal to that of the ground state (r_0) since the $4f^6 5d$ level strongly depends on the crystal field around the Eu^{2+} ion. For $\alpha\text{-}SrB_2O_4:Eu^{2+}$ or $\gamma\text{-}SrB_2O_4:Eu^{2+}$, the electrons which are excited by absorbing the energy of 4-5 eV (250-310 nm) transfer to the ground state at the equilibrium distance (r_e^{α}) or (r_e^{γ}), whereupon the emission at 367 nm is to be observed. If the minimum of the $4f^6 5d$ level of phase δ is slightly lowered or shifted to the right (Stokes shift: $\Delta r_e^{\delta} < \Delta r_e^{\alpha}$ or Δr_e^{γ}) compared with that of phase α or δ owing to the effect of its above-mentioned crystal field, the emission peak position of phase δ should shift to long wavelength. A nonradiative process from the excited to the ground state requires an activation energy ΔE, and if this value is very great, the possibility of the nonradiative process is very small. However, the difference between the activation energy, ΔE^{α} or ΔE^{γ} for phase α or γ and ΔE^{δ} for phase δ, is expected to be very small, and this cannot account for the fact that the relative emission intensity drastically increases with transformation into phase δ.

For the purpose of interpretation of this phenomenon, we measured reflection spectra on the high-pressure phases of $Sr_{0.99}Eu_{0.01}B_2O_4$ and EuB_2O_4 (see Fig. 3). However, we could not obtain their reflection petterns at a shorter wavelength than their emission peak positions, since the measured reflection spectra were mixed with the emissions from the samples owing to the integrating sphere attachment of the spectrophotometer, except those of the EuB_2O_4 modifications of which the emissions are very weak. For $Sr_{0.99}Eu_{0.01}B_2O_4$, phase α gives a broad band with the absorption edge at about 440 nm, and the emission band is completely included in this absorption region. The absorption edge shifts to short wavelength with transformation into the higher-pressure phase, and sample d (the pure phase of δ) no longer gives an apparent absorption edge. Phases α-, γ-, and δ-EuB_2O_4 give broad absorption bands, which completely include the corresponding emission bands. This suggests that some 5d levels of Eu^{2+} ions in the modifications of EuB_2O_4 are lowered by the interaction between the neighboring Eu^{2+} ions compared with the luminescent center, and the absorption in those levels cannot contribute to emit. The fact that the absorption spectra of γ- and δ-EuB_2O_4 are not sharp compared with that of α-EuB_2O_4 must be due to their low crystallinity. It is noticeable that the absorption spectra of α-EuB_2O_4 and α-$Sr_{0.99}Eu_{0.01}B_2O_4$ are closely similar to each other, and their emission bands completely overlap the sbsorption spectra. In general, the reflection spectra of Eu^{2+}-activated phosphors correspond to their excitation patterns except for the absorption of matrixes, and the degree of overlaps for the emission and excitation bands is small. That is in good agreement with the case of δ-$Sr_{0.99}Eu_{0.01}B_2O_4$ but not with the case of α- and γ-$Sr_{0.99}Eu_{0.01}B_2O_4$. If the Eu^{2+} ions in SrB_2O_4:Eu^{2+} form a kind of " cluster," namely, a number of Eu^{2+} ions localized in a region of which the Eu^{2+} concentration is very high and enough to interact with the neighboring Eu^{2+} ions, $SrB_2O_4:Eu^{2+}$ gives the same absorption pattern as EuB_2O_4.

From Fig. 10, phases α, γ, and δ consist of $(BO_2)_\infty$ chains, the $(B_6O_{12})_\infty$ network, and the $(B_3O_6)_\infty$ network, and the lower pressure phase is seen to be the more " open " structure than the higher pressure one. It seems that the sites which the Eu^{2+} ions in α-$SrB_2O_4:Eu^{2+}$ can occupy are located on (010) and (020) planes, and the Eu^{2+} ions have a tendency to be concentrated on those planes. However, such tendency in δ-$SrB_2O_4:Eu^{2+}$ must be very small since the Eu^{2+} ions are completely surrounded by the BO_4 units of the $(B_3O_6)_\infty$ network and hardly migrate to other sites. Consequently, the amount of the cluster in δ-$SrB_2O_4:Eu^{2+}$ must be smaller than that of other phases. This is supported by the following facts: (a) the reflection patterns of phase α or γ of $SrB_2O_4:Eu^{2+}$ and EuB_2O_4 are in agreement with each other different from those of phase δ. (b) α-$SrB_2O_4:Eu^{2+}$ in which the Eu^{2+} concentration is relatively high (>10 at%) has a tendency to be $\theta_C<0$ K, and this suggests magnetic interactions between the neighboring Eu^{2+} ions. (c) The color of α-$SrB_2O_4:Eu^{2+}$ changes from pale yellow-white to white with transformation into the high-pressure phases because the cluster should be colored with light yellow as well as α-EuB_2O_4.

The concentration quenching phenomena of Eu^{2+}-containing phosphors are interpreted by considering the energy transfer from Eu^{2+} to Eu^{2+} ions on the basis of the Dexter theory,31) in which the nonradiative process is regarded as being undergone by repeating the energy transfers. Since the 4f→5d transition in Eu^{2+} ions is allowed one, the transfer will mainly take place via a dipole-dipole interaction.

The critical distance, R_c, defined by Blasse32) is the distance between two luminescent centers, S (sensitizer) and A (activator), at which the probability of transfer from S to A is equal to the probability of radiative emission of S.

If we substitute in Eq. (1-4) $P_A=0.01$ (the usual value for 4f-5d transitions) and E=3.4 eV (the mean energy around the region in which the emission band overlaps with the reflection band) and we estimate the energy overlap at 1.0 eV^{-1} on α-$Sr_{0.99}Eu_{0.01}B_2O_4$ from Fig. 3

because the emission band completely overlaps with the reflection one, we find R_c=25 Å. Since the mean distance between the neighboring Eu^{2+} ions of EuB_2O_4 is 4.080 Å for six nearest neighbors and 6.632 Å for ten second-nearest neighbors, the probability of $Eu^{2+} \rightarrow Eu^{2+}$ energy transfer is very high and hence the emission from α-EuB_2O_4 should be very weak. For α-$Sr_{0.99}Eu_{0.01}B_2O_4$, the Eu^{2+} ions almost exist in two types of regions: the Eu^{2+} ions in the first type are dispersed by Sr^{2+} ions at the longer distance than at least 25 Å from the neighboring Eu^{2+} ions while the second type is the region of the cluster formed by a number of Eu^{2+} ions. The Eu^{2+} ions in the former region contribute as the luminescent center, but the concentration quenching effect in the cluster region is expected to be very strong. The energy-level diagram of Eu^{2+} ions in phases α and δ of SrB_2O_4:Eu^{2+} are illustrated in Fig. 13. The emission of α-SrB_2O_4:Eu^{2+} in which many Eu^{2+} ions

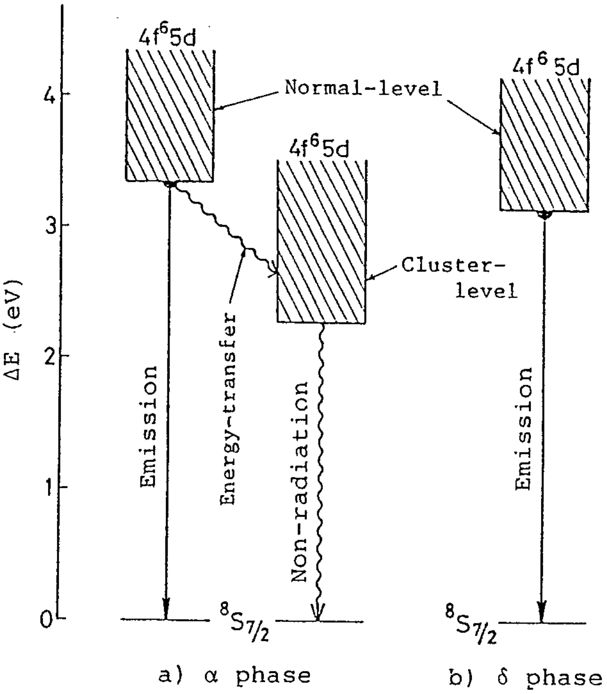

Figure 13. Proposed energy-level diagram of Eu^{2+} ions in phases α and δ of SrB_2O_4:Eu^{2+}. The narrow $4f^7$ level is represented with horizontal lines whereas the broad $4f^65d$ level corresponds to the hatched broad band. The black half-circles are levels of the luminescent center.

easily form the cluster should be weak. The energy transfer from Eu^{2+} in the former region to Eu^{2+} ions in the cluster region must not entirely contribute to the emission process.

If we substitute in Eq. (1-6) $V=6.589\times12.018\times4.337$ Å^3, N=4, and $R_c=25$ Å for α-$SrB_2O_4:Eu^{2+}$, we find $x_c\simeq0.01$. This value deviates from the observed one, $x_c\simeq0.04$ (see Fig. 5), and this fact must be due to the formation of clusters. The clusters contribute to decrease the calculated value owing to the increase of the overlap $\int f_{Eu}(E)F_{Eu}(E)dE$ between the emission and the reflection spectra while to increasing the observed value because Eu^{2+} ions are concentrated at the limited regions. Consequently, the true value must be $0.01<x_c<0.04$. The Eu^{2+} ions in γ-$SrB_2O_4:Eu^{2+}$, which also is the " open " structure, almost seem to behave as well as in α-$SrB_2O_4:Eu^{2+}$.

In phase δ of $SrB_2O_4:Eu^{2+}$, the such cluster region is scarcely formed and each Eu^{2+} ion is considerably isolated from the neighboring Eu^{2+} ions by the BO_4 units, and hence the possibility of $Eu^{2+}\rightarrow Eu^{2+}$ energy transfer must be lower than that of other phases. Consequently, the relative emission intensity of $SrB_2O_4:Eu^{2+}$ drastically increases with transformation into phase δ. This agrees with the fact that $SrB_4O_7:Eu^{2+}$, which consists of a three-dimensional $(B_4O_7)_\infty$ network of BO_4 tetrahedra in a similar manner as phase δ and in which the Eu^{2+} ions are completely surrounded by BO_4 units, gives a strong emission compares with other borates, viz., $Sr_3B_2O_6:Eu^{2+}$, $Sr_2B_2O_5:Eu^{2+}$, and α-$SrB_2O_4:Eu^{2+}$ as discussed in the previous chapter.

3-5. Summary

High-pressure syntheses and characterization by magnetic susceptibility and luminescent measurements were made on europium(II) metaborate, EuB_2O_4, and Eu^{2+}-activated alkaline earth metaborates, $SrB_2O_4:Eu^{2+}$ and $CaB_2O_4:Eu^{2+}$. The pressure-temperature phase diagram of EuB_2O_4 was determined by X-ray analysis. This diagram consists of the following four regions: the high-pressure phases of α, γ, and δ and the decomposed phase of $EuB_4O_7+Eu_2B_2O_5$. Phase δ-EuB_2O_4 was paramagnetic whereas other phases were antiferroagnetic. It was found that the high-pressure phases of EuB_2O_4, $SrB_2O_4:Eu^{2+}$, and $CaB_2O_4:Eu^{2+}$ gave the band emissions based on a $4f^7$-$4f^6 5d$ transition and the peak positions of their emissions shifted to long wavelength with transformation into the high-pressure phases. The emissions of EuB_2O_4 consist of a weak band at about 370 nm for phases α and γ, a band at about 410 nm for phase δ, and two bands at about 368 and 395 nm for the decomposed phase. Also their emission intensities drastically increased with changing from phase γ to δ; particularly, δ-$SrB_2O_4:Eu^{2+}$ was found to be an efficient photoluminescent material. The compound, $Sr_{0.99}Eu_{0.01}B_2O_4$, gives a strong emission at 395 nm, and its relative emission intensity (about 60 %) under an optimum (313 nm) excitation was about 100 times higher than that of phase α. These results were discussed by considering the relationship between their crystal structures and theories for the magnetic interactions and energy transfer phenomena.

The phase of β-$SrAl_4O_7$ was obtained by the hydrothermal preparation method under high-pressure conditions, and the structure was determined from three-dimensional X-ray diffraction data (R=0.047 for 324 observed reflections). The crystal lattice consists of a three-dimensional $(Al_4O_7)_\infty$ network of $Al(1)O_6$ octahedra and $Al(2)O_4$ and $Al(3)O_4$ tetrahedra, of which the Al-O bond lengths are 1.795 to 1.968 Å for the octahedra and 1.449 to 1.537 Å for the tetrahedra. These distances of AlO_4 units are considerably shorter than those in the other aluminates. Each Sr atom is surrounded by ten O atoms with interatomic distances from 2.503 to 2.664 Å

4. HIGH-PRESSURE SYNTHESIS AND PROPERTIES OF EUROPIUM(II) METASILICATE

4-1. Introduction

In the preceding chapter, the emission intensity of $SrB_2O_4:Eu^{2+}$ has been found to increase drastically when the host lattice transforms into a high-pressure phase (δ form). Alkaline earth metasilicates show various high-temperature and high-pressure polymorphisms.48) The calcium silicate, α- or β-$CaSiO_3$ (atmospheric pressure form) is transformed into δ-$CaSiO_3$ at about 30 kbar and 900°C, and ε-$CaSiO_3$ is obtained above 100 kbar at 1000°C.49) The structure of β-$CaSiO_3$ (low-temperature form) consists of $(SiO_3)_\infty$ chains of SiO_4 tetrahedra,50) while α-$CaSiO_3$ (high-temperature form) has been presumed to contain a $(Si_3O_9)^{6-}$ ring of three SiO_4 tetrahedra.51) Trojer52) has determined the structure of δ-$CaSiO_3$, of which the structural framework is the same $(Si_3O_9)^{6-}$ ring as in α-$CaSiO_3$. The ε phase crystallizes in the cubic system (perovskite type) and its structure is composed of a three-dimensional $(SiO_3)_\infty$ network of SiO_6 octahedra. The strontium metasilicate, α-$SrSiO_3$, also gives two high-pressure phases at 34-120 kbar and 750-1400°C53) but their structural analyses have not been performed.

The luminescent properties of Eu^{2+}-activated silicates in a system $M'O-SiO_2$ (M = Ca, Sr, and Ba) have been investigated by some workers,14) who have found that those silicates give band emissions colored with violet-blue to green. Among them, $M'_2SiO_4:Eu^{2+}$ is a green-emitting phosphor with high quantum efficiency, and $M'SiO_3:Eu^{2+}$ has been reported to show emissions varying from violet to green depending on the heating temperature of samples.14a)

If the above-mentioned high-pressure phases of $CaSiO_3:Eu^{2+}$ and $SrSiO_3:Eu^{2+}$ are obtained, they will show various luminescent properties. The silicate, α-$EuSiO_3$, also can be expected to transform such high-pressure forms as mentioned above. This chapter describes the high-pressure syntheses of $EuSiO_3$, $CaSiO_3:Eu^{2+}$, and $SrSiO_3:Eu^{2+}$, the luminescent properties of the resulting materials, and the crystal structures of α-, δ-, and δ′-$SrSiO_3$. Furthermore, the luminescent properties are discussed with regard to the X-ray structural analyses and IR spectra of the host lattices, the temperature dependences of the emission spectra, and experimental results of $CaSiO_3:Pb^{2+}$ and $SrSiO_3:Pb^{2+}$.

4-2. Experimental

<u>A. Sample preparation</u>. The atmospheric pressure phase, α-$EuSiO_3$, was obtained by heating a mixture of appropriate amounts of Eu_2O_3 (99.99 %), Si(99.999 %), and SiO_2 (99.999 %) at 1400°C for 3×2 h (two times) in Ar. The phosphors of α-$MSiO_3:Eu^{2+}$ (M=Ca and Sr) were prepared by the following standard ceramic technique: appropriate amounts of SiO_2 and $MCO_3:Eu^{3+}$, coprecipitated from a dilute HCl solution of luminescent grade MCO_3 and Eu_2O_3 by the slow addition of a $(NH_4)_2CO_3$ solution, were fully mixed, pelletized, and heated at 1300°C for 3 h in a reducing stream of H_2. The high-pressure treatments of samples were carried out with a cubic anvil type apparatus (∿60 kbar) and a split-sphere type apparatus (60-150 kbar).[54)] The powdered samples were packed into boron nitride cups (6 mm × 3.2 mm for the former apparatus or 3.5 mm × 4 mm for the latter one) and were heated by a graphite or a molybdenum heater. A Pt/Pt-13%Rh thermocouple was employed to measure the temperature of the sample. After maintaining the desired pressure and temperature, the samples were quenched to room temperature, and then the pressure was released.

Single crystals for the polymorphs of $SrSiO_3$ were grown from a mixture of polycrystalline α-$SrSiO_3$ containing KCl of a mol. ratio, $SrSiO_3$:KCl=10:1, as a flux. The samples were subjected to the appropriate pressure at 1300 or 1400°C for 60 min and then were allowed to cool to 800°C at a rate of 2°C/min. The applied pressures were 35, 40, and 55 kbar for α, δ, and δ′ phases, respectively. Transparent single crystals (∿0.3 mm long) were grown, the crystal habits of which were plates for the α and δ′ forms and needles for the δ one. For runs, in which samples containing the larger amount of KCl than the above-mentioned ratio of $SrSiO_3$:KCl were used, an unknown phase was formed as a by-product. The polycrystalline samples for the polymorphs of $SrSiO_3$ were obtained as follows: α-$SrSiO_3$ was prepared by heating stoichiometric mixture of $SrCO_3$ and SiO_2 at about 1300°C for 5×2 h (two times) in air, and δ- and δ′-$SrSiO_3$ were prepared from α-$SrSiO_3$ by treatments of 40 and 60 kbar at about 1000°C.

The atmospheric phases of Pb^{2+}-activated phosphors, α-$CaSiO_3$:Pb^{2+}, β-$CaSiO_3$:Pb^{2+}, and α-$SrSiO_3$:Pb^{2+}, were prepared by the following solid-state reactions: appropriate amounts of MCO_3, SiO_2, and PbO (99.9 %) were fully mixed, pelletized, and heated at various temperatures (1050-1100°C, β-$CaSiO_3$:Pb^{2+}; 1250-1350, α-$CaSiO_3$:Pb^{2+} and α-$SrSiO_3$:Pb^{2+}) for 3×2 h (two times) in Ar. The high-pressure treatments of α-$CaSiO_3$:Pb^{2+} and α-$SrSiO_3$:Pb^{2+} were carried out with the same apparatus as mentioned above.

B. Optical and magnetic susceptibility measurements. Ultraviolet luminescent spectra and magnetic susceptibilities of powdered samples were measured with a Shimadzu recording absolute spectrofluorophotometer and a Shimadzu MB-11 magnetic balance according to the techniques described in the previous chapter. The quantum efficiencies were estimated from the relative emission intensities taking into account the absorbances of the samples, which were determined by measurements of diffuse reflection spectra with a Shimadzu double-beam spectrophotometer UV-180 equipped with an attachment for an integrating sphere, using optical filters cutting the emissions of samples. The temperature dependences of luminescences were measured over the range between liquid N_2 temperature (77.4 K) and about 450 K in a stream of dry N_2 gas. The IR spectra of samples were obtained using the apparatus and method described in the first chapter.

C. X-ray measurements. Preliminary oscillation and Weissenberg photographs showed that the crystals of α-, δ-, and δ′-$SrSiO_3$ belong to the monoclinic system of C2, Cm, or C2/m (systematic absence: h+k=2n+1 for hkl reflections), the triclinic system of P1 or $P\bar{1}$, and the monoclinic system of $P2_1/c$ (systematic absences: l=2n+1 for h0l reflections and k=2n+1 for 0k0 reflections), respectively. Accurate cell parameters are presented in Table I. The intensity data were measured on a Rigaku automated four-circle diffractometer with graphite-monochromatized Mo Kα radiation according to the techniques as described previously. All possible reflections were collected up to the 2θ value of 60°. The observed reflections with $F_o>3\sigma_{F_o}$ (α-$SrSiO_3$, 730 reflections; δ-$SrSiO_3$, 1458 reflections; δ'-$SrSiO_3$, 914 reflections) were obtained, and were used for the latter calculations. The usual Lorentz and polarization corrections were applied, but the absorption and anomalous dispersion effects for heavy atoms were not considered.

D. Structure determinations and refinements. The structures of

Table I. Crystal data and X-ray measurements for the high-pressure polymorphs of $SrSiO_3$

	α form	δ form	δ' form
F.W.		163.70	
Symmetry	Monoclinic	Triclinic	Monoclinic
S.G.	C2	$P\bar{1}$	$P2_1/c$
a (Å)	12.323(5)	6.874(2)	7.452(4)
b (Å)	7.139(2)	6.894(2)	6.066(2)
c (Å)	10.873(5)	9.717(3)	13.479(7)
α (°)		85.01(3)	
β (°)	111.58(4)	110.57(3)	117.09(4)
γ (°)		104.01(2)	
V (Å^3)	889.5(6)	418.3(2)	542.5(4)
Dm (g/cm^3)	3.64	3.87	3.96
Dx (g/cm^3)	3.67	3.90	4.01
Z	12	6	8
λ (Å)		0.71069	
(Mo Kα) (mm^{-1})	17.83	18.95	19.48
F(000)	912	456	608
Cryst size (mm^3)	0.20×0.20 ×0.07	0.08×0.07 ×0.15	0.15×0.25 ×0.10

α-, δ-, and δ′-$SrSiO_3$ were solved by the direct method (MULTAN 78 program[55]) and were refined by the method of block-diagonal least-squares (HBLS-V program[22]). The final positional and thermal parameters along with their estimated standard deviations are listed in Tables II, III, and IV.

As the space group of α-$SrSiO_3$, C2 was adopted, and the atoms of Sr(1), Sr(2), and Sr(3) were found to occupy the general positions [site 4(c)]. The coordinates of the remaining atoms (Si and O) were determined from the difference Fourier maps. Among them, the coordinates of Si(1), Si(3), O(1), and O(6) could be located at the special sites 2(a) and 2(b) and those of the other atoms at general positions. Isotropic refinements for all atomic parameters gave R=0.053 and R_w= 0.082 for 730 observed reflections. The weighting scheme $w=(F_m/F_o)^2$ for $F_o>F_m$ (=30.0) and w=1.0 for $F_o \leq F_m$ (=30.0) was employed.

For the δ form, the space group of $P\bar{1}$ gave a satisfactory result and coordinates of Sr atoms could be determined as follows: Sr(1) at 0.75, 0.25, 0.00; Sr(2) at 0.26, 0.08, 0.65; Sr(3) at 0.11, 0.58, 0.35.

Table II. Final positional and thermal parameters for α-$SrSiO_3$, with their standard deviations in parentheses

Atom	x	y	z	B (Å^2)
Sr(1)	0.0873(11)	0	0.2494(9)	0.34(2)
Sr(2)	0.2455(16)	0.4780(19)	0.2458(18)	0.33(2)
Sr(3)	0.4128(11)	-0.0207(14)	0.2516(9)	0.42(2)
Si(1)	0	0.417(6)	0	0.34(7)
Si(2)	0.116(4)	0.790(5)	-0.001(4)	0.45(5)
Si(3)	0	1.075(7)	1/2	0.31(7)
Si(4)	0.130(4)	0.702(5)	0.498(3)	0.39(5)
O(1)	0	0.874(16)	0	0.28(18)
O(2)	0.042(12)	0.323(13)	0.139(10)	0.74(16)
O(3)	0.107(11)	0.532(14)	-0.009(9)	0.73(14)
O(4)	0.130(11)	0.842(12)	-0.142(11)	0.52(14)
O(5)	0.223(12)	0.835(14)	0.139(11)	0.90(17)
O(6)	0	0.605(16)	1/2	0.34(19)
O(7)	0.049(9)	1.185(13)	0.635(9)	0.69(15)
O(8)	0.110(11)	0.911(12)	0.511(9)	0.41(14)
O(9)	0.119(12)	0.659(14)	0.350(11)	1.12(16)
O(10)	0.213(9)	0.643(12)	0.630(9)	0.40(13)

Table III. Final positional and thermal parameters for δ-$SrSiO_3$, with their estimated standard deviations in parentheses

Atom	x	y	z	U_{11}[a]	U_{22}	U_{33}	U_{12}	U_{13}	U_{23}
Sr(1)	0.752(2)	0.250(1)	0.003(1)	458(22)	274(17)	235(17)	-42(15)	111(16)	25(14)
Sr(2)	0.262(2)	0.079(2)	0.652(1)	641(24)	515(21)	308(20)	349(20)	101(17)	98(16)
Sr(3)	0.110(2)	0.578(2)	0.348(1)	880(27)	449(20)	316(20)	403(19)	337(18)	244(16)

Atom	x	y	z	B (Å^2)	Atom	x	y	z	B (Å^2)
Si(1)	0.600(5)	0.391(5)	0.291(5)	0.91(6)	O(4)	0.473(12)	0.386(11)	0.129(11)	0.87(16)
Si(2)	0.256(4)	0.250(4)	0.012(4)	0.40(5)	O(5)	0.094(11)	0.377(10)	-0.079(10)	0.54(14)
Si(3)	0.253(5)	0.056(4)	0.290(5)	0.78(6)	O(6)	0.366(10)	0.131(10)	-0.082(10)	0.45(14)
O(1)	0.759(10)	0.258(10)	0.266(10)	0.44(14)	O(7)	0.173(11)	0.090(10)	0.127(11)	0.71(15)
O(2)	0.439(10)	0.247(9)	0.384(9)	0.24(13)	O(8)	0.371(11)	-0.112(10)	0.269(10)	0.68(15)
O(3)	0.757(11)	0.563(10)	0.388(10)	0.61(15)	O(9)	0.122(11)	-0.053(10)	0.389(10)	0.58(15)

[a] The form of the anisotropic thermal parameter ($\times 10^4$) is $\exp[-2\pi^2(U_{11}h^2a^{*2} + U_{22}k^2b^{*2} + U_{33}l^2c^{*2} + 2U_{12}hka^*b^* + 2U_{13}hla^*c^* + 2U_{23}klb^*c^*)]$.

Table IV. Final positional and thermal parameters for δ'-SrSiO$_3$, with their estimated standard deviations in parentheses

Atom	x	y	z	U_{11}[a]	U_{22}	U_{33}	U_{12}	U_{13}	U_{23}
Sr(1)	0.2567(10)	0.0897(9)	0.3404(10)	94(5)	39(4)	79(5)	1(4)	59(4)	7(4)
Sr(2)	0.2147(10)	0.8983(10)	0.6261(9)	77(4)	41(4)	65(5)	-3(4)	42(4)	2(4)

Atom	x	y	z	B ($\mathring{A}^2$)	Atom	x	y	z	B ($\mathring{A}^2$)
Si(1)	0.158(3)	0.590(3)	0.408(3)	0.37(4)	O(3)	0.054(8)	0.829(8)	0.400(8)	0.37(11)
Si(2)	0.451(3)	0.353(3)	0.617(3)	0.31(4)	O(4)	0.314(9)	0.561(8)	0.539(9)	0.71(12)
O(1)	0.311(8)	0.590(9)	0.346(8)	0.50(10)	O(5)	0.433(8)	0.328(8)	0.733(8)	0.46(11)
O(2)	0.005(8)	0.386(8)	0.351(9)	0.48(10)	O(6)	0.400(8)	0.127(8)	0.548(8)	0.49(11)

[a] The form of the anisotropic thermal parameter ($\times 10^4$) is $\exp[-2\pi^2(U_{11}h^2a^{*2} + U_{22}k^2b^{*2} + U_{33}l^2c^{*2} + 2U_{12}hka^*b^* + 2U_{13}hla^*c^* + 2U_{23}klb^*c^*)]$.

The remaining atoms (Si and O) were located on the successive Fourier maps. Several cycles of the refinement with anisothermal parameters for Sr atoms gave conventional R and R_w values of 0.043 and 0.077. The weighting scheme of F_m=20.0 was used.

The Sr atoms of δ-$SrSiO_3$ were located at 0.26, 0.09, 0.24 for Sr(1) and 0.21, 0.90, 0.63 for Sr(2), and the coordinates of Si and O atoms were determined from the difference Fourier maps. All of these atoms occupy general positions [site 4(e)] of space group $P2_1/c$. The values of R and R_w were finally converged to 0.046 and 0.050 by the anisotropic refinements for Sr atoms. The same weighting scheme (F_m=30.0) as α-$SrSiO_3$ was used for the refinement. The atomic scattering factors used in all the calculations were taken from International Tables for X-ray Crystallography.$^{24)}$

4-3. Results

A. $EuSiO_3$. Under pressures of 60 and 70 kbar at 1000-1400°C, α-$EuSiO_3$ transformed into two high-pressure phases, which were termed in a similar manner as calcium and strontium analogs, viz., δ- and δ′-$EuSiO_3$. This polymorphism is the same as that shown in $SrSiO_3$.

The magnetic properties of the resulting materials are summarized in Table V. Since the effective magnetic moments, μ_{eff}, are in good agreement with the theoretical value (7.94 μ_B), the ions of Eu in the samples can be considered to be mainly in the divalent state. The

Table V. Magnetic data for the high-pressure polymorphs of $EuSiO_3$

Phase	Treatment		$\mu_{eff}(\mu_B)$	θ_c(K)
	P (kbar)	T (°C)		
α	—	—	7.95	-1
δ	60	1000	7.72	-3
δ′	70	1200	7.83	-3

paramagnetic Curie temperature is about -1 K for α-$EuSiO_3$ and about -3 K for δ- and δ′-$EuSiO_3$. This indicates that these samples are paramagnetic down to low temperatures, and thus the magnetic interactions between the neighboring Eu^{2+} ions are weak.

B. Crystal structures of α-, δ-, and δ′-$SrSiO_3$. The interatomic distances and angles in α-$SrSiO_3$ are summarized in Table VI. The projections of the α-$SrSiO_3$ structure viewed along the b and c axes are shown in Figs. 1 and 2. The structure consists of Sr atoms and $(Si_3O_9)^{6-}$ rings, which are alternately pseudohexagonally packed along the direction perpendicular to (001). Because of this arrangement, the symmetry of α-$SrSiO_3$ has been reported to be pseudohexagonal. There are two kinds of $(Si_3O_9)^{6-}$ rings, one type comprising one $Si(1)O_4$ and two $Si(2)O_4$ tetrahedra and the other one $Si(3)O_4$ and two $Si(4)O_4$ tetrahedra with shared O atoms. The atoms Si(1), Si(3), O(1), and O(6) are located on twofold axes parallel to the b axis, and the centers of gravity for those $(Si_3O_9)^{6-}$ rings also lie on these axes. Consequently, the $(Si_3O_9)^{6-}$ rings should show twofold rotation symmetry. The Si-O bond lengths of the SiO_4 tetrahedra vary from 1.48 to 1.85 Å and O-Si-O angles [96.7(6)-133.9(8)°] considerably deviate from the value for a regular tetrahedron (109.47°).

Atoms of Sr occupy the sites Sr(1), Sr(2), and Sr(3). Each Sr atom is surrounded by eight O atoms, with Sr-O distances from 2.39 to 2.83 Å, to form an SrO_8 dodecahedron. The polyhedra $Sr(1)O_8$, $Sr(2)O_8$, and $Sr(3)O_8$ are alternately connected with one another to form layers of SrO_8 on planes (004) and (00$\bar{4}$). The crystal lattice is a three-dimensional arrangement of these layers linked together with the $(Si_3O_9)^{6-}$ rings by the O atoms.

The interatomic distances and angles in δ-$SrSiO_3$ are listed in Table VII, and the projection of its structure is shown in Fig. 3. The atomic parameters of δ-$SrSiO_3$ (Table III) almost agree with those of δ-$CaSiO_3$ reported by Trojer,[52] where the a, b, and c axes of δ-$CaSiO_3$ correspond to the -a, c, and b axes of δ-$SrSiO_3$, and hence the δ forms of $SrSiO_3$ and $CaSiO_3$ are isostructural. The structure of δ-$SrSiO_3$ consists of the same $(Si_3O_9)^{6-}$ rings as do the α forms of

Table VI. Interatomic distances (Å) and angles (°) in α-$SrSiO_3$, with their estimated standard deviations in parentheses

(a) The Si_3O_9 rings

Si(1)-tetrahedron

Si(1) -O(2)	1.56(1)(×2)	O(2)-Si(1)-O(2^{i})	129.0(8)
-O(3)	1.59(2)(×2)	O(2)-Si(1)-O(3)	107.2(8)(×2)
Average	1.58	O(2)-Si(1)-O(3^{i})	98.6(8)(×2)
		O(3)-Si(1)-O(3^{i})	117.7(8)
		Average	109.7

Si(2)-tetrahedron

Si(2) -O(1)	1.55(2)	O(1)-Si(2)-O(3)	110.2(8)
-O(3)	1.85(2)	O(1)-Si(2)-O(4)	109.3(8)
-O(4)	1.65(1)	O(1)-Si(2)-O(5)	110.2(8)
-O(5)	1.64(2)	O(3)-Si(2)-O(4)	101.9(7)
Average	1.67	O(3)-Si(2)-O(5)	104.7(7)
		O(4)-Si(2)-O(5)	119.8(7)
		Average	109.4

Si(3)-tetrahedron

Si(3) -O(7)	1.58(1)(×2)	O(7)-Si(3)-O(7^{i})	120.2(8)
-O(8)	1.76(1)(×2)	O(7)-Si(3)-O(8)	104.3(7)(×2)
Average	1.67	O(7)-Si(3)-O(8^{i})	114.6(7)(×2)
		O(8)-Si(3)-O(8^{i})	96.7(6)
		Average	109.1

Si(4)-tetrahedron

Si(4) -O(6)	1.75(2)	O(6)-Si(4)-O(8)	101.9(7)
-O(8)	1.53(1)	O(6)-Si(4)-O(9)	101.4(8)
-O(9)	1.60(2)	O(6)-Si(4)-O(10)	100.6(8)
-O(10)	1.48(1)	O(8)-Si(4)-O(9)	109.0(7)
Average	1.59	O(8)-Si(4)-O(10)	105.4(7)
		O(9)-Si(4)-O(10)	133.9(8)
		Average	108.7

(b) Sr-O distances

Sr(1)-dodecahedron

Sr(1) -O(1)	2.68(2)	Sr(1) -O(7^{i})	2.78(1)
-O(2)	2.57(1)	-O(8)	2.83(1)
-O(4^{i})	2.74(1)	-O(9)	2.64(1)
-O(5^{i})	2.67(1)	-O(10^{iii})	2.54(1)
		Average	2.68

Sr(2)-dodecahedron

Sr(2) -O(2)	2.59(1)	Sr(2) -O(7^{i})	2.80(1)
-O(3)	2.69(1)	-O(8^{iii})	2.63(1)
-O(4^{ii})	2.42(1)	-O(9)	2.59(1)
-O(5)	2.77(1)	-O(10^{iii})	2.70(1)
		Average	2.65

Sr(3)-dodecahedron

Sr(3) -O(2^{ii})	2.59(1)	Sr(3) -O(6^{ii})	2.67(2)
-O(3^{iii})	2.59(1)	-O(7^{iii})	2.39(1)
-O(4^{i})	2.82(1)	-O(9^{ii})	2.69(1)
-O(5)	2.43(1)	-O(10^{ii})	2.63(1)
		Average	2.60

Symmetry code: O(n^{i})($\bar{x}$, y, $\bar{z}$), O(n^{ii})(1/2+x, 1/2+y, z), O(n^{iii})(1/2-x, 1/2+y, $\bar{z}$).

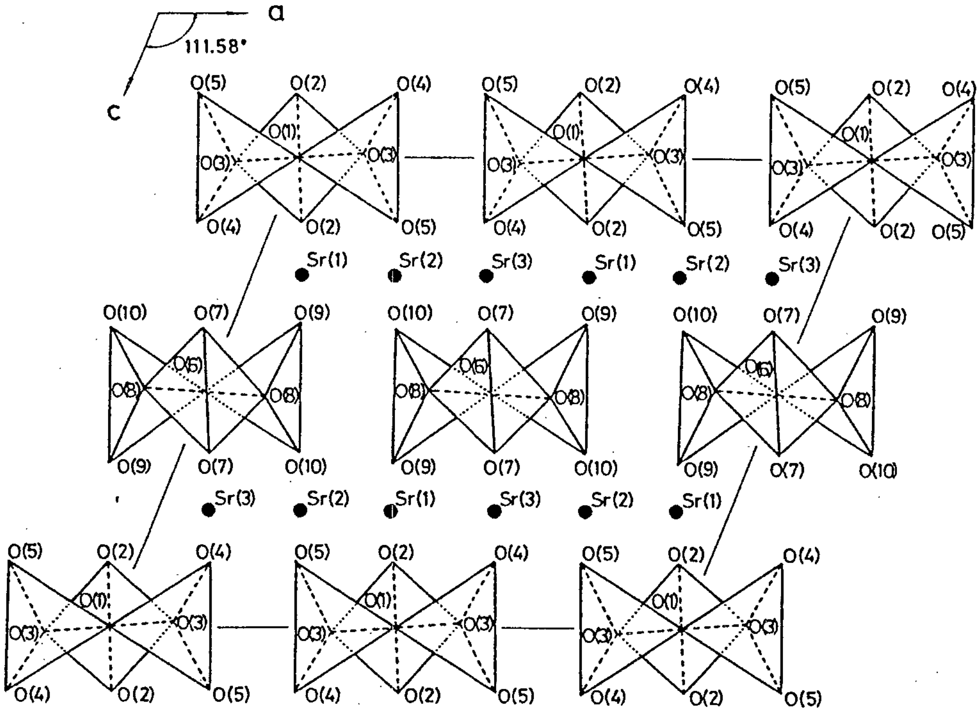

Figure 1. A projection of the α-SrSiO$_3$ structure viewed along the b axis.

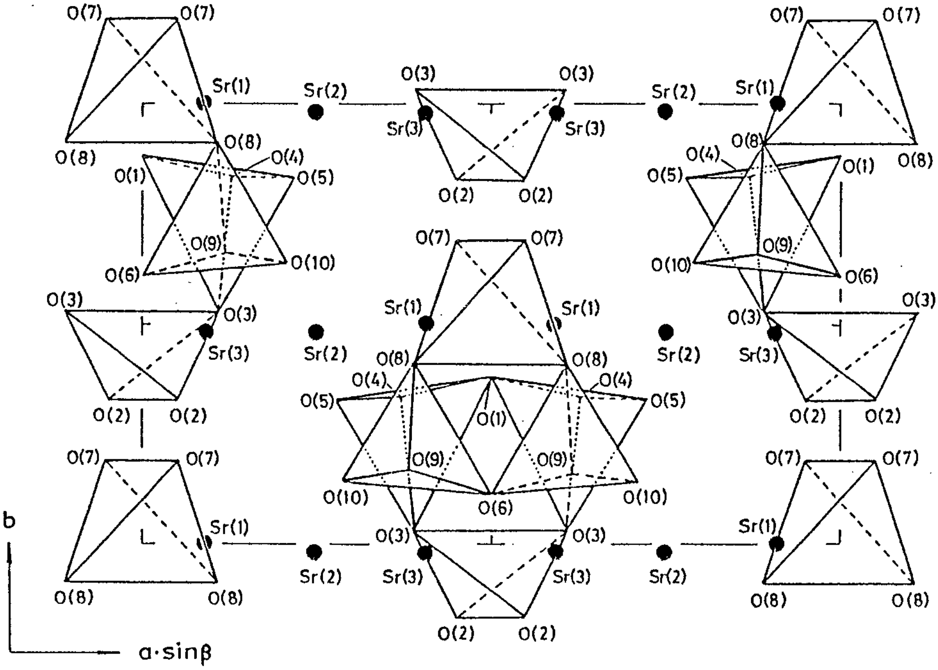

Figure 2. A projection of the α-SrSiO$_3$ structure viewed along the c axis.

Table VII. Interatomic distances (Å) and angles (°) in δ-$SrSiO_3$, with their estimated standard deviations in parentheses

(a) The Si_3O_9 Ring

Si(1)-Tetrahedron

Si(1) -O(1)	1.68(1)	O(1)-Si(1)-O(2)	109.7(6)
Si(1) -O(2)	1.74(1)	O(1)-Si(1)-O(3)	103.2(6)
Si(1) -O(3)	1.52(1)	O(1)-Si(1)-O(4)	91.6(7)
Si(1) -O(4)	1.51(1)	O(2)-Si(1)-O(3)	110.0(6)
average	1.61	O(2)-Si(1)-O(4)	108.7(6)
		O(3)-Si(1)-O(4)	130.4(7)
		average	109.0

Si(2)-Tetrahedron

Si(2) -O(4)	1.65(1)	O(4)-Si(2)-O(5)	112.6(7)
Si(2) -O(5)	1.56(1)	O(4)-Si(2)-O(6)	105.8(6)
Si(2) -O(6)	1.59(1)	O(4)-Si(2)-O(7)	99.8(6)
Si(2) -O(7)	1.65(1)	O(5)-Si(2)-O(6)	115.2(6)
average	1.61	O(5)-Si(2)-O(7)	114.5(6)
		O(6)-Si(2)-O(7)	107.5(6)
		average	109.2

Si(3)-Tetrahedron

Si(3) -O(2)	1.67(1)	O(2)-Si(3)-O(7)	113.9(9)
Si(3) -O(7)	1.50(1)	O(2)-Si(3)-O(8)	108.4(6)
Si(3) -O(8)	1.63(1)	O(2)-Si(3)-O(9)	108.7(6)
Si(3) -O(9)	1.57(1)	O(7)-Si(3)-O(8)	90.6(6)
average	1.59	O(7)-Si(3)-O(9)	127.9(7)
		O(8)-Si(3)-O(9)	103.2(6)
		average	108.8

(b) Sr-O Distances

Sr(1)-Polyhedron

Sr(1) -O(1)	2.55(1)	Sr(1) -O(6)	2.61(1)
Sr(1) -O(4)	2.96(1)	Sr(1) -O(6^{i})	2.66(1)
Sr(1) -O(5)	2.67(1)	Sr(1) -O(7i)	2.98(1)
Sr(1) -O(5^{i})	2.60(1)	Sr(1) -O(8i)	2.66(1)
		average	2.71

Sr(2)-Polyhedron

Sr(2) -O(1^{i})	2.38(1)	Sr(2) -O(8^{i})	2.33(1)
Sr(2) -O(3^{i})	2.49(1)	Sr(2) -O(9)	2.56(1)
Sr(2) -O(6)	2.48(1)	Sr(2) -O(9^{i})	2.48(1)
		average	2.45

Sr(3)-Polyhedron

Sr(3) -O(1)	2.78(1)	Sr(3) -O(5^{i})	2.53(1)
Sr(3) -O(3)	2.56(1)	Sr(3) -O(8)	2.69(1)
Sr(3) -O(3^{i})	2.59(1)	Sr(3) -O(9)	2.58(1)
		average	2.62

[a] Symmetry transformations: O(n^{i}), ($\bar{x}$, $\bar{y}$, $\bar{z}$).

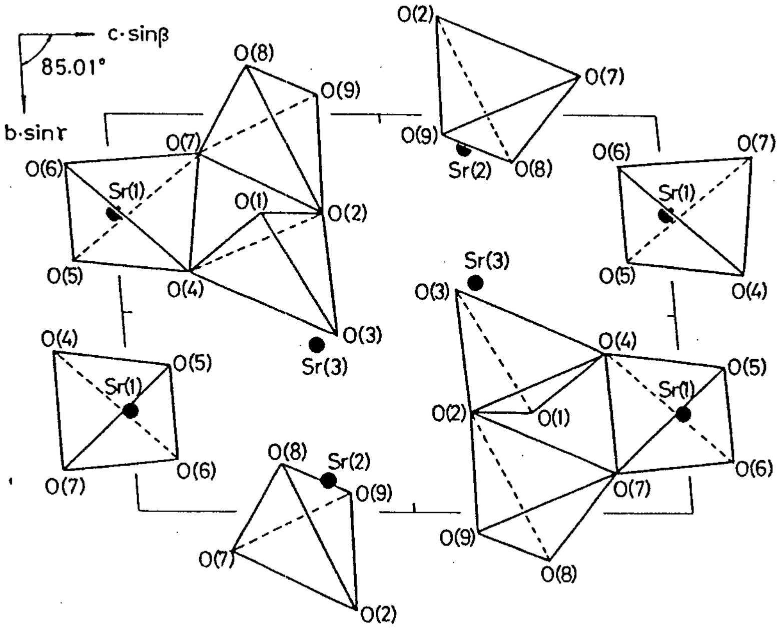

Figure 3. A projection of the δ-$SrSiO_3$ structure viewed along the a axis.

$CaSiO_3$ and $SrSiO_3$. The $(Si_3O_9)^{6-}$ ring is constructed of three distorted tetrahedra of $Si(1)O_4$, $Si(2)O_4$, and $Si(3)O_4$ by sharing the cornered oxygens, O(2), O(4), and O(7). Their Si–O bond lengths and angles vary from 1.50 to 1.74 Å and from 90.6 to 130.4°, respectively. Each Sr atom is surrounded by six or eight oxygens with Sr–O distances of 2.33 to 2.98 Å.

The interatomic distances and angles in δ'-$SrSiO_3$ are presented in Table VIII, and the projection viewed along the b axis is illustrated in Fig. 4. This silicate contains a four-membered $(Si_4O_{12})^{8-}$ ring, in which four tetrahedra are condensed by sharing O(1) and O(4) atoms. The $(Si_4O_{12})^{8-}$ ring has Si–O bond lengths ranging from 1.602 to 1.693 Å, O–Si–O bond angles from 103.1 to 116.0°, and an inversion center. Such four-membered rings have been found to be contained in complex silicates, but not in the other metasilicates except for δ'-$SrSiO_3$.56) The Sr atoms occupy the eightfold sites with the Sr–O distances varying from 2.409 to 3.058 Å. The structure of δ'-$SrSiO_3$ is constructed of Sr atoms and $(Si_4O_{12})^{8-}$ rings by packing along the b axis.

Table VIII. Interatomic distances (Å) and angles (°) in δ′-$SrSiO_3$, with their estimated standard deviations in parentheses

(a) The Si_4O_{12} Ring

Si(1)-Tetrahedron

Si(1) -O(1)	1.693(9)	O(1)-Si(1)-O(2)	104.6(5)
Si(1) -O(2)	1.620(9)	O(1)-Si(1)-O(3)	112.1(5)
Si(1) -O(3)	1.624(9)	O(1)-Si(1)-O(4)	103.1(5)
Si(1) -O(4)	1.622(9)	O(2)-Si(1)-O(3)	116.0(5)
average	1.640	O(2)-Si(1)-O(4)	115.7(5)
		O(3)-Si(1)-O(4)	104.6(5)
		average	109.4

Si(2)-Tetrahedron

Si(2) -O(1)	1.646(9)	O(1)-Si(2)-O(4)	107.4(5)
Si(2) -O(4)	1.662(9)	O(1)-Si(2)-O(5)	106.0(5)
Si(2) -O(5)	1.636(9)	O(1)-Si(2)-O(6)	107.1(5)
Si(2) -O(6)	1.602(9)	O(4)-Si(2)-O(5)	112.4(5)
average	1.637	O(4)-Si(2)-O(6)	111.6(5)
		O(5)-Si(2)-O(6)	112.0(5)
		average	109.4

(b) Sr-O Distances

Sr(1)-Polyhedron

Sr(1) -O(1)	3.058(9)	Sr(1) -O(3)	2.556(8)
	3.054(9)	Sr(1) -O(5^{iii})	2.409(9)
Sr(1) -O(2)	2.648(9)	Sr(1) -O(6)	2.510(8)
Sr(1) -O(2^{ii})	2.721(9)	Sr(1) -O(6^{i})	2.652(8)
		average	2.701

Sr(2)-Polyhedron

Sr(2) -O(1^{iii})	2.714(9)	Sr(2) -O(4)	2.627(9)
Sr(2) -O(2^{i})	2.492(9)	Sr(2) -O(5)	3.063(9)
Sr(2) -O(3)	2.752(8)	Sr(2) -O(5^{ii})	2.478(9)
Sr(2) -O(3^{i})	2.496(8)	Sr(2) -O(6)	2.503(8)
		average	2.641

[a] Symmetry transformations: Sr(n^{i}) and O(n^{i}), ($\bar{x}$, $\bar{y}$, $\bar{z}$); Sr(n^{ii}) and O(n^{ii}), ($\bar{x}$, 1/2+y, 1/2-z); Sr(n^{iii}) and O(n^{iii}), (x, 1/2-y, 1/2+z).

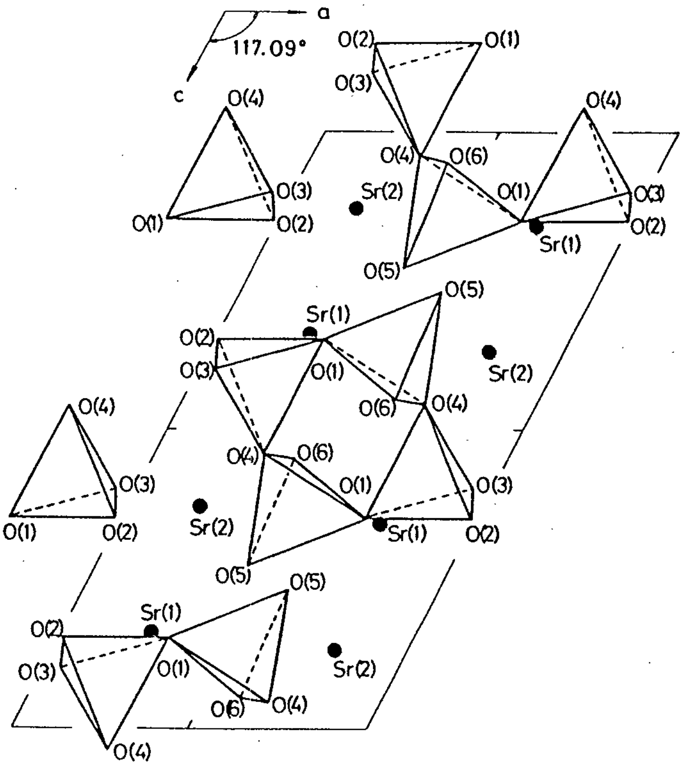

Figure 4. A projection of the δ'-$SrSiO_3$ structure viewed along the b axis.

C. High-pressure polymorphism of $SrSiO_3$ and $EuSiO_3$. The lattice parameters for the high-pressure phases of $CaSiO_3$, $SrSiO_3$, and $EuSiO_3$ are summarized in Table IX. The behavior for the phase transformation of $CaSiO_3$ differs somewhat from the cases of $SrSiO_3$ and $EuSiO_3$. Two phases α- and δ-$CaSiO_3$ correspond to the α and δ forms of $SrSiO_3$ and $EuSiO_3$, but the δ' form is a phase which has not been observed in $CaSiO_3$. Since the ionic radii of Sr^{2+} and Eu^{2+} are almost equal to each other (see ref. 57), both of $SrSiO_3$ and $EuSiO_3$ can be seen to show the same high-pressure polymorphism.

D. Luminescent spectra of $CaSiO_3{:}Eu^{2+}$ and $SrSiO_3{:}Eu^{2+}$. A series of high-pressure phases of $CaSiO_3{:}Eu^{2+}$ and $SrSiO_3{:}Eu^{2+}$ except for ε-$CaSiO_3{:}Eu^{2+}$ were obtained by treatments at 35-100 kbar and 800-1400°C. All of the obtained samples showed band emissions assigned to the

Table IX. Lattice parameters for the high-pressure polymorphs of $MSiO_3$ (M=Ca, Sr, and Eu)

Compound	α form	δ form	δ′ form	ε form
$CaSiO_3$[a]	a= 6.90 Å b=11.78 c=19.65 α= 90.0° β= 90.8 γ= 90.0	a= 6.695(5) Å b= 9.257(7) c= 6.666(6) α= 86.63(5)° β= 76.13(5) γ= 70.38(5)		a= 3.485(8) Å
$SrSiO_3$	a=12.323(5) Å b= 7.139(2) c=10.873(5) β=111.58(4)°	a= 6.874(2) Å b= 6.894(2) c= 9.717(3) α= 85.01(3)° β=110.57(3) γ=104.01(2)	a= 7.452(4) Å b= 6.066(2) c=13.479(7) β=117.09(4)°	
$EuSiO_3$	a=12.337(6) Å b= 7.141(3) c=10.894(6) β=111.58(4)°	a= 6.877(3) Å b= 6.898(3) c= 9.727(5) α= 85.01(4)° β=110.58(4) γ=104.00(4)	a= 7.455(6) Å b= 6.074(4) c=13.513(10) β=117.19(6)°	

[a] See refs. 46-49.

$4f^7$-$4f^65d$ transitions of Eu^{2+} ions, and their luminescent properties considerably varied with the phase transformations. The emission and excitation spectra of $CaSiO_3$:Eu^{2+}(1 at%) and $SrSiO_3$:Eu^{2+}(1 at%) are shown in Figs. 5 and 6, and the luminescent data are summarized in Table X.

The peak positions for the emission bands of the samples shift to short wavelength when the host lattices transform into high-pressure forms, δ-$CaSiO_3$ and δ′-$SrSiO_3$. The emission bands are centered at the following positions: 507 nm (green), α-$CaSiO_3$:Eu^{2+}; 472 nm (blue), δ-$CaSiO_3$:Eu^{2+}; 498 nm (green), α-$SrSiO_3$:Eu^{2+}; 503 nm (green), δ-$SrSiO_3$:Eu^{2+}; 466 nm (blue), δ′-$SrSiO_3$:Eu^{2+}.

The excitation spectral patterns of samples consist of a band peaking at 311 or 323 nm for α-$CaSiO_3$:Eu^{2+} or α-$SrSiO_3$:Eu^{2+}, two bands peaking at 257 and 356 nm for δ-$SrSiO_3$:Eu^{2+}, and three bands peaking at 248, 312, and 335 nm or 250, 314, and 350 nm for δ-$CaSiO_3$:Eu^{2+} or δ′-$SrSiO_3$:Eu^{2+}. For the compounds containing Eu^{2+} ions, the absorptions in the near-ultraviolet region are attributable to the 4f→5d transitions of Eu^{2+} ions. Therefore, the absorption (reflection) spectral patterns of the samples are generally compatible with their excita-

Table X. Luminescent data for the high-pressure polymorphs of $CaSiO_3$:Eu^{2+}(1 at%) and $SrSiO_3$:Eu^{2+}(1 at%)

Phase	Treatment P (kbar)	Treatment T (°C)	λ_{max}(nm)	λ/2 (nm)	Q.E.(%)[a]	T_{50}(K)[b]
α-$CaSiO_3$			507	70–80	≃1	420
δ-$CaSiO_3$	45	1000	472	83	22	420
α-$SrSiO_3$			498	75–80	<1	380
δ-$SrSiO_3$	35	1000	503	63	6	300
δ′-$SrSiO_3$	60	1000	466	58	37	360

[a] Q.E. = quantum efficiency under an optimum excitation at 300 K.

[b] T_{50} = quenching temperature at which the intensity of the luminescence is half of that at 77.4 K.

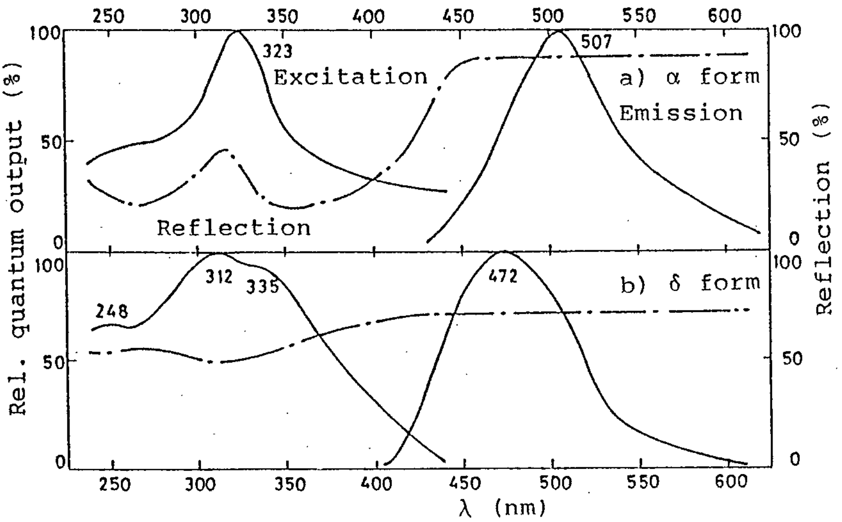

Figure 5. Relative emission and excitation spectra (solid line), and diffuse reflection spectra (dashed-dotted line) for α- and δ-$CaSiO_3:Eu^{2+}$(1 at%).

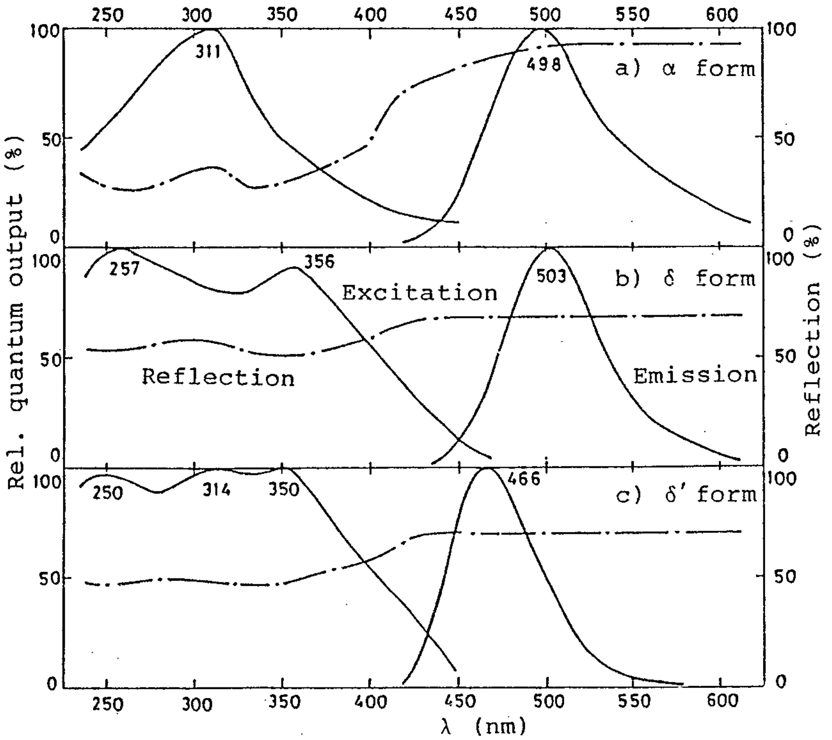

Figure 6. Relative emission and excitation spectra (solid line), and diffuse reflection spectra (dashed-dotted line) for the high-pressure polymorphs of $SrSiO_3:Eu^{2+}$(1 at%).

tion spectral patterns. The reflection spectra for δ-$CaSiO_3$:Eu^{2+}, δ-$SrSiO_3$:Eu^{2+}, and δ′-$SrSiO_3$:Eu^{2+} can be seen from Figs. 3 and 4 to correspond to the excitation spectra, but the excitation spectral patterns of α-$CaSiO_3$:Eu^{2+} and α-$SrSiO_3$:Eu^{2+} are not compatible with the reflection spectral patterns which consist of two absorption bands around 270 and 350 nm. From this observation, we can presume that there are two kinds of Eu^{2+} ions in α-$CaSiO_3$:Eu^{2+} and α-$SrSiO_3$:Eu^{2+}, that is, one acts as the luminescent center but the other does not contribute to the luminescence. If most of the Eu^{2+} ions in the samples belong to the latter type, we should observe only absorption (reflection) patterns for this type of Eu^{2+} ions. The small amount of Eu^{2+} ions must be classified as the former type and contribute to the luminescence but not to the overall observable absorption spectrum.

The emission intensities (quantum efficiencies) of $CaSiO_3$:Eu^{2+} and $SrSiO_3$:Eu^{2+} also were found to increase appreciably to 20-40 times with shifts for the peak positions of the emission bands when the host lattices transform into δ-$CaSiO_3$ and δ′-$SrSiO_3$. While the quantum efficiencies of α phases are very weak (Q.E.≃1 %), their high-pressure phases give relatively high quantum efficiency values (under optimum Eu^{2+} concentrations and excitations): 22 %, δ-$CaSiO_3$:Eu^{2+}; 7 %, δ-$SrSiO_3$:Eu^{2+}; 37 %, δ′-$SrSiO_3$:Eu^{2+}. The concentration dependences for quantum efficiencies of samples are summarized in Figs. 7 and 8. The optimum concentration of Eu^{2+} ions for the luminescence is around 1-2 at% for α-$CaSiO_3$:Eu^{2+}, 1 at% for δ-$CaSiO_3$:Eu^{2+}, 2 at% for α-$SrSiO_3$:Eu^{2+}, 4 at% for δ-$SrSiO_3$:Eu^{2+}, and 1 at% for δ′-$SrSiO_3$:Eu^{2+}, respectively.

The temperature dependences for the emission intensities of the samples are shown in Figs. 9 and 10. The light output at 77.4 K was adopted as a standard for the temperature dependence of each sample. The quenching curves of α-$CaSiO_3$:Eu^{2+} and δ-$CaSiO_3$:Eu^{2+} can be seen to be closely similar to each other, and both of these phases give T_{50}= 420 K (Table X). The shape for the quenching curve of α-$SrSiO_3$:Eu^{2+} differs from that of δ- and δ′-$SrSiO_3$:Eu^{2+}. The T_{50} values are 380, 300, and 360 K for the α, δ, and δ′ forms, respectively. However, the data of the α form seem to be unreliable because its emission intensity

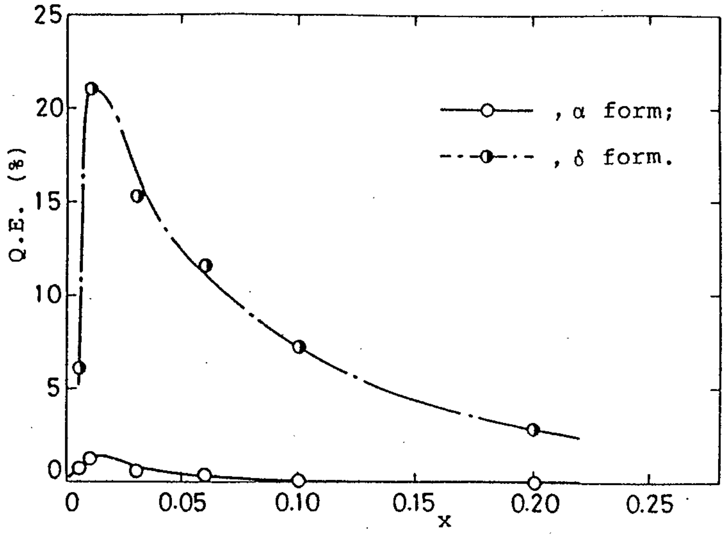

Figure 7. Quantum efficiency vs. Eu^{2+} content (x) for the α and δ phases of $Ca_{1-x}Eu_xSiO_3$.

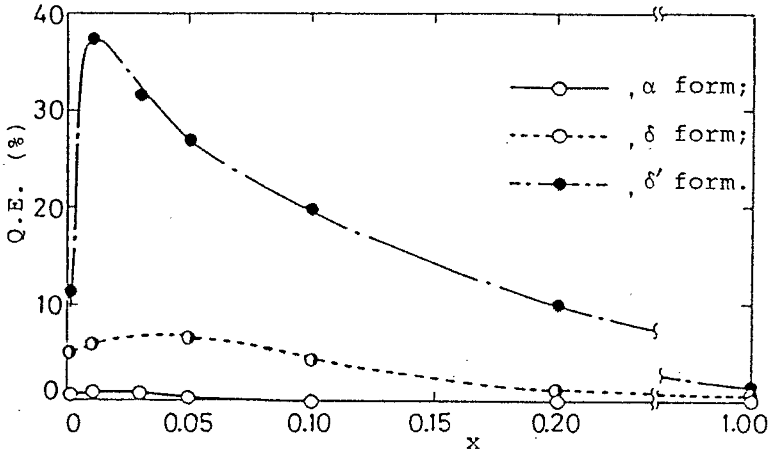

Figure 8. Quantum efficiency vs. Eu^{2+} content (x) for the high-pressure polymorphs of $Sr_{1-x}Eu_xSiO_3$.

is weak.

Ringwood and Major[58)] have pointed out that the perovskite modification of $CaSiO_3$ (ε form) is obtained under pressures exceeding 100 kbar, but on the release of pressure, it retrogressively transformed either to glass, ε-$CaSiO_3$, or mixtures of these phases. For $CaSiO_3$: Eu^{2+}, however, instead of ε-$CaSiO_3$ or the vitreous phase which are

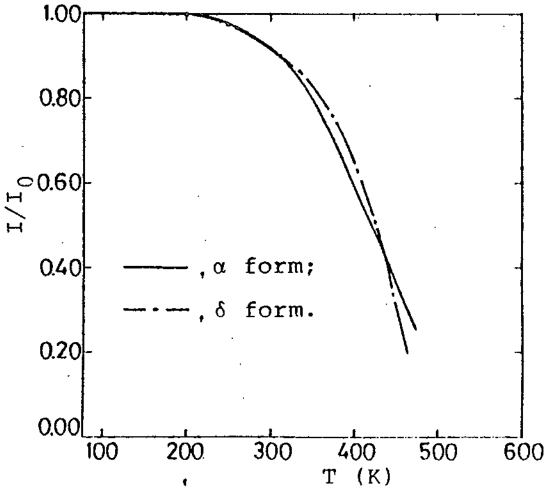

Figure 9. Temperature dependences of the light outputs for the α and δ phases of $CaSiO_3:Eu^{2+}$ (1 at%).

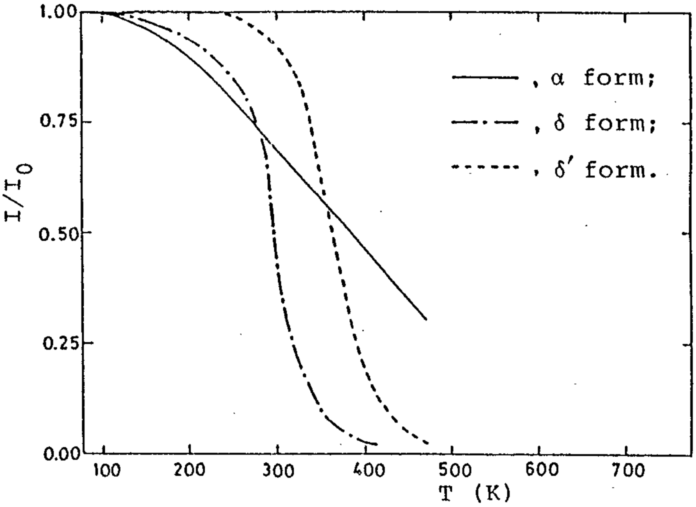

Figure 10. Temperature dependences of the light outputs for the high-pressure polymorphs of $SrSiO_3:Eu^{2+}$(1 at%).

are expected to be obtained by the treatments of α-$CaSiO_3:Eu^{2+}$ at 150 kbar and 1000°C, an unknown phase was obtained. Its X-ray powder diffraction data are presented together with the data of ε-$CaSiO_3$ in Table XI.

The stability for perovskite type structure of ABO_3 oxides (A, large cation; B, small cation) can be estimated from the tolelance factor t. In Table XII, the t values for the some silicates $MSiO_3$ (M=Ca,

Table XI. X-ray powder diffraction data for $CaSiO_3:Eu^{2+}$(1 at%) and ε-$CaSiO_3$

$CaSiO_3:Eu^{2+}$		ε-$CaSiO_3$[a]	
$d_{obs.}$ (Å)	I/I_0	$d_{obs.}$ (Å)	I/I_0
3.03	100	2.467	100
2.92	75	2.009	60
2.79	95	1.742	80
2.75	65	1.570	5
2.69	35	1.427	60
2.61	50	1.229	50
2.52	55		
2.44	50		
2.40	30		
2.28	30		
2.19	55		
2.12	30		
2.04	35		
2.02	25		
1.98	50		
1.89	20		
1.63	30		
1.60	30		

[a] Ref. 49b.

Sr, and Eu) are summarized. When the value of t is between 0.89 and 1.00, in general, the cubic perovskite modification is formed. All of $CaSiO_3$, $SrSiO_3$, and $EuSiO_3$ give larger values of t than 1.00. It is impossible for those silicates that the perovskite modification is obtained. From the experimental results,⁴⁹⁾ however, $CaSiO_3$ whose t value is the smallest among them has been found to be barely trans-

Table XII. Tolerance factors for perovskite modifications of $MSiO_3$ (M=Ca, Sr, and Eu)

Compound	t[a]
$CaSiO_3$	1.08
$SrSiO_3$	1.12
$EuSiO_3$	1.11

[a] $t=\frac{r_A+r_B}{\sqrt{2}(r_B+r_X)}$, where the value of r_A, r_B, and r_X represent the ionic radii of M^{2+}, Si^{4+}, and O^{2-}, of which the values are given in ref. 57.

formed into the ε form by the treatments at very high pressures, but, from their large values of t, both $SrSiO_3$ and $EuSiO_3$ cannot be expected to give the ε phase. Therefore, the experimental observation that the perovskite modification of $CaSiO_3:Eu^{2+}$ has not been obtained by the treatment at 150 kbar must be responsible for the large Eu^{2+} ions in the matrix of $CaSiO_3$.

4-4. Discussion

Since the absorption (excitation) spectra of Eu^{2+}-activated phosphors are attributable to the 4f→5d transitions of Eu^{2+} ions, their spectral patterns reflect splittings of 5d levels by the crystal fields. The Eu^{2+} ions in $CaSiO_3:Eu^{2+}$ and $SrSiO_3:Eu^{2+}$ phosphors occupy the sites of Ca^{2+} and Sr^{2+} ions. In Fig. 11, we illustrate the oxygen arrangements around the Eu^{2+} ions in $SrSiO_3:Eu^{2+}$ polymorphs. The α and δ phases of $CaSiO_3$ or $SrSiO_3$ are approximately or entirely isostructural with the corresponding analogues, and hence the anion environments of the Eu^{2+} ions in $CaSiO_3:Eu^{2+}$ are closely similar to those in $SrSiO_3:Eu^{2+}$. The symmetries of these polyhedra are very low (point group C1), although the EuO_8 polyhedra in α-$SrSiO_3:Eu^{2+}$ have a symmetry similar to that of a polyhedron with point group Ci. It may be difficult, therefore, to assign exactly the excitation spectral patterns on the basis of the splittings of 5d levels by the crystal fields.

The Eu^{2+} ions in δ'-$SrSiO_3:Eu^{2+}$, which are surrounded by eight oxygens, give an excitation spectrum consisting of three bands (Fig. 6). This observation means that the $Eu(1)O_8$ and $Eu(2)O_8$ polyhedra shown in Fig. 11 form the crystal field by which the 5d level is split into three levels.

For the α phases of $CaSiO_3:Eu^{2+}$ and $SrSiO_3:Eu^{2+}$, the Eu^{2+} ions occupy the eightfold sites to form similar EuO_8 polyhedra to those in δ'-$SrSiO_3:Eu^{2+}$. Thus these phosphors can also be expected to give the same crystal fields around Eu^{2+} ions as δ'-$SrSiO_3:Eu^{2+}$. However, the estimated excitation spectral profile agrees with the reflection spectra, but not with their excitation spectra. It is concluded that

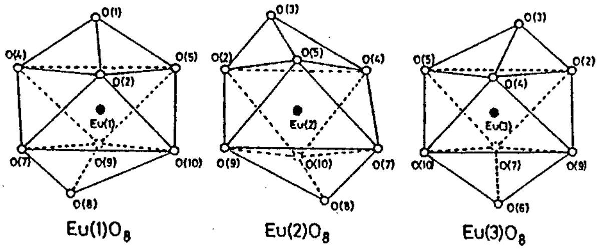

a) α form

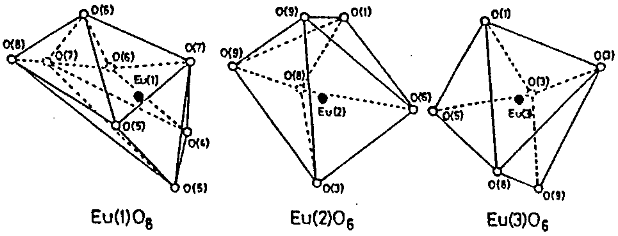

b) δ form

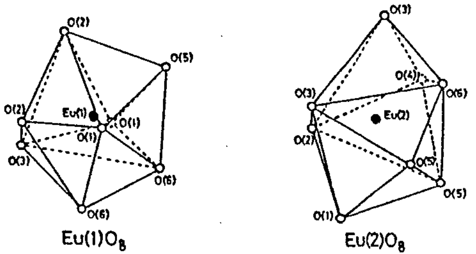

c) δ′ form

Figure 11. Schematic illustrations of the EuO_n polyhedra in the high-pressure polymorphs of $SrSiO_3:Eu^{2+}$ phosphors.

the Eu^{2+} ions placed on the eightfold sites in α-$CaSiO_3$ and α-$SrSiO_3$ cannot give the luminescence and contribute only to the absorption in the near-ultraviolet region. The Eu^{2+} ions responsible for the luminescent centers must be located on positions difficult from the above-mentioned eightfold sites, e.g., grain boundaries or vitreous regions in the matrix.

For δ-$SrSiO_3:Eu^{2+}$, the Eu^{2+} ions are surrounded by six or eight oxygens to form $Eu(1)O_8$, $Eu(2)O_6$, and $Eu(3)O_6$ polyhedra. Among them, the EuO_6 octahedra give a different crystal field from that of EuO_8 polyhedra, by which the 5d level of Eu^{2+} ion is split into two levels of e_g and t_{2g}, roughly speaking, because the symmetries of the $Eu(2)O_6$ and $Eu(3)O_6$ octahedra are similar to that of the regular octahedron.

As two-third of the Eu^{2+} ions statistically occupy the sixfold sites of Sr(2) and Sr(3) atoms in δ-$SrSiO_3$, this phosphor apparently gives the excitation spectrum of two bands peaking at 257 and 356 nm.

The δ phase of $CaSiO_3$:Eu^{2+}, which is isostructural with δ-$SrSiO_3$:Eu^{2+}, is expected to give an excitation spectrum with two maxima, but its spectral pattern consists of three bands like that of δ′-$SrSiO_3$:Eu^{2+}. This can be interpreted from the difference in the ionic radii of Ca^{2+}, Sr^{2+}, and Eu^{2+}. The ionic radius of Eu^{2+} is almost equal to that of Sr^{2+}, but it is larger than that of Ca^{2+}. Thus the Eu-O and Sr-O distances should be long compared with the Ca-O length. The mean Ca-O and Sr-O distances in $CaSiO_3$ and $SrSiO_3$ polymorphs are presented in Table XIII. For δ-$CaSiO_3$, the Ca-O length of the Ca(1) site (2.630 Å) is longer than those of Ca(2) and Ca(3) sites, and is comparable to the normal Sr-O or Eu-O distance (2.60-2.70 Å). In δ-$CaSiO_3$:Eu^{2+}, consequently, most of the Eu^{2+} ions are located on the eightfold site of Ca(1) atom rather than the sixfold sites of Ca(2) and Ca(3) atoms, and hence this phosphor must give the same excitation spectral pattern as δ′-$SrSiO_3$:Eu^{2+}.

The peak positions for emission bands of Eu^{2+}-activated phosphors also depend on the arrangements of the anions around Eu^{2+} ions, the electronegativity of anions, etc. Both δ-$CaSiO_3$:Eu^{2+} and δ′-$SrSiO_3$:Eu^{2+}, in which the Eu^{2+} ions must occupy the eightfold sites with the similar Eu-O distances to each other, show the same emissions around 470 nm, whereas the Eu^{2+} ions placed on the eightfold and sixfold sites in δ-$SrSiO_3$:Eu^{2+} give the emission band peaking at about 510 nm.

It is noticeable that the quantum efficiencies of $CaSiO_3$:Eu^{2+} and $SrSiO_3$:Eu^{2+} appreciably increase when the host lattices transform into the high-pressure phases. Since the constituent chemical species of the samples are unchangeable throughout the phase transformations, the differences in their quantum efficiencies are qualitatively interpreted by considering the crystal structures.

Repeats of the energy transfers via Coulomb and exchange interactions between neighboring Eu^{2+} ions are pointed out as one of the quenching effects on Eu^{2+}-activated phosphors. The critical distance

Table XIII. Oxygen arrangements around Sr atoms in the high-pressure polymorphs of $CaSiO_3$ and $SrSiO_3$

Phase	Site	C.N.[a]	Mean M-O dist.(Å)
α-$CaSiO_3$[b]	Ca	8	——
δ-$CaSiO_3$[c]	Ca(1)	8	2.630
	Ca(2)	6	2.467
	Ca(3)	6	2.375
α-$SrSiO_3$	Sr(1)	8	2.68
	Sr(2)	8	2.65
	Sr(3)	8	2.60
δ-$SrSiO_3$	Sr(1)	8	2.71
	Sr(2)	6	2.45
	Sr(3)	6	2.62
δ'-$SrSiO_3$	Sr(1)	8	2.701
	Sr(2)	8	2.641

[a] C.N. = Ca or Sr coordination number to oxygen.

[b] The detailed structural analysis of this form has not been performed.

[c] Ref. 52.

R_c for most of them is 20-25 Å for the Coulomb interaction and 4-5 Å for the exchange interaction, where R_c represents the distance between the luminescent centers, S (sensitizer) and A (activator) at which the probability of transfer from S to A is equal to the probability of radiative emission of S. The Eu^{2+} ions in Eu^{2+}-activated phosphors act as both S and A. The magnitudes of the above-mentioned interactions can be estimated from the proportion of overlap between the absorption (reflection) and emission bands, and depend on the number of neighboring Eu^{2+} ions and their interatomic distances. The distances between the neighboring sites which can be occupied by the Eu^{2+} ions in $SrSiO_3$: Eu^{2+} polymorphs are summarized in Table XIV. The mean distances are 3.85-4.12 Å for the nearest Eu neighbors and 4.24-5.08 Å for the second-nearest Eu neighbors, respectively. These distances suffice for the energy transfer.

Table XIV. Interatomic distances between the Eu neighbors in the high-pressure polymorphs of $SrSiO_3:Eu^{2+}$

Phase	Site	Mean Eu-Eu dist.(Å)[a]	
		nn	nnn
α-$SrSiO_3$	Eu(1)	4.12(×6)	5.08(×2)
	Eu(2)	4.12(×6)	5.07(×2)
	Eu(3)	4.12(×6)	5.04(×2)
δ-$SrSiO_3$	Eu(1)	3.89(×4)	4.24(×2)
	Eu(2)	3.88(×3)	4.41(×2)
	Eu(3)	3.85(×4)	4.41(×2)
δ′-$SrSiO_3$	Eu(1)	4.03(×6)	4.62(×1)
	Eu(2)	3.92(×6)	5.05(×1)

[a] nn and nnn represent the nearest and second-nearest Eu neighbors, respectively.

From the reflection spectral measurements of the samples (Figs. 5 and 6), generally speaking, the overlaps between the reflection and emission bands are small. Thus, energy transfers between the neighboring Eu^{2+} ions do not occur so often. However, α-$CaSiO_3:Eu^{2+}$ or α-$SrSiO_3:Eu^{2+}$ has a great absorption band at 320-450 nm, and consequently, if the Eu^{2+} ions which occupy the eightfold sites give the emission around 470 nm like δ-$CaSiO_3:Eu^{2+}$ or δ′-$SrSiO_3:Eu^{2+}$, the overlaps between their absorption and emission spectra will be great. This assumption sufficiently suggests that no luminescence is caused by the Eu^{2+} ions placed on the eightfold sites, and emission spectra (507 and 498 nm) which hardly overlap with the absorption bands are observable.

On the basis of the measurements of quenching temperature, we can estimate the effect of lattice vibrations on the luminescence. It is noticeable that the T_{50} value of δ′-$SrSiO_3:Eu^{2+}$ (ca. 360 K) is higher than that of δ-$SrSiO_3:Eu^{2+}$ (ca. 300 K). This means that, in δ′-$SrSiO_3:Eu^{2+}$, the quenching effect caused by the lattice vibration is to be smaller than that in the δ form.

The silicate anions can be regarded as mainly taking part in the lattice vibration of samples. The silicate anions in $SrSiO_3$ polymorphs

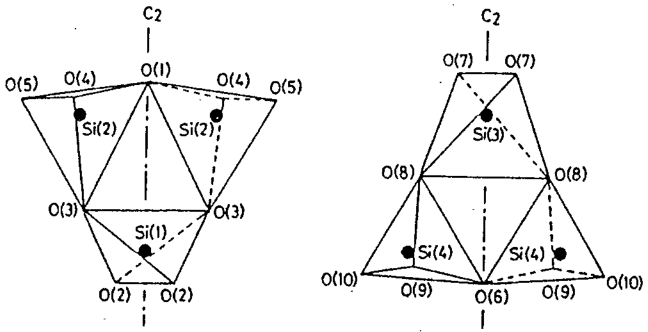

a) α form

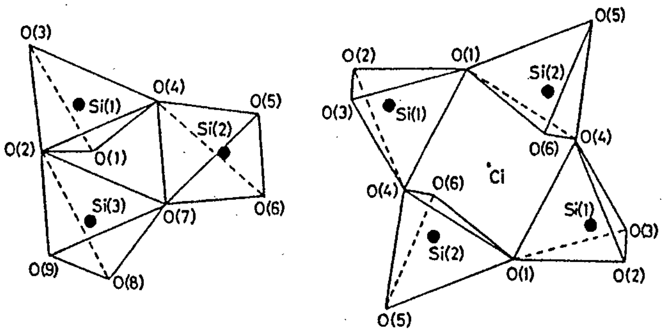

b) δ form

c) δ′ form

Figure 12. Illustrations of the silicate anions in the high-pressure polymorphs of $SrSiO_3$.

are illustrated in Fig. 12. The $(Si_3O_9)^{6-}$ rings of the α form show the symmetry of twofold rotation around an axis of Si(1)-O(1) or Si(3) -O(6) and the $(Si_4O_{12})^{8-}$ rings have inversion centers, but no symmetry element can be found out about the $(Si_3O_9)^{6-}$ rings of the δ form. Their point groups are C2 (pseudo D3h), C1, and Ci for the α, δ, and δ′ forms, respectively. Consequently, the IR spectral patterns of $CaSiO_3$ and $SrSiO_3$ polymorphs are expected to be very complex.

For an isolated tetrahedral SiO_4 anions with a symmetry Td, there are four fundamental modes of vibrations, viz., a normally inactive symmetric strech (800 cm^{-1}), an inactive doubly degenerate bend (500 cm^{-1}), a strongly active triply degenerate stretch (1050 cm^{-1}), and another active bending mode (625 cm^{-1}).$^{59)}$ When the SiO_4 units are connected with one another by sharing oxygens, the symmetric stretch of SiO_4 unit becomes an infrared active mode.

The IR spectra for the high-pressure polymorphs of $CaSiO_3$ and $SrSiO_3$ are shown in Figs. 13 and 14. In Table XV, their spectral patterns are interpreted according to the assignments of some silicates attempted by Lazarev and co-workers.60) These metasilicates give strong absorptions over three regions around ∿580, 615-750, and 815-1070 cm^{-1}. The absorption bands of 815-1070 cm^{-1} are derives from $\nu_{as}(O^-SiO^-)$, $\nu_{as}(SiOSi)$, and $\nu_s(O^-SiO^-)$, where ν_{as} and ν_s correspond to the antisymmetric and symmetric stretching modes of SiO_4 unit, and $\nu(O^-SiO^-)$ and $\nu(SiOSi)$ represent the Si-O bonds of oxygens non-shared and shared with the other SiO_4 units, respectively. The bands below 580 cm^{-1} are responsible for the Si-O bending and Ca-O or Sr-O stretching modes. The group of bands in the regions of 615-750 cm^{-1} corresponds to the mode originated from the $\nu_s(SiOSi)$, which has been suggested to be a characteristic mode of the silicates containing cyclic anions by some workers.61) From the absorption bands around 615-750 cm^{-1}, consequently, we can obtain informations for the ring structures of silicate anions in the high-pressure polymorphs of $CaSiO_3$ and $SrSiO_3$.

The IR spectral patterns of δ-$CaSiO_3$ and δ-$SrSiO_3$, of which the crystal structures have been found to be entirely isostructural from the previous X-ray analyses, are closely similar to each other. For the α form, however, the spectral profile around 615-750 cm^{-1} for $CaSiO_3$ somewhat differs from that of $SrSiO_3$. The former silicates consists of three bands: 616, 653, and 717 cm^{-1} whereas two bands: 622 and 705 cm^{-1} are observed on the latter silicate. This suggests that the shapes of $(Si_3O_9)^{6-}$ rings in α-$CaSiO_3$ and α-$SrSiO_3$ are similar but their symmeries are distinct from each other. The symmetries of crystal structures are generally higher than those of structure elements, e.g., silicate anions, in crystal lattices. From Table XV, the symmetry for the $(Si_3O_9)^{6-}$ ring in α-$CaSiO_3$ is expected to be low compared with that for α-$SrSiO_3$, and possibly the silicate anion in α-$CaSiO_3$ does not show the symmetry of twofold rotation. This must be confirmed if the detailed structural analysis of α-$CaSiO_3$ is performed.

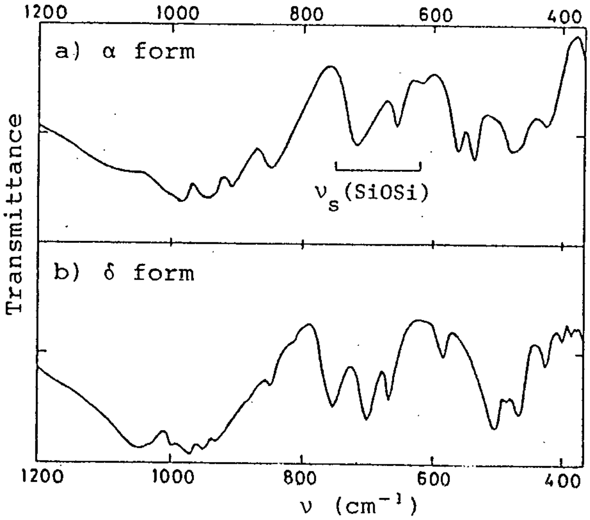

Figure 13. IR spectra for the high-pressure polymorphs of $CaSiO_3$.

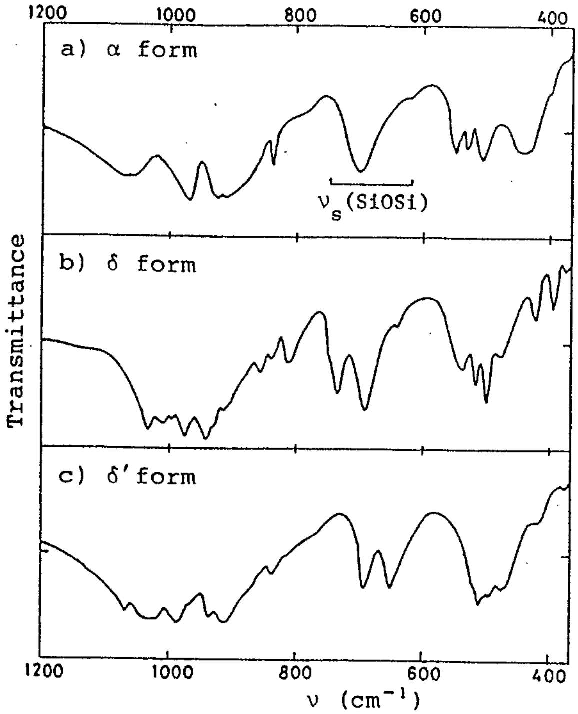

Figure 14. IR spectra for the high-pressure polymorphs of $SrSiO_3$.

For the δ′ form, the IR spectral profile responsible for the mode of ν_s(SiOSi) consists of two strong bands at about 648 and 690 cm^{-1}, which shift to longer wavenumber compared with the main absorption bands of α- or δ-$SrSiO_3$. This observation suggests that the ring of

Table XV. IR spectra (cm^{-1})[a] for the high-pressure polymorphs of $MSiO_3$ (M=Ca and Sr)

Mode	$CaSiO_3$		$SrSiO_3$		
	α	δ	α	δ^{-}	δ'
	1050 m	1046 vs	1067 s	1033 vs	1067 s
$\nu_{as}(O^-SiO^-)$	1003 s	1031 s	1053 s	1007 s	1025 vsb
	985 vs	1004 s	970 vs	997 s	985 vs
	948 vs	994 s	925 vs	976 vs	968 s
$\nu_{as}(SiOSi)$	940 vs	972 vs	910 vsb	943 vs	938 vs
	906 s	949 vs	840 m	929 s	910 vsb
$\nu_s(O^-SiO^-)$	846 s	933 s		915 s	840 w
		882 w		858 m	816 vw
		847 w		842 w	
		817 w		816 m	
	717 s	753 s	705 vsb	749 m	690 s
$\nu_s(SiOSi)$	653 m	700 vs	622 vw	734 vs	648
	616 w	666 s		692 vs	
				643 w	
Si–O bending and M–O stretching vibrations	560 s	581 m	549 m	535 m	526 m
	538 vs	509 vs	529 m	519 s	511 vs
	474 sb	484 m	504 s	502 vs	505 s
	421 w	466 s	436 sb	485 s	495 s
		425 m		480 s	474 s
		400 w		476 s	470 s
				421 m	417 vw
				395 m	

[a] The characters of absorption bands are represented as follows: v, very; s, strong; m, medium; w, weak; b, broad.

$(Si_4O_{12})^{8-}$ anion is less flexible than that of the $(Si_3O_9)^{6-}$ anion in α- or δ-$SrSiO_3$. The $(Si_4O_{12})^{8-}$ ring in the δ′ form must be hard to vibrate compared with the $(Si_3O_9)^{6-}$ ring in the δ form. Therefore, δ′-$SrSiO_3$:Eu^{2+}, which consists of the rigid $(Si_4O_{12})^{8-}$ rings, give the relatively strong emission.

The Eu^{2+} ions in δ-$CaSiO_3$:Eu^{2+} must selectively occupy the eightfold sites rather than another sites. As the dispersion of the Eu^{2+} ions in the matrix is expected to be good, the quenching effect of the energy transfer seems to be smaller than that of δ-$SrSiO_3$:Eu^{2+}. The great T_{50} value (ca. 420 K) indicates that the quenching effect of lattice vibration is relatively small. We can interpret from these considerations that δ-$CaSiO_3$:Eu^{2+} gives strong emission similar to δ′-$SrSiO_3$:Eu^{2+} in spite of the crystallographic mismatch between Ca^{2+} and Eu^{2+} ions.

The same results as described above have been observed on the high-pressure polymorphs of $CaSiO_3$:Pb^{2+} and $SrSiO_3$:Pb^{2+}. The relative emission and excitation spectra for $CaSiO_3$:Pb^{2+} and $SrSiO_3$:Pb^{2+} polymorphs are shown in Figs. 15 and 16. These luminescent properties are presented in Table XVI. Among the atmospheric phases of $CaSiO_3$:Pb^{2+} and $SrSiO_3$:Pb^{2+}, the β form shows a violet emission and is an efficient material with the bright luminescence under 253.7 nm excitation because its excitation spectrum peaks at about 257 nm. For α-$SrSiO_3$:Pb^{2+}, however, the emission spectra colored with light-blue are broad and weak, and furthermore, the excitation spectra peak around 230 nm. Therefore, their luminescences are not sensitive to the 253.7 nm excitation. These observations agree with the results reported by Froelich and Fonda.[62)]

By high-pressure treatments of α-$CaSiO_3$:Pb^{2+} and α-$SrSiO_3$:Pb^{2+}, their resulting materials were found to give the luminescences sensitive to the 253.7 nm excitation. A high-pressure phase, δ-$CaSiO_3$:Pb^{2+}, shows a strong violet emission (ca. 341 nm) with a half-width of 37 nm as well as that of β-$CaSiO_3$:Pb^{2+}. The excitation spectrum consists of a band peaking at about 244 nm, and hence δ-$CaSiO_3$:Pb^{2+} may be also useful for an ultraviolet-exciting phosphor. Similarly, δ- and δ′-

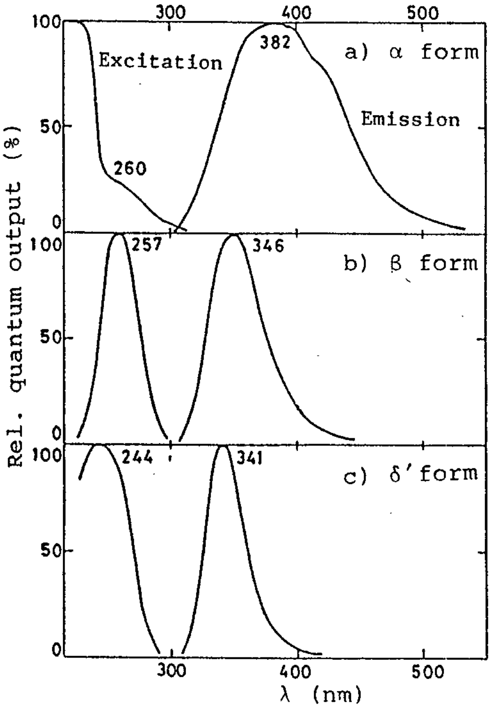

Figure 15. Relative emission and excitation spectra for the polymorphs of $CaSiO_3:Pb^{2+}$ (5 at%).

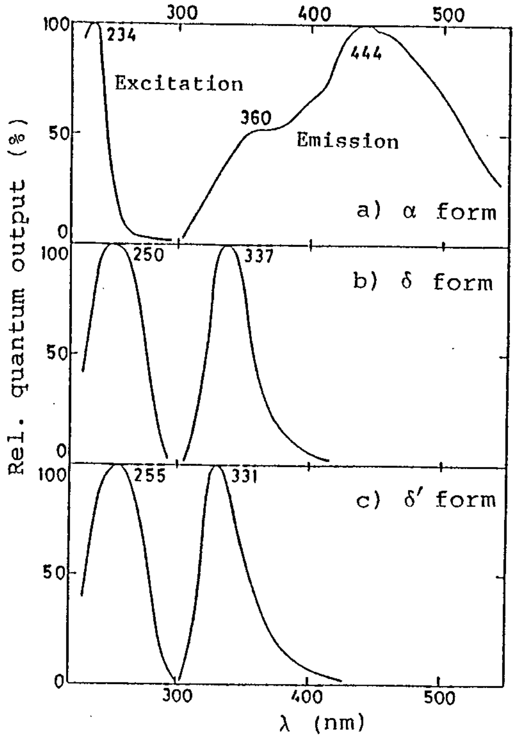

Figure 16. Relative emission and excitation spectra for the polymorphs of $SrSiO_3:Pb^{2+}$ (5 at%).

$SrSiO_3:Pb^{2+}$ give violet emissions peaking at about 337 and 331 nm, and the peak positions of those excitation spectra are around 250 and 255 nm. It was found that the emission intensity of $SrSiO_3:Pb^{2+}$ drastically increased when the host lattice (α form) transformed into the δ and δ′ forms. The ionic radii of Ca^{2+}, Sr^{2+}, and Pb^{2+} are summarized in Table XVII. The ionic radius of Pb^{2+} is considerably larger than that of Ca^{2+}. In β- or δ-$CaSiO_3$, the Ca^{2+} ions occupy two kinds of sites, especially a third of them occupy seven- or eight-coordinated sites. Consequently, the large Pb^{2+} ions in the β and δ forms are expected to be selectively located at those large sites.

The luminescent properties of β-$Ca_{1-x}Eu_xSiO_3$ ($0.01 \le x \le 0.20$) are given in Table XVIII. The emission band of sample shifted to longer wavelength and broadened with increasing the content of Pb^{2+} ions. For the samples with $x \ge 0.07$, the emission spectra were found to consist of

Table XVI. Luminescent properties for the polymorphs of $CaSiO_3:Pb^{2+}$(5 at%) and $SrSiO_3:Pb^{2+}$(5 at%)

Phase	λ_{max}(nm)	$\lambda/2$ (nm)	I (%)[a]	T_{50}(K)
α-$CaSiO_3$	light-blue	broad	6	
β-$CaSiO_3$	346	45	32	430
δ-$CaSiO_3$	341	37	26	440
α-$SrSiO_3$	light-blue	broad	weak	
δ-$SrSiO_3$	337	37	11	330
δ'-$SrSiO_3$	331	37	6	320

[a] I = relative intensity estimated by integrating the corresponding area below the emission curve obtained under 254 nm excitation at 300 K, where the intensity of $CaWO_4:Pb^{2+}$ (NBS 1026) is defined as 100 %.

two bands and the concetration quenching effect on luminescence was observed. Possibly the Pb^{2+} ions at seven-coordinated sites give the emission band at shorter wavelength, while another band may be responsible for the Pb^{2+} ions at six-coordinated sites. This suggests that the Pb^{2+} ions in the β or δ form which must be selectively located at the large sites are effectively dispersed in the matrix, and hence the interactions between the neighboring Pb^{2+} ions must be relatively small. Therefore, β- and δ-

Table XVII. Ionic radii (Å)[a] for some divalent-metal cations

Ion	VI[b]	VIII[b]
Ca^{2+}	1.00	1.12
Sr^{2+}	1.18	1.26
Pb^{2+}	1.19	1.29

[a] Ref. 57)

[b] These values represent the coordination numbers to oxygen.

Table XVIII. Luminescent properties for β-$Ca_{1-x}Pb_xSiO_3$

Pb^{2+} content (x)	λ_{max}(nm)	λ/2 (nm)	I (%)[a]
0.01	336	33	21
0.03	337	34	31
0.05	346	45	32
0.07	348,355	54	29
0.10	349,356	54	24
0.20	350,359	55	16

[a] Excitation at 254 nm and 300 K.

$CaSiO_3:Pb^{2+}$ give the strong emissions compared with α-$CaSiO_3:Pb^{2+}$, in which the Pb^{2+} ions arbitrarily occupy only the eight-coordinated sites in the matrix. In a similar manner as $CaSiO_3:Pb^{2+}$, δ-$SrSiO_3$ which is isostructural with δ-$CaSiO_3$ has two kinds of sites for Pb^{2+} ions may be effectively dispersed compared with those occupying the eightfold sites in α- and δ'-$SrSiO_3:Pb^{2+}$. However, this dispersion effect of Pb^{2+} ions in δ'-$SrSiO_3:Pb^{2+}$ is small because the difference between the ionic radii of Sr^{2+} and Pb^{2+} is small (see Table XVII).

The temperature dependences for the luminescences of $CaSiO_3:Pb^{2+}$ and $SrSiO_3:Pb^{2+}$ are shown in Fig. 17. The light output at 77.4 K was adopted as a standard for the temperature dependences of the sample. The quenching temperatures of α-$CaSiO_3:Pb^{2+}$ and α-$SrSiO_3:Pb^{2+}$ could not reproducibly be measured because their luminescences were weak. From the quenching curves, the temperatures required to quench the luminescences of β- and δ-$CaSiO_3:Pb^{2+}$ can be seen to be high compared with those of δ- and δ'-$SrSiO_3:Pb^{2+}$, and their T_{50} values are 320-440 K (see Table XVI). This result suggests that the quenching effect caused by the lattice vibrations in β- and δ-$CaSiO_3:Pb^{2+}$ are smaller than the corresponding effect in δ- and δ'-$SrSiO_3:Pb^{2+}$, and that the emission intensities of the former materials are strong compared with those of the latter materials. The phase, δ'-$SrSiO_3:Pb^{2+}$, which has the same

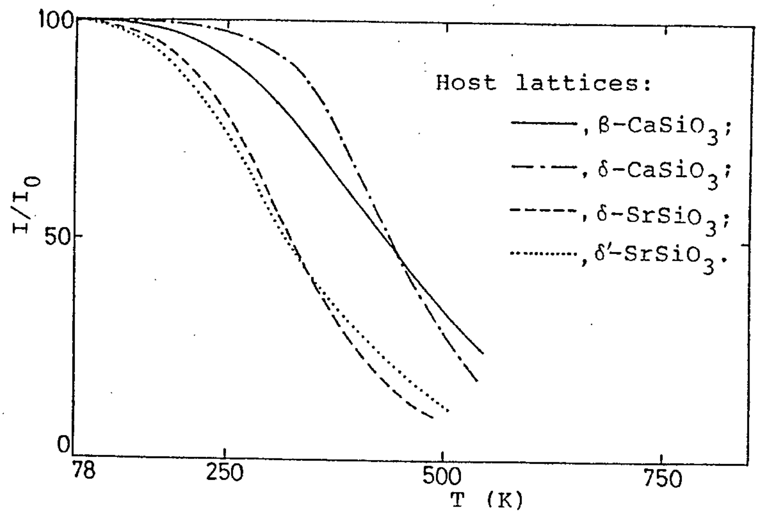

Figure 17. Temperature dependences for the light outputs of $CaSiO_3:Pb^{2+}$(5 at%) and $SrSiO_3:Pb^{2+}$(5 at%) polymorphs.

T_{50} value as δ-$SrSiO_3:Pb^{2+}$, gives the relatively strong emission as well as that of the δ form although the dispersion effect of the δ′ form cannot be expected as described previously.

4-5. Summary

The high-pressure synthesis up to 150 kbar was carried out on europium(II) metasilicate, $EuSiO_3$, and Eu^{2+}-activated calcium and strontium metasilicates, $MSiO_3:Eu^{2+}$ (M=Ca and Sr), and the luminescent properties of the resulting materials were studied. The crystal structures for the host lattices, α-, δ-, and δ′-$SrSiO_3$, were determined from three-dimensional X-ray diffraction data. New high-pressure phases, δ- and δ′-$EuSiO_3$, were obtained under pressures of about 60 and 70 kbar at 1000-1400°C, and the atmospheric phases, α-$CaSiO_3:Eu^{2+}$ and α-$SrSiO_3:Eu^{2+}$, transformed into δ-$CaSiO_3:Eu^{2+}$, δ-$SrSiO_3:Eu^{2+}$, and δ′-$SrSiO_3:Eu^{2+}$ at 35-100 kbar and 800-1400°C. The peak positions for the emission bands of $MSiO_3:Eu^{2+}$ shifted to short wavelength with the phase transformations: green (ca. 510 nm), α-$CaSiO_3:Eu^{2+}$; blue (ca. 470 nm), δ-$CaSiO_3:Eu^{2+}$; green (ca. 500 nm), α- and δ-$SrSiO_3:Eu^{2+}$; blue (ca. 465 nm), δ′-$SrSiO_3:Eu^{2+}$. In addition, their emission intensities were appreciably increased when the samples transformed into high-pressure phases. The phosphors, δ-$CaSiO_3:Eu^{2+}$ and δ'-$SrSiO_3:Eu^{2+}$, gave quantum efficiency values of about 20 and 40 %, whereas those of the atmospheric pressure phases were around 1 %. The crystals of α-, δ-, and δ'-$SrSiO_3$ belong to the monoclinic system (space group: C2), the triclinic system (space group: $P\bar{1}$), and the monoclinic system (space group: $P2_1/c$), respectively. Thses structures were solved by the direct method and refined by the block-diagonal least-squares. Final R values were 0.053 for 730 observed reflections of α-$SrSiO_3$, 0.043 for 1458 observed reflections of δ-$SrSiO_3$, and 0.046 for 914 observed reflections of δ'-$SrSiO_3$. The crystal lattices of α- and δ-$SrSiO_3$ consist of $(Si_3O_9)^{6-}$ rings while that of δ'-$SrSiO_3$ is constructed of four-membered rings of $(Si_4O_{12})^{8-}$. The Sr atoms in δ-$SrSiO_3$ are surrounded by six or eight oxygens whereas those in α- and δ'-$SrSiO_3$ occupy only the sites coordinated by eight oxygens. The above-mentioned luminescent properties are discussed on the basis of X-ray structural and IR structural analyses of the host lattices and temperature dependences of the emission spectra. For $CaSiO_3:Pb^{2+}$ and $SrSiO_3:Pb^{2+}$, the high-pressure phases, viz., the δ and δ' forms, also were found to give strong violet emissions sensitive to the 253.7 nm excitation.

GENERAL CONCLUSION

The purpose of the present studies is to synthesize new Eu^{2+}-containing compounds and to appreciate the possibilities for magnetic materials and phosphors. The structural analyses of the resulting materials are a significant approach towards the purpose since the magnetic and luminescent properties closely relate to crystal structures. In this work, these physical properties, especially luminescences, have been discussed with regard to the interactions between neighboring Eu^{2+} ions or the lattice vibrations of matrixes based on the X-ray and IR spectral analyses of the europium(II) compounds prepared or host lattices. New materials, findings, or informations obtained in the present studies are summarized in the following.

In the first chapter, new europium(II) borates, EuB_4O_7, EuB_2O_4, and $Eu_2B_2O_5$, have been prepared in the binary system $EuO-B_2O_3$. These borates and $Eu_3B_2O_6$ as obtained previously crystallize in the following symmetries: the orthorhombic system of $Pnm2_1$, EuB_4O_7; the orthorhombic system of Pnca, EuB_2O_4; the monoclinic system of $P2_1/a$, $Eu_2B_2O_5$; the trigonal system of $R\bar{3}c$, $Eu_3B_2O_6$. From the three-dimensional X-ray and IR spectral analyses, their crystal lattices have been found to be constructed of a three-dimensional $(B_4O_7)_\infty$ network, $(BO_2)_\infty$ chains, $B_2O_5{}^{4-}$, and $BO_3{}^{3-}$ ions for EuB_4O_7, EuB_2O_4, $Eu_2B_2O_5$, and $Eu_3B_2O_6$, respectively. The structures of these borate units reflect the habits of single crystals: $(B_4O_7)_\infty$ network, prism; $(BO_2)_\infty$ chain, needle; $B_2O_5{}^{4-}$ ion, plate; $BO_3{}^{3-}$ ion, hexagonal prism.

The borate, EuB_2O_4, is an antiferromagnet with $T_N \simeq 3$ K while EuB_4O_7 and $Eu_2B_2O_5$ are paramagnetic over the measured temperature. The magnetic properties have been understood by considering the relationship between their structures and the magnetic interactions. The magnetism of EuB_2O_4 is attributable to the antiferromagnetic interaction resulted from indirect 99.0 or 100.4° $Eu^{2+}-O^{2-}-Eu^{2+}$ superexchange pairs between nearest neighboring Eu^{2+} ions with $Eu^{2+}-Eu^{2+}$ distance of 3.896 Å. On the other hand, the magnetism of $Eu_3B_2O_6$ (T_C=7.5 K) are responsible for the following ferromagnetic exchange and superexchange pairs between nearest and second-nearest neighboring Eu^{2+} ions: direct Eu^{2+}-Eu^{2+} exchange pairs with interatomic distances of 3.509-3.778 Å and indirect 166.0°Eu^{2+}-O^{2-}-Eu^{2+} superexchange pairs with Eu^{2+}-Eu^{2+} distance of 5.450 Å.

A few of the europium(II) borates, e.g., EuB_4O_7 and EuB_2O_4, give the band emissions assigned to $4f^7$-$4f^6 5d$ transitios of Eu^{2+} ions, which are colored with violet-blue. No luminescence is observed on $Eu_2B_2O_5$ and $Eu_3B_2O_6$. It has been found that EuB_4O_7 and $SrB_4O_7{:}Eu^{2+}$ consisting of the $(B_4O_7)_\infty$ network give remarkably stronger emssion intensities than the other borates consisting of $(BO_2)_\infty$ chains, $B_2O_5{}^{4-}$, and $BO_3{}^{3-}$ ions. These experimental results are interpreted from their crystallographic properties with the help of the Dexter theory. For EuB_4O_7 and $SrB_4O_7{:}Eu^{2+}$ in which the Eu^{2+} ions are completely surrounded by BO_4 tetrahedra of $(B_4O_7)_\infty$ network, the quenching effect via the Coulomb or exchange interactions between neighboring Eu^{2+} ions can be expected to be smaller than that of the other borates. Therefore, EuB_4O_7 and SrB_4O_7 give the relatively strong emissions.

The borate, EuB_4O_7, has excellent thermal stability at high temperatures in air. This is attributable to the fact that the Eu^{2+} ions in EuB_4O_7 are completely surrounded by BO_4 units and are hardly attacked by oxygen.

In the second chapter, two europium(II) haloborates, Eu_2BO_3X and $Eu_2B_5O_9X$, have been obtained in the ternary system EuO-EuX_2(X=Cl and Br)-B_2O_3, and their single crystals with the shapes of hexagonal prism and needle or prism have been grown using the flux method. The crystals of Eu_2BO_3X belong to the hexagonal symmetry of $P6_3mc$ while $Eu_2B_5O_9X$ crystallizes in the orthorhombic system of Pnn2. The crystal structure of $Eu_2B_5O_9X$ has been found to consist of a three-dimensional $(B_5O_9)_\infty$ network from the X-ray analyses. The Eu^{2+} and X^- ions are alternately located in tunnels of the $(B_5O_9)_\infty$ network, and each Eu^{2+} ion is almost entirely isolated from neighboring Eu^{2+} ions because of the $(B_5O_9)_\infty$ network for the a- and b-axis directions and X^- ions for the c-axis direction.

The haloborate, Eu_2BO_3X, is a ferromagnet with $T_C \simeq 5$ K while

$Eu_2B_5O_9X$ is paramagnetic over the measured temperature. This result indicates that the magnetic interactions are strong for Eu_2BO_3X but weak for $Eu_2B_5O_9X$.

The haloborate, $Eu_2B_5O_9X$, is a blue-emitting phosphor and the compounds obtained by the dilution of the Eu^{2+} ions in the matrix, e.g., $Sr_2B_5O_9X:Eu^{2+}$, have been found to be efficient photoluminescent materials. However, no luminescence has been observed on Eu_2BO_3X. This finding can be accounted for by estimating the magnitudes of the Coulomb and exchange interactions between neighboring Eu^{2+} ions in $Eu_2B_5O_9X$, which are expected to be weak from the magnetism and the arrangement of anions around Eu^{2+} ions.

In the third chapter, the high-pressure phases of EuB_2O_4 and $MB_2O_4:Eu^{2+}$ (M=Ca and Sr) have been synthesized, viz., phases γ and δ. The pressure-temperature phase diagram of EuB_2O_4 consists of the following four regions: the high-pressure phases of α, γ, and δ forms and the decomposed phase of EuB_4O_7 and $Eu_2B_2O_5$. The phases γ- and δ-EuB_2O_4 are isostructural with the corresponding high-pressure phases of CaB_2O_4 and SrB_2O_4, respectively. Under the conditions above 40 kbar and 900°C, EuB_2O_4 decomposes as follows:

$$3\ EuB_2O_4 \longrightarrow EuB_4O_7 + Eu_2B_2O_5.$$

According to this scheme, the overall mole number is reduced from 3 to 2 and the volume of the sample also is reduced to 87.5 % compared with that of α-EuB_2O_4. The γ or decomposed phase of EuB_2O_4 are antiferromagnetic at low temperatures while δ-EuB_2O_4 has the tendency to be paramagnetic.

The high-pressure phases of EuB_2O_4 and $SrB_2O_4:Eu^{2+}$ give the band emissions assigned to $4f^7$-$4f^65d$ transitions of Eu^{2+} ions. The emission peak posision shifts to long wavelength with transformation into the δ phase because of the differences in the coördination of oxygen around Eu^{2+} ions. The emission intensity also increase with transformation into the δ phase. Particularly, the relative emission intensity of δ-$SrB_2O_4:Eu^{2+}$ is about 100 times higher than that of

α-SrB_2O_4:Eu^{2+} under 313 nm excitation, and hence the δ phase is one of excellent phosphors. This is due to the fact that the Eu^{2+} ions in the δ phase are effectively surrounded by the BO_4 tetrahedra of three-dimensional $(B_3O_6)_\infty$ network and hardly interact with neighboring Eu^{2+} ions in a similar manner to those in SrB_4O_7:Eu^{2+} and $Sr_2B_5O_9X$:Eu^{2+}. The luminescent properties of the high-pressure phases of CaB_2O_4:Eu^{2+} correspond to those of EuB_2O_4 pressed out into the grain boundaries of the matrix because of the crystallographic mismatch of Eu^{2+} and Ca^{2+} ions.

A high-pressure phase, β-$SrAl_4O_7$, has been obtained by the hydrothermal preparation method under high pressures. The crystal lattice consists of a three-dimensional $(Al_4O_7)_\infty$ network of AlO_6 octahedra and AlO_4 tetrahedra.

In the fourth chapter, the high-pressure phases of $EuSiO_3$ and $MSiO_3$:Eu^{2+} (M=Ca and Sr) have been prepared at 30-150 kbar. Both of $SrSiO_3$ and $EuSiO_3$ show similar high-pressure polymorphisms to that of $CaSiO_3$, and transform into phases δ and δ' at pressures of 35-70 kbar. The δ form is isostructural with δ-$CaSiO_3$, but the δ' phase is not formed for $CaSiO_3$, and hence it is a characteristic phase of $SrSiO_3$ or $EuSiO_3$. The ε (perovskite) form of $SrSiO_3$ or $EuSiO_3$ is not obtained because of the large ionic radius of Sr^{2+} or Eu^{2+}. The structures of δ-$SrSiO_3$ and δ-$EuSiO_3$ consist of $(Si_3O_9)^{6-}$ rings in a manner similar to δ-$CaSiO_3$ while the δ' forms of $SrSiO_3$ and $EuSiO_3$ contain $(Si_4O_{12})^{8-}$ rings. The Sr or Eu atoms in these phases are surrounded by six or eight oxygens for the δ form and eight oxygens for the δ' form.

The luminescent properties of $CaSiO_3$:Eu^{2+} and $SrSiO_3$:Eu^{2+} phosphors considerably change following the phase transformations. The excitation and emission spectra of δ-$CaSiO_3$:Eu^{2+} and δ'-$SrSiO_3$:Eu^{2+} are responsible for the Eu^{2+} ions which occupy the eightfold sites in the matrixes while the Eu^{2+} ions on the eightfold sites in δ-$SrSiO_3$:Eu^{2+} contribute to its luminescent spectra. For the α phases of $CaSiO_3$:Eu^{2+} and $SrSiO_3$:Eu^{2+}, the reflection spectra disagree with their excitation spectral patterns. This means that there are two kinds of Eu^{2+} ions in the matrixes: one functions as the luminescent center whereas the other does not. Most of the Eu^{2+} ions belong to the latter type, and hence the emission intensity of this phase is weak. The experimental observation that the quantum efficiency of the sample appreciably increases with transformation into the δ-$CaSiO_3$ or δ'-$SrSiO_3$ phase is qualitatively interpreted by considering the crystal structure of host lattice and the dispersion of Eu^{2+} ions in the matrix.

It has been pointed out throughout this work that the efficient phosphors obtained consist of three-dimensional network or rings as highly condensed with borate or silicate units, which relieve the quenching effects on Eu^{2+} ions caused by the Coulomb and exchange interactions between neighboring Eu^{2+} ions or the lattice vibrations of matrixes. These informations must give a guide to research efficient Eu^{2+}-activated phosphors. For Eu^{2+}-activated phosphors, whose crystal lattices can be expected to transform into high-pressure phases with highly condensed frameworks, the high-pressure treatments are very effective means of increasing the brightness of phosphors.

Acknowledgement

The author is greatly indebted to Professor Dr. Jiro Shiokawa for his kind encouragement and valuable suggestions throughout this work.

The author also is indebted to Professor Dr. Hideo Tamura and Professor Dr. Toshio Tanaka for their valuable suggestions in the course of this thesis.

The author would like to express his sincere thanks to Associate Professor Dr. Gin-ya Adachi for his direction during the course of the study and for his stimulating discussion and reading the manuscript.

Grateful acknowledgement is made to Professor Dr. Mitsue Koizumi and Drs. Masahiko Shimada, Kaichi Suito, and Akifumi Onodera for their supports of sample preparations under high-pressure conditions and helpful discussions.

The author also wishes to thank to Professor Dr. Nobutami Kasai and Dr. Noritake Yasuoka, Kunio Miki, Nobuo Tanaka, Yasushi Kai, and Yasuo Hata for their kind suggestions on X-ray measurements and computations

The author is very grateful to Dr. Masanori Nakane, Dr. Nagao Kamijo, Mr. Masahiro Setoguchi, and Mr. Ken-ichi Sakaguchi for the measurements on four-circle X-ray diffractometers and Mr. Noriyuki Ogawa for his assistances of sample preparations at high pressures.

The author also wishes to extend acknowledgement to Mr. Yoshiyuki Hirashima, Dr. Tsuyoshi Arakawa, and Dr. Tsutomu Shin-ike for their encouragement and helpful advices.

Thanks are given to Mr. Hajime Hata, Mr. Yoshikazu Moriwaki, and Mr. Naofumi Ito for their assistances and Mr. Tetsuo Sakai and all the members of Shiokawa laboratory for their friendships.

References

1) B. T. Matthias, R. M. Bozorth, and J. H. Van Vleck, Phys. Rev. Lett., 7, 1960 (1961).

2) a) T. R. McGuire, B. E. Argyle, M. W. Shafer, and J. S. Smart, J. Appl. Phys., 34, 1345 (1963); b) T. R. McGuire and M. W. Shafer, J. Appl. Phys., 35, 984 (1964); c) B. E. Argyle, J. C. Suits, and M. J. Freiser, Phys. Rev. Lett., 15, 822 (1965); d) R. F. Brown, A. W. Lawson, and G. E. Everett, Phys. Rev., 172, 559 (1968); e) V. E. Wood, Phys. Lett., 30A, 25 (1969).

3) M. W. Shafer, J. Appl. Phys., 36, 1145 (1965).

4) a) T. R. McGuire, M. W. Shafer, and R. J. Joenk, J. Appl. Phys., 37, 981 (1966); b) J. E. Greedan and G. J. McCarthy, Mater. Res. Bull., 7, 531 (1972); c) C. Chien, S. DeBenedetti, F. D. Borros, Phys. Rev. Sect. B, 10, 3913 (1974).

5) a) K. Y. Ahn and J. C. Suits, IEEE Trans. on Magnetics, 3, 453 (1967); b) G. Fan and J. H. Greiner, J. Appl. Phys., 41, 1401 (1970); c) G. Fan and R. A. Burn, J. Appl. Phys., 42, 3458 (1971).

6) J. C. Suits and K. Lee, J. Appl. Phys., 42, 3258 (1971).

7) J. C. Suits, B. E. Argyle, and M. J. Freiser, J. Appl. Phys., 37, 1391 (1966).

8) a) J. B. Goodenough, " Magnetism and the Chemical Bond," Interscience, New York (1963) p. 146; b) T. Kasuya, IBM J. Res. Develop., 14, 214 (1970).

9) a) G. Blasse and A. Bril, Philips Tech. Rev., 31, 304 (1970); b) G. Blasse, " Struct. Bonding," Berlin (1976), Vol. 26, pp. 43-79.

10) G. Blasse, Phys. Status Solidi B, 55, K131 (1973).

11) a) R. A. Hewes and M. V. Hoffman, 3, 261 (1971); b) J. P. Meehan and E. J. Wilson, J. Cryst. Growth, 15, 141 (1972); c) M. V. Hoffman, J. Electrochem. Soc., 119, 905 (1972); d) N. S. Altshuler, L. D. Livanova, and A. L. Stolov, Opt. Spectroc. (Engl. Transl.), 36, 72 (1974); e) J. L. Sommerdijk, J. M. P. J. Verstegen, and A. Bril, J. Lumin., 8, 502 (1974); f) L. H. Brixner and J. D. Bierlein, Mater. Res. Bull., 9, 99 (1974); g) B. Tanguy, P. Merle,

M. Pezat, and C. Fouassier, Mater. Res. Bull., 9, 831 (1974); h) L. H. Brixner and A. Ferretti, J. Solid State Chem., 18, 111 (1976); i) P. Valon, J. C. Cousseins, A. Vedrine, J. C. Gacon, G. Boulon, and F. K. Fong, Mater. Res. Bull., 11, 43 (1976); j) B. Latourrette, J. Grannec, C. Fouassier, and P. Hagenmuller, Mater. Res. Bull., 11, 135 (1976); k) L. H. Brixner, 11, 269 (1976).

12) G. Blasse, A. Bril, J. de Vries, J. Electrochem. Soc., 115, 977 (1968)

13) a) A. L. N. Stevels and A. D. M. Schrama-de Pauw, J. Lumin., 14, 147 (1976); b) A. L. N. Stevels and J. M. P. J. Verstegen, J. Lumin., 14, 207 (1976); c) J. M. P. J. Verstegen and A. L. N. Stevels, J. Lumin., 9, 406 (1974); d) A. L. N. Stevels and A. D. M. Schrama-de Pauw, J. Electrochem. Soc., 123, 691 (1976); e) A. L. N. Stevels, 17, 121 (1978).

14) a) H. G. Jenkins and A. H. McKeag, J. Electrochem. Soc., 97, 415 (1950); b) G. Blasse, W. L. Wanmaker, J. W. ter Vrugt, and A. Bril Bril, Philips Res. Rept., 23, 189 (1968); c) E. Kaldis, P. Streit, and P. Wachter, J. Phys. Chem. Solids, 32, 159 (1971); d) J. M. P. J. Verstegen and J. L. Sommerdijk, J. Lumin., 9, 297 (1974).

15) C. C. Lagos, J. Electrochem. Soc., 117, 1189 (1970).

16) A. L. N. Stevels and F. Pingault, Philips Res. Rept., 30, 277 (1975).

17) a) G. J. McCarthy and J. E. Greedan, Inorg. Chem., 14, 772 (1975); b) J. E. Greedan, G. J. McCarthy, and C. Sipe, Inorg. Chem., 14, 775 (1975).

18) G. J. McCarthy and W. B. White, J. Less-Common Met., 22, 409 (1970).

19) C. E. Weir and R. A. Schroeder, J. Res. NBS, 68A, 465 (1964).

20) H. Hata, G. Adachi, and J. Shiokawa, Mater. Res. Bull., 12, 811 (1977).

21) C. F. Chenot, J. Am. Ceram. Soc., 50, 117 (1967).

22) T. Ashida, " The Universal Crystallographic Computing System-Osaka," The Computing Center, Osaka University (1979), pp. 53-59.

23) T. Ashida, " The Universal Crystallographic Computing System-

Osaka, " The Computing Center, Osaka University (1979), p. 60.

24) " International Tables for X-ray Crystallography," Kynoch Press, Birmingham (1974), Vol. IV, pp. 72-102.

25) T. Kurita, H. Yamamoto, M. Takada, and Y. Komurasaki, Shimadzu Hyoron, 32, 225 (1975).

26) M. Marezio, H. A. Plettinger, and W. H. Zachariasen, Acta Crystallogr., 16, 390 (1963).

27) Y. Takeuchi, Acta Crystallogr., 5, 574 (1952).

28) a) S. Garcia-Blanco and J. Fayos, Z. Kristallogr., 127, 145 (1968); b) J. Pardo, M. Martinez-Ripoll, and S. Garcia-Blanco, Acta Crystallogr., Sect. B, 30, 37 (1974).

29) H. Bartl and W. Schuckmann, Neues Jahrb. Mineral. Monatsh., 1966, 253.

30) A. Perloff and S. Block, Acta Crystallogr., 20, 274 (1966).

31) D. L. Dexter, J. Chem. Phys., 21, 836 (1953).

32) G. Blasse, Philips Res. Rept., 24, 131 (1969).

33) a) T. E. Peters and J. Baglio, J. Inorg. Nucl. Chem., 32, 1089 (1970); b) C. Fouassier, A. Levasseur, and P. Hagenmuller, J. Solid State Chem., 3, 206 (1971); c) M. D. J. Lloyd, A. Levasseur, and C. Fouassier, J. Solid State Chem., 6, 179 (1973).

34) a) J. Majling, V. Figusch, J. Corba, and F. Hanic, J. Appl. Crystallogr., 7, 402 (1974); b) Z. Zak and F. Hanic, Acta Crystallogr., Sect. B, 32, 1784 (1976).

35) J. G. Smeggil and H. A. Eick, Inorg. Chem., 10, 1458 (1971)

36) O. Muller and R. Roy, " The Major Ternary Structural Families," Springer-Verlag, New York (1974), pp. 62-63, 71, 78.

37) W. H. Zachariasen, Acta Crystallogr., 17, 749 (1964).

38) a) M. Marezio, H. A. Plettinger, and W. H. Zachariasen, Acta Crystallogr., 16, 594 (1963); b) A. D. Mighell, A. Perloff, and S. Block, Acta Crystallogr., 20, 819 (1966).

39) a) C. H. Chang and J. L. Margrave, Mater. Res. Bull., 2, 929 (1967); b) M. Marezio and J. P. Remeika, J. Chem. Phys., 44, 3348 (1966).

40) a) M. Marezio, J. P. Remeika, and P. D. Dernier, Acta Crystallogr.,

Sect. B, 25, 955 (1969); b) M. Marezio, J. P. Remeika, and P. D. Dernier, Acta Crystallogr., Sect. B, 25, 965 (1969).

41) P. D. Dernier, Acta Crystallogr., Sect. B, 25, 1001 (1969).

42) M. Shimada, N. Ogawa, M. Koizumi, F. Dachille, and R. Roy, Am. Ceram. Soc. Bull., 58, 519 (1979).

43) J. Krogh-Moe, Acta Chem. Scand., 18, 2055 (1964).

44) D. J. Craik, " Magnetic Oxides Part I," Wiley, New York (1975), p. 12.

45) D. S. McClure and Z. J. Kiss, J. Chem. Phys., 39, 3251 (1963).

46) A. J. Lindop and D. W. Goodwin, Acta Crystallogr., Sect. B, 28, 2625 (1972).

47) W. Hörkner and HK. Müller-Buschbaum, J. Inorg. Nucl. Chem., 38, 983 (1976).

48) N. A. Toropov, V. P. Barzakovskii, V. V. Lapin, and N. N. Kurtseva, " Handbook of Phase Diagrams of Silicate Systems, — Binary Systems," Israel Program for Scientific Translations, Jerusalem (1972),Vol. I, pp. 20-44.

49) a) A. E. Ringwood and A. Major, Earth Planet. Sci. Lett., 2, 106 (1967); b) L. Liu and A. E. Ringwood, Earth Planet. Sci. Lett., 28, 209 (1975).

50) a) K. S. Mamedov and N. V. Belov, Doklady Akad. Nauk SSSR, 107, 463 (1956); b) F. J. Trojer, Z. Kristallogr., 127, 291 (1968).

51) J. W. Jeffery and L. Heller, Acta Crystallogr., 6, 807 (1953).

52) F. J. Trojer, Z. Kristallogr., 130, 185 (1969).

53) Y. Shimizu, Y. Syono, and S. Akimoto, High Temp.-High Pressures, 2, 113 (1970).

54) a) N. Kawai, M. Togaya, and A. Onodera, Proc. Jpn. Akad., 49, 623 (1973); b) K. Suito and N. Kawai, High-pressure Sci. Technol., 2, 53 (1979).

55) P. Main, S. E. Hull, L. Lessinger, G. Germain, J. P. Declercq, and and M. M. Woolfson, " A System of Computer Programs for the Automatic Solution of Crystal Structures from X-ray Diffraction Data, MULTAN 78 "; University of York: USA (1978).

56) A. F. Wells, " Structural Inorganic Chemistry," 4th ed., Oxford

(1975), p. 815.

57) R. D. Shannon, Acta Crystallogr., Sect. A, 32, 225 (1975).

58) A. E. Ringwood and A. Major, Earth Planet. Sci. Lett., 12, 411 (1971).

59) K. Nakamoto, " Infrared Spectra of Inorganic and Coordination Compounds," John Willey and Sons, Inc., New York (1963), Part II, pp. 103-110.

60) a) A. N. Lazarev, Opt. Spektrosk., 9, 195 (1960); b) A. N. Lazarev and T. F. Tenisheva, Opt. Spektrosk., 11, 584 (1961); c) A. N. Lazarev, Opt. Spektrosk., 12, 60 (1962); d) A. N. Lazarev and T. F. Tenisheva, Zh. Strukt. Khim., 4, 703 (1963); e) A. N. Lazarev and V. A. Kolesova, Izv. Akad. Nauk SSSR, Neorg. Mater., 6, 1445 (1970); f) A. N. Lazarev and I. S. Ignatyev, Opt. Spektrosk., 28, 971 (1970).

61) F. Matossi and H. Kruger, Z. Phys., 99, 1 (1936).

62) a) H. C. Froelich, J. Electrochem. Soc., 93, 101 (1948); b) G. R. Fonda and H. C. Froelich, J. Electrochem. Soc., 93, 114 (1948); c) G. R. Fonda and F. J. Studer, J. Opt. Soc. Am., 42, 360 (1952).